

AD-A199 292

REMOTE MEASUREMENT OF UPPER ATMOSPHERIC DENSITY &  
FEASIBILITY STUDY(U) MICHIGAN UNIV ANN ARBOR SPACE  
PHYSICS RESEARCH LAB P B HAYES ET AL. 10 JUN 88

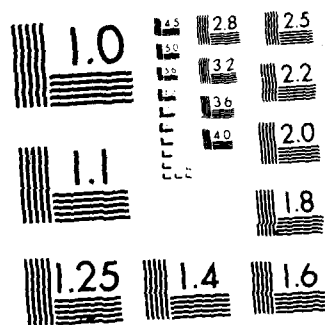
1/2

UNCLASSIFIED

AFGL-TR-88-0139 F19628-87-K-0039

F/G 16/2

NL



MICROCOPY RESOLUTION TEST CHART  
NATIONAL BUREAU OF STANDARDS-1963-A

**DTIC FILE COPY**  
AFGL-TR-88-0139

(4)

**Remote Measurement of Upper Atmospheric  
Density: A Feasibility Study**

P. B. Hayes  
V. J. Abreu  
C. R. Cornish  
J. J. Horvath

M. Luo  
W. R. Skinner  
J. H. Yee

AD-A199 292

University of Michigan  
Space Physics Research Laboratory  
Ann Arbor, Michigan 48109-2143

10 June 1988

Final Report  
23 March 1987-22 March 1988

APPROVED FOR PUBLIC RELEASE; DISTRIBUTION UNLIMITED

AIR FORCE GEOPHYSICS LABORATORY  
AIR FORCE SYSTEMS COMMAND  
UNITED STATES AIR FORCE  
HANSCOM AIR FORCE BASE, MASSACHUSETTS 01731-5000

**DTIC**  
**ELECTE**  
**S** **D**  
SEP 12 1988  
H

88 9 12 08 1

"This technical report has been reviewed and is approved for publication"

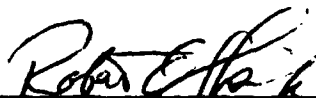


FRANK A. MARCOS  
Contract Manager



WILLIAM K. VICKERY  
Acting Branch Chief

FOR THE COMMANDER



ROBERT A. SKRIVANEK  
Division Director

This report has been reviewed by the ESD Public Affairs Office (PA) and is releasable to the National Technical Information Service (NTIS).

Qualified requestors may obtain additional copies from Defense Technical Information Center.

If your address has changed, or if you wish to be removed from the mailing list, or if the addressee is no longer employed by your organization, please notify APGL/DAA, Hanscom AFB, MA 01731. This will assist us in maintaining current mailing list.

Do not return copies of this report unless contractual obligations or notice on a specific document requires that it be returned.

Unclassified

SECURITY CLASSIFICATION OF THIS PAGE

# AD-A199221

## REPORT DOCUMENTATION PAGE

1a. REPORT SECURITY CLASSIFICATION Unclassified			1b. RESTRICTIVE MARKINGS		
2a. SECURITY CLASSIFICATION AUTHORITY			3. DISTRIBUTION/AVAILABILITY OF REPORT Approved for public release; Distribution unlimited		
2b. DECLASSIFICATION/DOWNGRADING SCHEDULE					
4. PERFORMING ORGANIZATION REPORT NUMBER(S)			5. MONITORING ORGANIZATION REPORT NUMBER(S) AFGL-TR-88-0139		
6a. NAME OF PERFORMING ORGANIZATION University of Michigan		6b. OFFICE SYMBOL (if applicable)	7a. NAME OF MONITORING ORGANIZATION Air Force Geophysics Laboratory		
6c. ADDRESS (City, State, and ZIP Code) Space Physics Research Laboratory Ann Arbor, Michigan 48109-2143			7b. ADDRESS (City, State, and ZIP Code) Hanscom AFB Massachusetts 01731-5000		
8a. NAME OF FUNDING/SPONSORING ORGANIZATION		8b. OFFICE SYMBOL (if applicable)	9. PROCUREMENT INSTRUMENT IDENTIFICATION NUMBER F19628-87-K-0039		
8c. ADDRESS (City, State, and ZIP Code)			10. SOURCE OF FUNDING NUMBERS		
			PROGRAM ELEMENT NO 61101F	PROJECT NO ILIR	TASK NO 7E
11. TITLE (Include Security Classification) Remote Measurement of Upper Atmospheric Density: A Feasibility Study					
12. PERSONAL AUTHOR(S) P. B. Hays, V. J. Abreu, C.R. Cornish, J.J. Horvath, M. Luo, W.R. Skinner, J. H. Yee					
13a. TYPE OF REPORT FINAL REPORT		13b. TIME COVERED FROM 3/23/87 TO 3/22/88		14. DATE OF REPORT (Year, Month, Day) 1988 June 10	
15. PAGE COUNT 120					
16. SUPPLEMENTARY NOTATION This research was supported by the AFGL In-house Laboratory Independent Research Fund.					
17. COSATI CODES			18. SUBJECT TERMS (Continue on reverse if necessary and identify by block number) Atmospheric density Rayleigh scattering Satellite remote sensing Stellar occultation Resonance fluorescence		
FIELD	GROUP	SUB-GROUP			
19. ABSTRACT (Continue on reverse if necessary and identify by block number)  → Orbital reentry of large maneuverable vehicles and the potential to modify orbital parameters using the aerobreaking technique have increased the need to understand in detail the variability of atmospheric density in the mesosphere and lower thermosphere. The variability of mass density in the mesosphere has been apparent for many years, being seen in sounding rocket data, backscatter radar profiles, and airglow optical emissions. The →					
20. DISTRIBUTION/AVAILABILITY OF ABSTRACT <input type="checkbox"/> UNCLASSIFIED/UNLIMITED <input type="checkbox"/> SAME AS RPT. <input type="checkbox"/> DTIC USERS			21. ABSTRACT SECURITY CLASSIFICATION Unclassified		
22a. NAME OF RESPONSIBLE INDIVIDUAL Frank Marcos			22b. TELEPHONE (Include Area Code)		22c. OFFICE SYMBOL AFGL/LIS

Cont of Block 19:

systematic variations that have been determined from these data sets are the obvious seasonal, latitudinal, and local time dependences that are prescribed in the major models in use today. These models, however, are based on liminated data and thus, are not useful in making predictions or forecasts of the effects of planetary waves or gravity wave breaking. The primary fact holding back the improvement of these models and the development of a forecasting technique is the lack of a sufficiently large and accurate morphological data base. This global data base must rely on a sampling technique that will provide a morphology of the atmospheric density in the critical 60 to 120 km region. The only practical method of providing global information is to use a remote sensing technique for earth orbit, given a technique that has the required accuracy and spatial sensitivity. The University of Michigan Space Physics Research Laboratory has evaluated several means of obtaining the density morphology in the Mesosphere and lower Thermosphere by remote sensing techniques.



Accession For	
NTIS GPA&I	<input checked="checked" type="checkbox"/>
DTIC T&F	<input type="checkbox"/>
Unannounced	<input type="checkbox"/>
Justification	
By	
Distribution/	
Availability Codes	
Dist	Avail and/or Special
A-1	

## Table of Contents

<b>1.</b>	<b>INTRODUCTION .....</b>	<b>1</b>
<b>2.</b>	<b>STELLAR OCCULTATION TECHNIQUE .....</b>	<b>3</b>
2.1	Principle of Stellar Occultation .....	4
2.1.1	O <sub>2</sub> Absorption Cross-sections .....	6
2.1.2	Stellar Occultation Spectra .....	11
2.2	Recovery of Density and Temperature Profiles .....	15
2.2.1	Data Analysis .....	15
2.2.2	Statistical Error Analysis .....	17
2.2.3	An Example: 39_Lambda_Orion .....	18
2.3	Summary and Discussion .....	21
<b>3.</b>	<b>RESONANCE FLUORESCENCE OF O<sub>2</sub> .....</b>	<b>25</b>
3.1	The O <sub>2</sub> Atmospheric Bands .....	26
3.1.1	Spectral Intensity of the Atmospheric Bands .....	26
3.1.2	Characteristics of the O <sub>2</sub> Atmospheric Band Emission .....	28
3.2	Recovery of Density and Temperature Profiles .....	36
3.2.1	Mathematical Formulation .....	36
3.2.2	Data Analysis .....	39
3.3	Statistical Accuracy Analysis .....	46
3.4	Summary and Discussion .....	51
<b>4.</b>	<b>RAYLEIGH SCATTERING TECHNIQUE .....</b>	<b>55</b>
4.1	Scattering Intensity Simulation .....	57
4.2	Summary and Discussion .....	60
<b>5.</b>	<b>MERIT EVALUATION .....</b>	<b>61</b>
5.1	Feasibility .....	61
5.2	Accuracy .....	61
5.2.1	Statistical Error .....	61
5.2.2	Systematic Error .....	62
5.2.3	Pointing and Satellite Position Error .....	63
5.3	Complexity .....	63
5.3.1	Operation .....	63
5.3.2	Data Analysis .....	64
5.4	Data Coverage .....	64

5.4.1	Spatial Coverage .....	64
5.4.2	Temporal Coverage .....	64
5.5	Scientific Merits .....	65
5.6	Summary .....	65
<b>6.</b>	<b>CONCEPTUAL INSTRUMENT DESIGN .....</b>	<b>67</b>
6.1	Image Plane Detector Spectrophotometer (IPDS) .....	67
6.2	Ebert-Fastie Grating Spectrometer (EFGS) .....	69
6.2.1	The O <sub>2</sub> Resonance Measurement .....	70
6.2.1.1	Field-of-View Determination .....	70
6.2.1.2	Telescope Selection and Input Slit Width Determination ...	70
6.2.1.3	Grating Selection .....	71
6.2.1.4	Detector Selection: A CCD Device .....	74
6.2.2	The Occultation Measurement .....	75
6.2.2.1	Telescope Selection .....	75
6.2.2.2	Grating Selection .....	75
6.2.2.3	Detector Selection: A CCD Device .....	77
6.3	Summary of Instrument Parameters for EFGS .....	78
<b>7.0</b>	<b>OPERATIONAL REQUIREMENTS.....</b>	<b>79</b>
7.1	O <sub>2</sub> Resonance .....	79
7.2	Stellar Occultation .....	81
	References .....	85
	Appendix .....	89



## ABSTRACT

There is a great need for a large and accurate global data base in the critical 60 to 120 km region of the atmosphere in order to understand in detail the spatial and temporal variabilities in its mass density. The only practical method of providing global information is to use a remote sensing technique from earth orbit. Several possible techniques had been proposed which have the potential to measure the density in this important atmospheric region. These include measuring the brightness of sunlight that is rayleigh scattered by the molecular nitrogen and oxygen, measuring the absorption of starlight during stellar occultation, and measuring the intensity of molecular oxygen resonance fluorescence. A feasibility study, funded by the Air Force Geophysics Laboratory, has been conducted here at the Space Physics Research Laboratory, University of Michigan, on the relative merits of these techniques. This report presents the results of the trade-off studies wherein various sources of error and complexity of the data analysis are evaluated. An instrumental conceptual design is also prepared identifying the major hardware elements required to implement the remote sensing technique.

## 1. INTRODUCTION

Orbital reentry of large maneuverable vehicles and the potential to modify orbital parameters using the aerobreaking technique have increased the need to understand in detail the variability of atmospheric density in the mesosphere and lower thermosphere. Acceleration data (Champion, 1986) obtained during shuttle reentry illustrates the fact that the atmosphere exhibits variation which often exceeds expectation and which raise questions regarding the safe return of heavy Shuttle payloads from polar orbit.

The variability of mass density in the mesosphere has been apparent for many years, being seen in sounding rocket data, backscatter radar profiles, and airglow optical emissions (Wasser and Donahue, 1979). The systematic variations that have been determined from these data sets are the obvious seasonal, latitudinal, and local time dependencies that are prescribed in the major models in use today. These models, however, are based on limited data and thus, are not useful in making predictions or forecasts of the effects of planetary waves or gravity wave breaking. The wave processes will never be accurately predicted, but like the weather in the troposphere we may ultimately be able to base a forecast on operational information. The primary factor holding back the improvement of these models and the development of a forecasting technique is the lack of a sufficiently large and accurate morphological data base.

This global data base must rely on a sampling technique that will provide a morphology of the atmospheric density in the critical 60 to 120 km region, with the consistency required to quantify the higher frequency variability. The only practical method of providing global information is to use a remote sensing technique from earth orbit, given a technique that has the required accuracy and spacial sensitivity. Such a technique could be tested using first sub-orbital evaluation, followed by shuttle validation, and finally deployed on a satellite in earth orbit to provide the required global information.

Several possible remote sensing techniques have been proposed which have the potential to measure the atmospheric density in this important atmospheric region. These include measuring the brightness of sunlight that is rayleigh scattered by the molecular nitrogen and oxygen (Rusch et al., 1983), measuring the absorption of starlight during stellar occultation (Hays and Roble, 1968), and a new technique where the fluorescence of molecular oxygen is measured photometrically. Each of these methods of sensing the density has inherent advantages as well as weaknesses. In this report, we will examine these techniques in details by simulating the measurements.

developing the density recovering algorithms, designing conceptually the best suitable instrument, and analyzing the errors in the recovered density. The three proposed approaches will be evaluated, focusing primarily on the accuracy of the measurements, the complexity of the data processing and analysis.

## 2. STELLAR OCCULTATION TECHNIQUE

Stellar occultation has been used for many years to determine the composition and number density profiles in the Earth and planetary atmospheres. During the early years, most of the occultation measurements have been made from rockets by examining the absorption of solar ultraviolet radiation in certain atmospheric bands. For example, vertical ozone density profiles were obtained by Johnson et al. (1951) from series of rockets using this technique. Later, artificial satellites were used (Venkateswaran et al. 1961; Hinteregger and Hall, 1969; Hays and Roble, 1973).

Basically, the occultation technique is similar to the classical technique of absorption spectroscopy, and has been investigated in detail, with the early theoretical studies of Hays and Roble (1968a), examination of errors by Roble and Hays (1972), and recent reviews by Atreya (1981). As shown in Fig. 2.1, the Sun, Moon, or a star is used as a source of light and the satellite photometer as a detector, with the atmosphere between acting as the extinction cell. At long wavelengths (such as visible and radio wave) the extinction results primarily from differential refraction of the light by atmospheric particles. At shorter wavelengths (e.g. ultraviolet), however, absorption by the various atmospheric species is mainly responsible for the extinction of light. As the satellite moves in its orbit, the intervening atmosphere extinguishes progressively more of the light as it traverses deeper layers of the atmosphere. The occultation intensity data can be related to the tangential column number density of the atmospheric species provided that the extinction cross-sections are known. The equation for the tangential column number density can then be easily inverted to give the number density profile at the occultation tangent point. It is worthwhile to note that the atmospheric densities obtained from this technique are independent of the knowledge of absolute flux of the light source, as the technique depends only on the relative attenuation of the light. However, the nature of the light source does affect the design of the instrument in terms of the accuracy required for the recovered density profile.

In this chapter we describe a technique for retrieving the temperature and the molecular oxygen number density profiles in the critical 60 to 120 km altitude region from occultation intensity data. A data-reduction technique similar to the one described by Hays and Roble (1968a) is developed, and a theoretical error analysis is used to determine the accuracy of the retrieved temperature and density profiles in the presence of random statistical error in the measured intensities. This allows us to examine the retrieval accuracy as a function of the star brightness and its color type.

## 2.1 Principle of Stellar Occultation

A detector on board a spacecraft, as shown in Fig. 2.1, measures the unattenuated intensity,  $I_\infty$ , of the source when the absorption path, the line connecting the source and the detector, is above the atmosphere. As the spacecraft moves in its orbit, the absorption path descends deeper into the atmosphere, resulting in progressively greater absorption of light. The attenuation of monochromatic light of wavenumber  $\nu$  due to absorption by the  $i^{\text{th}}$  atmospheric species is given by Beer's Law, which states

$$I(\nu, r_0) = I_\infty(\nu) \exp \left[ - \sum_i \tau_i(\nu) \right], \quad (2.1)$$

where  $I(\nu, r_0)$  is the attenuated intensity at tangent point of radius  $r_0$ , and  $\tau_i(\nu)$  is the line of sight optical depth of species,  $i$ . If we assume that the absorption cross-section of the  $i^{\text{th}}$  atmospheric species at wavenumber  $\nu$ ,  $\sigma_i(\nu)$ , is independent of altitude,  $\tau_i(\nu)$  can be written as

$$\tau_i(\nu) = \sigma_i(\nu) N_i(r_0), \quad (2.2)$$

where  $N_i(r_0)$  is its line of sight column density of the absorber  $N_i$  at radius  $r_0$ . In the case of a spherically stratified atmosphere, the tangential column density  $N_i(r_0)$  is

$$N_i(r_0) = 2 \int_{r_0}^{\infty} \frac{n_i(r) r dr}{\sqrt{r^2 - r_0^2}} \quad (2.3)$$

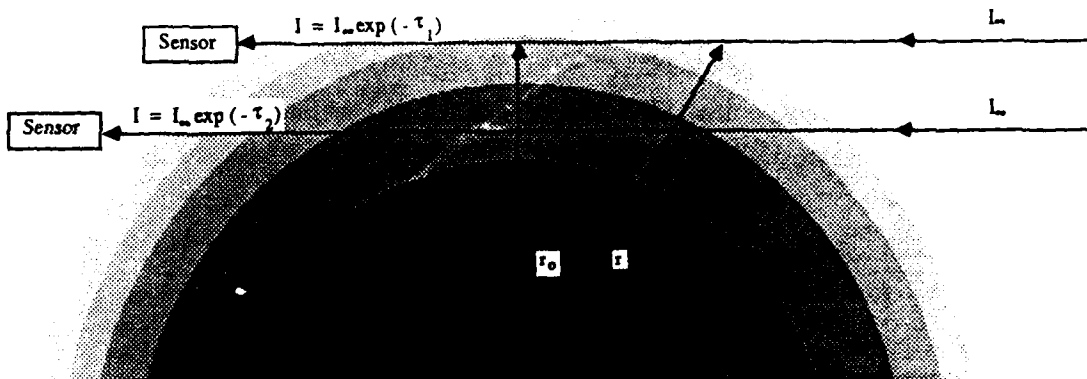


Figure 2.1

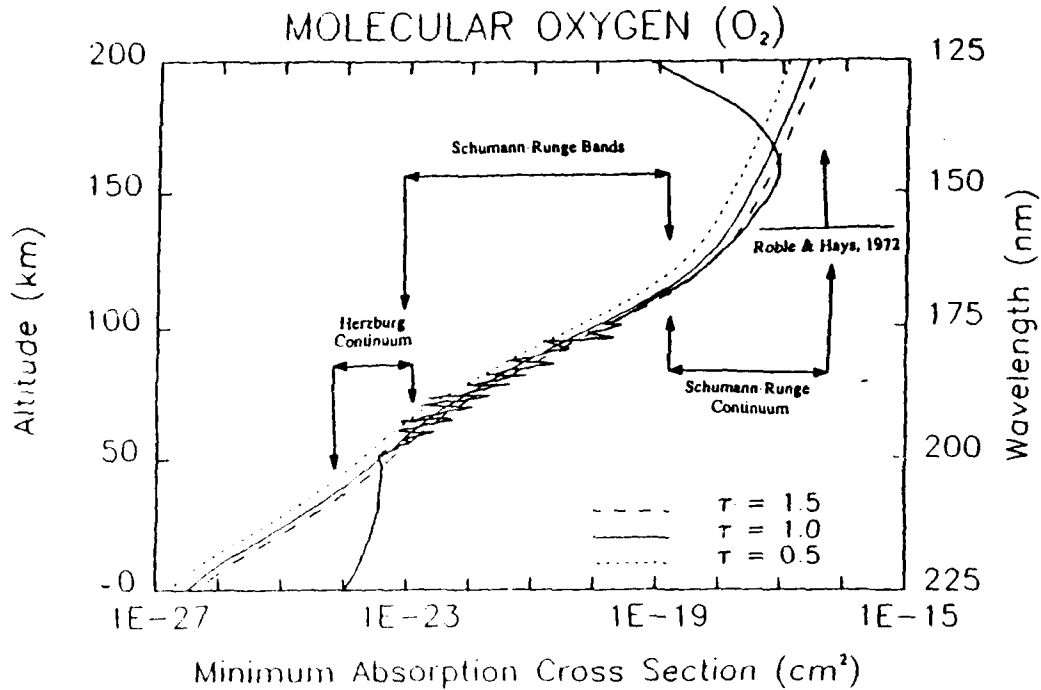


Figure 2.2

where  $n_i(r)$  is the number density of the  $i^{\text{th}}$  absorbing species at a distance  $r$  from the center of the Earth. This equation is the Abel integral equation (c.f. Hays and Roble, 1968 a, b) which can then be directly inverted to give the number density of the absorbing species at radius  $r$

$$n_i(r) = -\frac{1}{\pi} \int_r^\infty \frac{[dN(r_0)/dr_0] dr_0}{\sqrt{r^2 - r_0^2}} \quad (2.4)$$

Hays and Roble (1968b) calculated the tangential ultraviolet transmission for the mesosphere and the lower thermosphere. They showed that in certain specific wavelength and altitude intervals the ultraviolet starlight is absorbed by a single species and attenuations due to refraction and Rayleigh scattering are negligible. These include a region near 1500Å (66000 cm<sup>-1</sup>) where molecular oxygen acts as a single absorber in the lower thermosphere and also a region near 2500Å (40000 cm<sup>-1</sup>) where ozone is a single absorber in the mesosphere.

Among various photoabsorption processes by the molecular oxygen, photodissociations through the Herzberg continuum, Schumann-Runge bands and Schumann-Runge continuum make the most contributions to the extinction of solar ultraviolet light. Fig. 2.2 shows the required magnitudes of absorption cross-section as a function of tangent height which would give optical depths of 0.5, 1.0 and 1.5 for an O<sub>2</sub> atmosphere during an occultation sequence. The absorption

cross-sections of molecular oxygen due to the three processes are also shown. The observations near the Schumann-Runge continuum allow measurement of density down to about 120 km. This has been successfully demonstrated in the observations of the OAO-A2 satellite reported by Hays and Roble (1973). As the altitude decreases and the tangential O<sub>2</sub> column density increases, the spectral regions with smaller absorption cross-sections are required, and the various Schumann-Runge bands between 1750Å and 2000Å (50000-57000 cm<sup>-1</sup>) and the Herzberg continuum beyond 2000Å (< 57000 cm<sup>-1</sup>) become applicable. Although these regions were also observed by the OAO-A2 satellite, the occultation data were not analyzed due to the complexity of the band system and the uncertainty of knowledge of its relatively small cross-sections. Recently cross-sections of the Herzberg continuum (Cheung et al., 1986a) and the Schumann-Runge bands as well as the positions of each of the individual rotational lines have been obtained at very high resolution (~0.04 cm<sup>-1</sup>) from photoabsorption measurements using a photoelectric scanning spectrometer (Yoshino et al., 1983, 1984; Cheung et al., 1984; Yoshino et al., 1987). This allows us to understand the band systems better theoretically, and enables us to examine the feasibility of using the stellar occultation technique to extract O<sub>2</sub> number density in the critical 60 to 120 km region.

### 2.1.1 O<sub>2</sub> Absorption Cross-sections

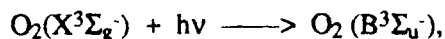
#### *Herzberg Continuum*

The Herzberg continuum is one of the two important dissociation continua in O<sub>2</sub> photoabsorption processes. It occurs near the O<sub>2</sub> dissociation limit where  $\lambda < 2420\text{\AA}$  and involves a forbidden transition between O<sub>2</sub>(X<sup>3</sup>Σ<sub>g</sub><sup>-</sup>, ground state and O<sub>2</sub>(A<sup>3</sup>Σ<sub>u</sub><sup>+</sup>) excited state, leading to photo-dissociation products of two O(<sup>3</sup>P) atoms.

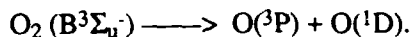
The absorption at this transition is rather weak, thus measurements of the cross-sections are very difficult (Buisson et al., 1933; Gotz and Maier-Leibnitz, 1933). Ditchburn and Young (1962) used long absorption paths to increase the optical depth and obtained cross-sections in this spectral region varying from 1.4x10<sup>-24</sup> cm<sup>2</sup> at 2500Å to 2.64x10<sup>-23</sup> cm<sup>2</sup> at 2000Å. Recently, using a 6.65m photoelectric scanning spectrometer, Cheung et al., (1986a) were able to measure the Herzberg continuum cross-sections more accurately in the wavelength region between 1950Å and 2400Å. They obtained a peak cross-section of 6.62x10<sup>-24</sup> cm<sup>2</sup> at 2010Å, which is smaller than the ones that Ditchburn and Young (1962) had derived and Banks and Kockart (1973) had adopted. In this study, we use the laboratory measurement of Cheung et al. (1986a).

### *Schumann-Runge Continuum*

The stronger Schumann-Runge Continuum arises because the permitted electric-dipole transition



for wavelengths shorter than 1750Å down to 1250Å, and leads to a final molecular state lying above the threshold for the dissociation



It has an absorption cross-section that peaks with a value of  $1.1 \times 10^{-17} \text{ cm}^2$  near 1400Å and decreases toward the longer wavelengths. Early measurements by Ladenburg and Van Voorhis (1933) and by Watanabe et al. (1953) differ by about 25 percent at some wavelengths. Later measurements by Metzger and Cook (1964) and Huffman et al. (1964) also differ by approximately 10 percent. Hall et al. (1965) then indicated the need for more accurate measurements, given the differences in the published values of the absorption cross-sections, and the necessity to accurately know this cross-section for stellar occultation measurements of atmospheric density. In an attempt to investigate the effect of temperature on the  $\text{O}_2$  absorption coefficients, Hudson et al. (1966) measured the absorption cross-sections of the Schumann-Runge Continuum between 1580Å and 1950Å at three different temperatures. They concluded that the maximum change in the absorption cross-section is about 10% when the temperature of the oxygen is increased from 300 K to 1000K. In our study, we adopt the cross-sections of Metzger and Cook (1964) for  $1325\text{Å} < \lambda < 1650\text{Å}$ , and the results of Hudson et al. (1966) at 300K for  $1650\text{Å} < \lambda < 1800\text{Å}$ .

### *Schumann-Runge Bands*

The Schumann-Runge band system, originating from the same electronic transition as the Schumann-Runge Continuum, begins with the (0-0) band at 2026Å and converges to the second dissociation limit at about 1750Å. Kreusler (1901) first attempted to measure the absorption coefficient in this spectral region and obtained a cross-section on the order of  $10^{-21} \text{ cm}^2$ . Since then these bands have been studied extensively by several investigators, for example, by Watanabe et al. (1953) and by Wilkinson and Mulliden (1957). Recently, using a high resolution photoelectric scanning spectrometer, Yoshino et al. (1983), Cheung et al. (1984) and Yoshino et al. (1987) were able to measure the absorption cross-sections of each of the individual rotational line throughout the wavelength region containing the ( $\nu'$ ,0) bands with  $\nu' = 0,12$ . Errors in the their cross-



section measurements were estimated to be 4 percent and somewhat greater for cross-sections less than  $5.0 \times 10^{-22} \text{ cm}^2$ . The band oscillator strengths were obtained at two temperatures, 300 K and 79K, and differences between them were observed although they lie within the measurement errors.

Because of the existence of a repulsive  $^3\Pi_u$  state, whose potential curve crosses that of the  $B^3\Sigma_u^-$  in the vicinity of  $v = 4$ , the lines in the Schumann-Runge bands are predissociative lines, i.e. they are unstable against molecular dissociation. As a result, these lines are broadened, and extensive overlaps exist between rotational lines in the same band or different bands. Determining  $O_2$  density using the stellar occultation technique from the photoabsorption of light in the Schumann-Runge bands thus requires line by line calculations based on a band model that will take into account the effect of temperature on both the band oscillator strength and the absorption coefficient of each rotational line. Next we will describe how we have calculated the absorption cross-section of each line.

If we designate a line within a Schumann-Runge band by its upper and lower states of the vibrational, rotational, and total angular momentum quantum numbers,  $v', N', J'$  and  $v'', N'', J''$ , respectively, the absorption cross-section  $\sigma(v'u'', N''N'', J'J'')$  can be written as

$$\sigma(v'u'', N''N'', J'J'') = \frac{8\pi^3\nu}{3hc} R_{v'u''}^2 S(v'u'', N''N'', J'J''), \quad (2.5)$$

where  $\nu$  is the transition frequency,  $c$  is the speed of the light,  $R_{v'u''}$  is the transition moment which is the product of the electronic dipole moment and the vibrational overlap integral, and  $S(v'u'', N''N'', J'J'')$  is the line strength, or Hönl-London factor.

The oscillator strengths are calculated for the lines in the Schumann-Runge bands arising from the  $F_2$  fine-structure component of the ground  $X^3\Sigma_g^-$  state, since the dependence of the oscillator strength on the fine-structure component is expected to be weak (Lewis et al., 1987). The Hönl-London factors are taken from Tatum and Watson (1971) for a coupling case intermediate between Hund's cases (a) and (b). They are calculated using the accurate  $O_2$  molecular parameters of the  $X^3\Sigma_g^-$  state (Steinbach and Gordy, 1975) and the  $B^3\Sigma_u^-$  state (Cheung et al., 1986b). All of the twelve allowed lines in the P and R branches, including the weak satellite lines, and the two forbidden lines corresponding to  $\Delta N = \pm 3$  are included. The vibrational wave functions and the overlap integral are computed based on the  $X^3\Sigma_g^-$  potential of Allison et al. (1971) and the  $B^3\Sigma_u^-$  potential of Allison et al. (1986). The electronic dipole moment of Allison et al. (1986) was also adopted.

The shape of each rotational line in the Schumann-Runge bands is broadened due to predissociation and has been approximated by a Lorentzian profile by Hudson and Mahle (1971) and Omidvar and Frederick (1987) in their calculations of photodissociation rate. The absorption cross-section of a line  $i$  at wavenumber  $\nu$ ,  $\sigma_i(\nu)$ , using the Lorentz distribution function is given by

$$\sigma_i(\nu) = \sigma(\nu_i) \frac{(\Delta L_i/2)^2}{(\nu - \nu_i)^2 + (\Delta L_i/2)^2}, \quad (2.6)$$

where  $\nu_i$  and  $\sigma(\nu_i)$  are the wavenumber and the cross-section at the line center, and  $\Delta L_i$  is the FWHM (Full Width at Half Maximum) line width. The validity of this assumption was discussed in detail by Omidvar and Frederick (1987), except that we used measured Lorentz widths of Yoshino (1988, private communication), which give the variation of  $\Delta L_i$  with respect to the total angular momentum quantum number  $J$ .

The temperature effect on the absorption coefficients is introduced when the rotational population of  $O_2(X^3\Sigma_g^-, v'')$ ,  $f_N(T)$ , is considered,

$$f_N(T) = (2N + 1) \exp \{ - E''/kT \} / Q_r(T), \quad (2.7)$$

where  $Q_r$  is the rotational partition function given by

$$Q_r(T) = \sum_{N=1,3,5}^{\infty} (2N + 1) \exp \{ - E''/kT \}, \quad (2.8)$$

$T$  is the rotational temperature,  $E''$  is the energy level for the rotational level  $N$ , and  $N$  takes only odd integer numbers, in accordance with the exclusion principle for an ordinary  $O_2$  molecule (Herzberg, 1950). For temperatures below 300K (the case in the lower thermosphere and mesosphere), all  $O_2$  molecules are populated in their lowest vibrational level,  $v'' = 0$ . We can then define an effective absorption cross-section  $\sigma_{ei}(\nu, T)$  as

$$\sigma_{ei}(\nu, T) = f_N(T) \sigma_i(\nu) \quad (2.9)$$

and calculate the optical depth  $\tau(\nu)$  by

$$\tau(\nu) = \int_{-\infty}^{\infty} \sum_i n(s) f_N(T) \sigma_i(\nu) ds = \sum_i \int_{-\infty}^{\infty} n(s) \sigma_{ei}(\nu, T) ds \quad (2.10)$$

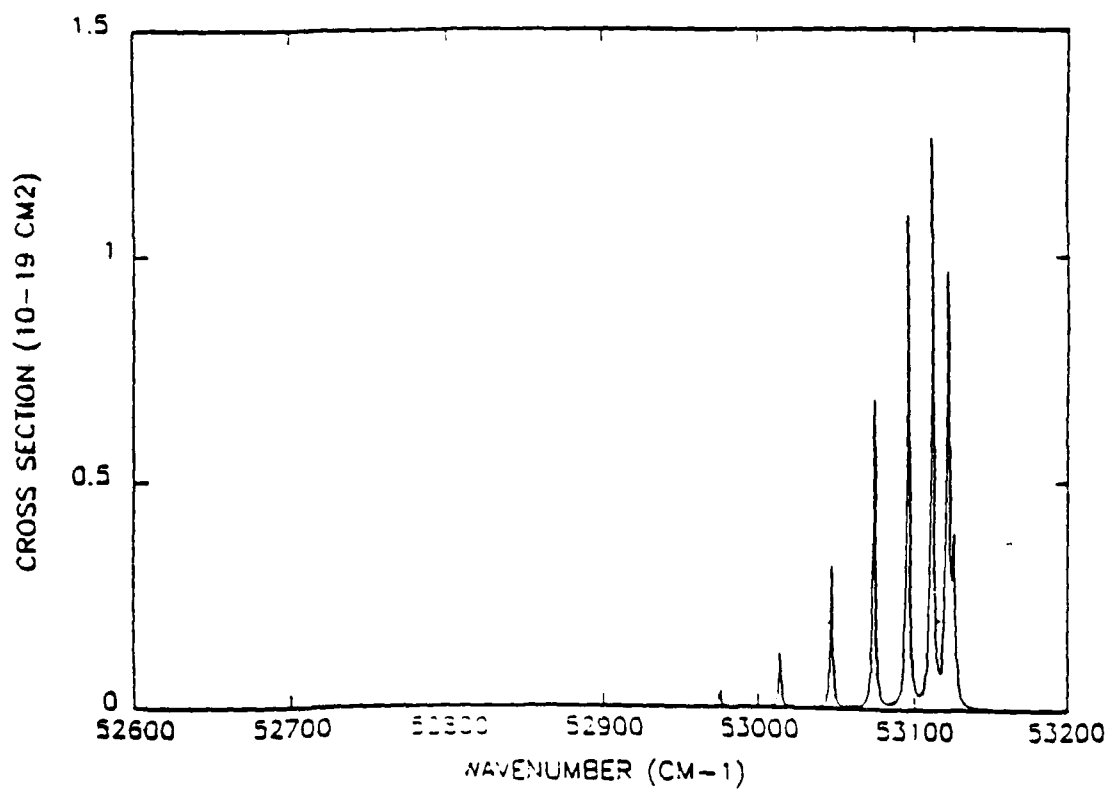
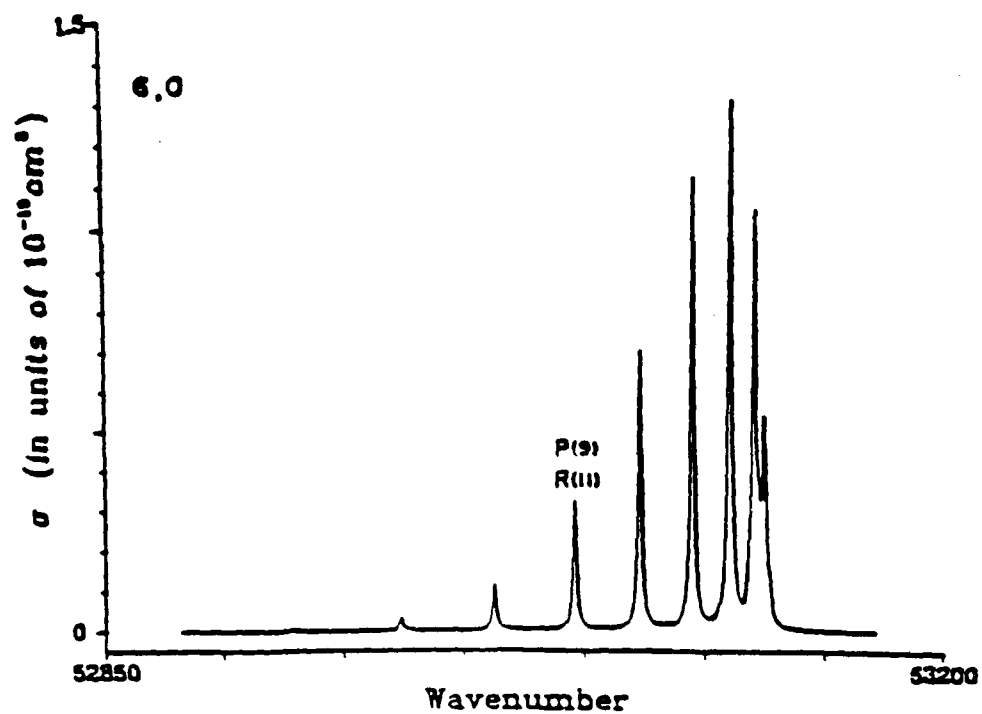


Figure 2.3

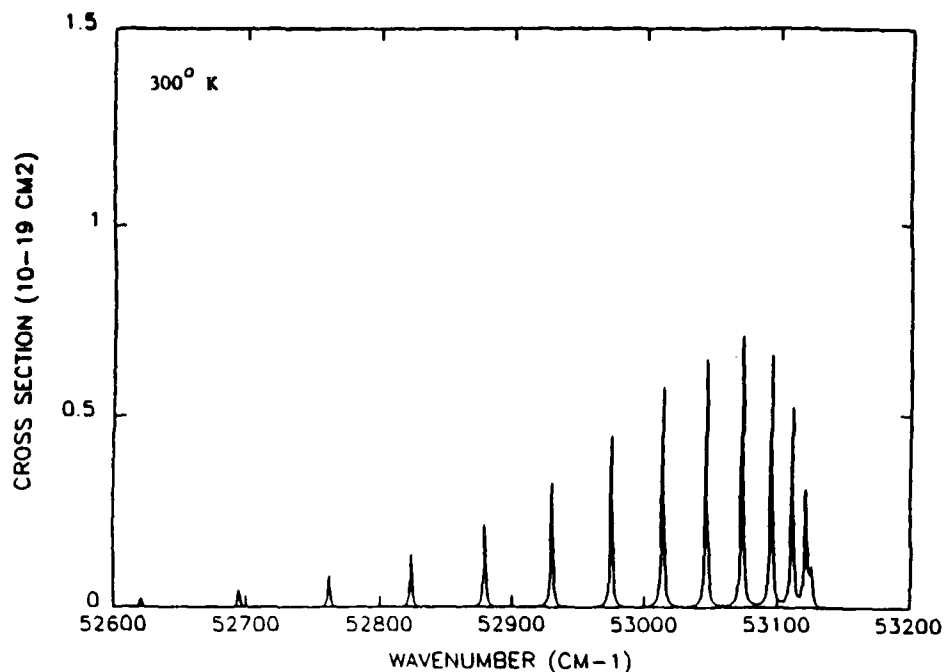


Figure 2.4

to consider the overlap of adjacent lines. All of the cross-sections appearing hereafter will be referred to as the effective cross-sections, so that the rotational and vibrational populations of the  $O_2$  molecules do not have to be considered.

Fig. 2.3 shows our calculated absorption cross-sections of Schumann-Runge (6,0) band in comparison with the measurements of Yoshino et al. (1987) at 79K. The two are in excellent agreement. Fig. 2.4 presents the calculated absorption cross-sections at 300K for the same (6,0) band. As the temperature increases, the lines in the shorter wavenumber region, representing the transitions from higher rotational levels of the ground state of  $O_2$ , become more pronounced. This apparent change in band structure, which appears more clearly in a high resolution  $O_2$  absorption spectrum, thus can provide rotational temperature information of the ground state  $O_2(X^3\Sigma_g^-)$  molecules, and will be illustrated further in detail in the next section.

### 2.1.2 Stellar Occultation Spectra

Fig. 2.5 presents the calculated occultation spectra in the spectral region between 50000 and 56000  $cm^{-1}$  for tangent heights at 60, 80 and 100 km. Since the column density of the absorber,  $O_2$ , is

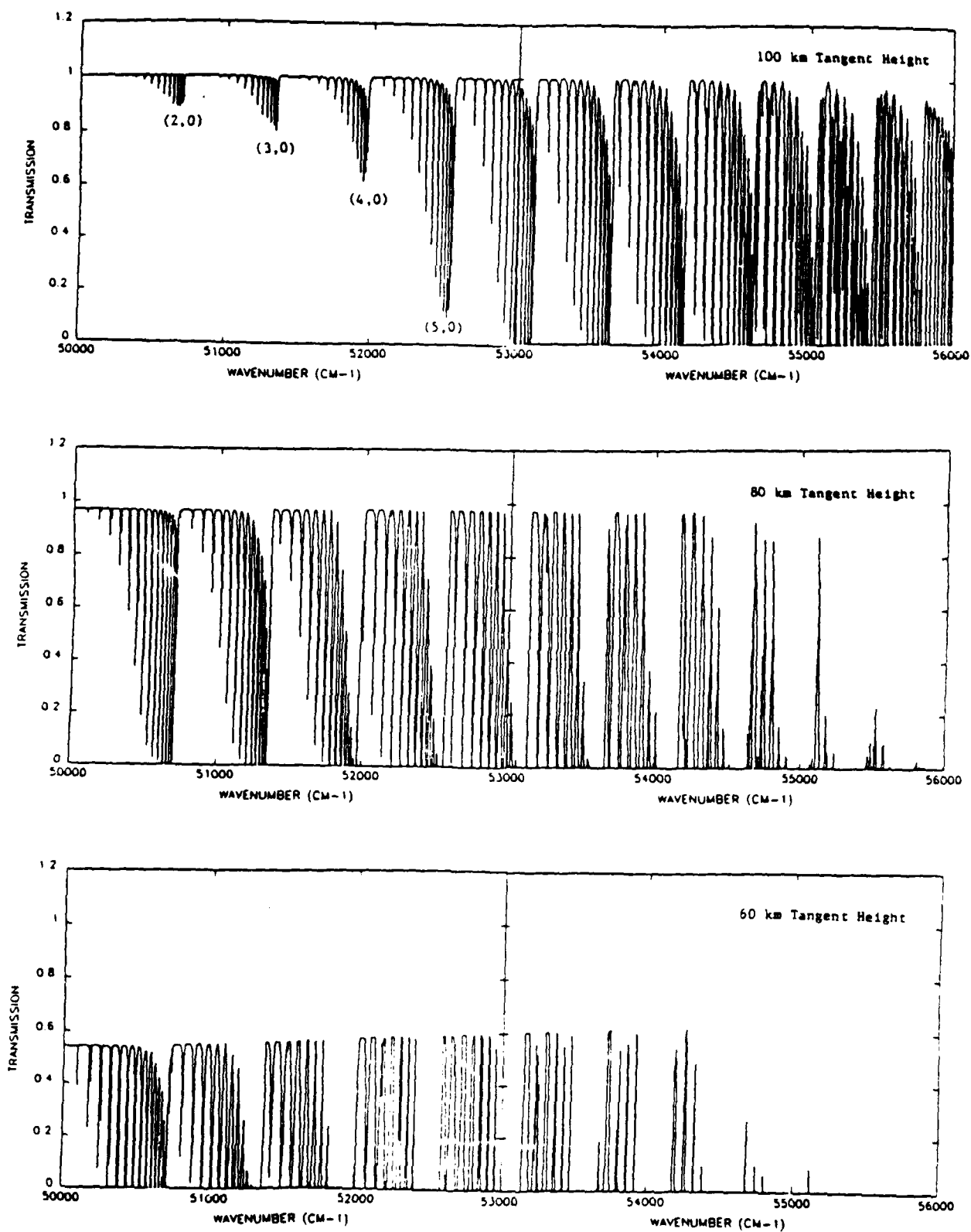


Figure 2.5

small for measurements at high tangent heights, the overall absorption is weaker in comparison to measurements at lower tangent heights. The structure of the Schumann-Runge bands can clearly be seen, from the weaker (2,0) band near 50000 cm<sup>-1</sup> to the stronger (13,0) band near 56000 cm<sup>-1</sup>. Complete absorption is observed near 56000 cm<sup>-1</sup> for the measurement at 60 km tangent height. The envelope, showing a transmission of ~0.5 in the shorter wavenumber region, results from the Herzberg continuum lying underneath the Schumann-Runge bands.

Single wavelength (photometric) occultation measurements carried out in the past have assumed the knowledge of the cross-section. Because the absorption cross-sections of the Schumann-Runge bands are temperature dependent, the accuracy with which we can retrieve the O<sub>2</sub> number density profile depends upon how accurately we know the temperature profile. Consequently, it is best to carry out temperature measurements simultaneously with the density measurements. This can be accomplished by carrying out spectrometric occultation measurements in order to provide simultaneous spectral information, which can be used to retrieve the temperature profile.

Here we demonstrate the recovery of the number density and temperature profiles by simulating occultation measurements using a simple Ebert-Fastie Spectrometer with a CCD (Charged-Coupled Device) detector. The intensity signal of a star,  $C(z_t, \nu)$ , measured in counts/sec at a tangent altitude  $z_t$  and wavenumber  $\nu$ , can be expressed by

$$C(z_t, \nu) = S \int_0^{\infty} I(\nu') T(\nu' - \nu) d\nu', \quad (2.11)$$

where  $S = A Q_e T_o$ ,  $A$  is the aperture area of the telescope,  $Q_e$  is the quantum efficiency of the detector,  $T_o$  is the optical transmission of the system, and  $T(\nu' - \nu)$  is the broadening function or transmission function of the dispersive element at wavenumber  $\nu$ . Since a star is a point source, the instrument transmission function is a rectangular function with its spectral width determined by how the dispersed light is imaged onto the detector and by the number of CCD pixels combined. The spectral resolution is thus variable since the number of pixels that can be combined is easily controlled.

Fig. 2.6 illustrates how the occultation transmission spectrum varies with the rotational temperature of the absorber, O<sub>2</sub>. A column density of O<sub>2</sub> equal to 10<sup>22</sup> cm<sup>-2</sup> (~80 km tangent height) is used in this illustration. Five rotational temperatures, varying from 200K to 300K with an increment of 25K, are simulated for two spectrometer instrument widths, 50 cm<sup>-1</sup> (Fig. 2.6a) and 1000 cm<sup>-1</sup> (Fig. 2.6b) respectively. The various Schumann-Runge ( $\nu', 0$ ) bands are better resolved by the

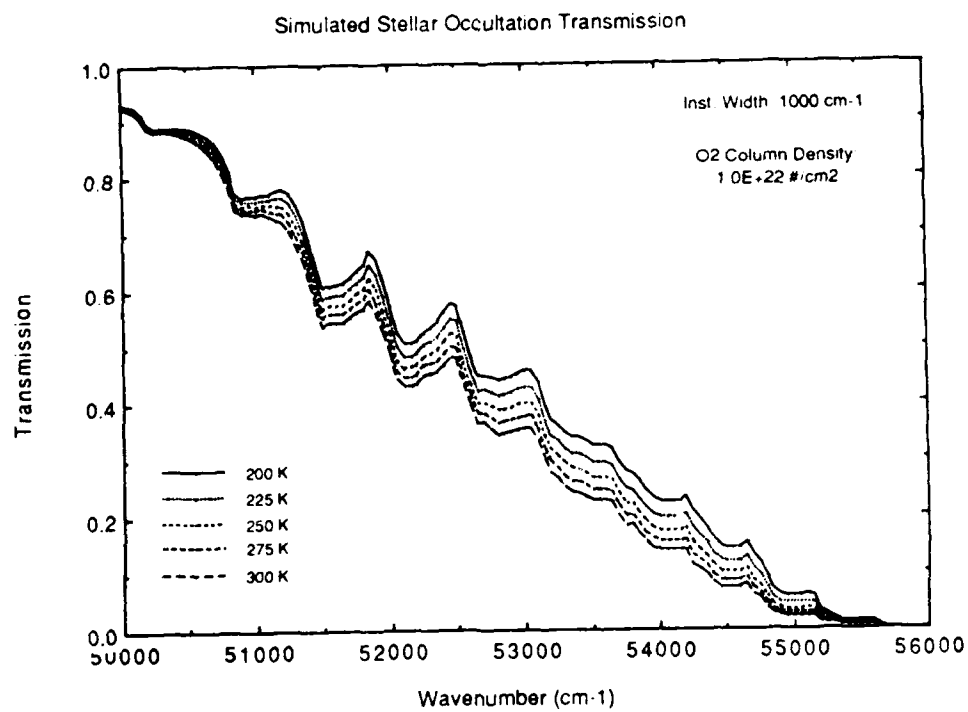
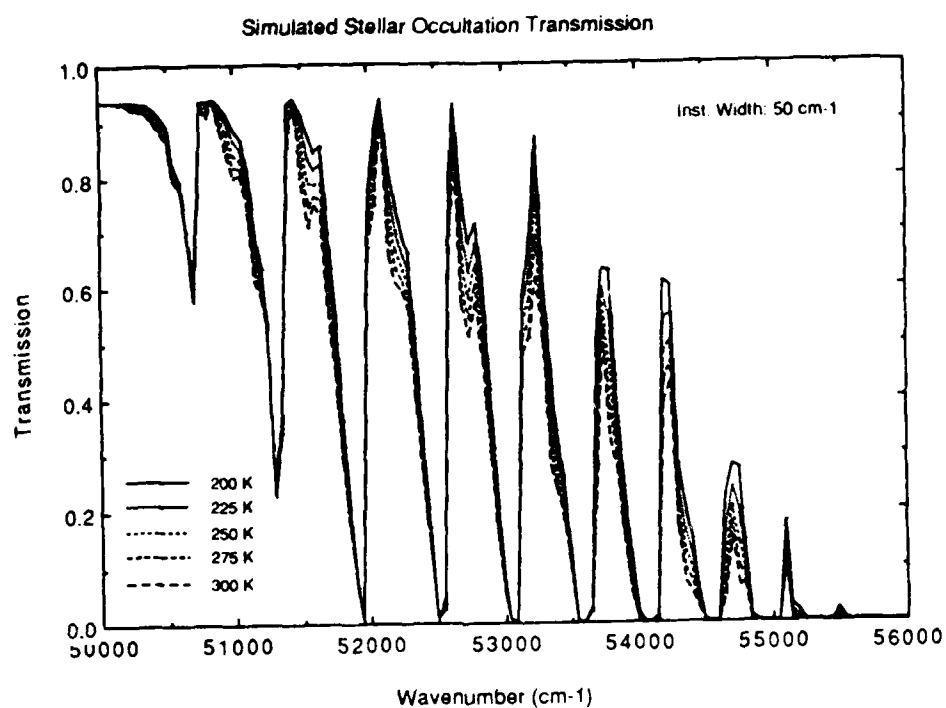


Figure 2.6

higher resolution instrument. The rotational band structure of each vibrational band is also better revealed, indicating that the rotational temperature may be determined more accurately if enough signal were observed. It is worth to note here that a 25K change in temperature gives rise to approximately 5 to 10 percent change in the transmission in certain temperature sensitive spectral regions. In other words, an uncertainty of 25K in temperature may translate into an error of ~5 to 10 percent in the deduced column density, and this error varies with the spectral resolution of the measured spectra. In fact, if we include regions of the spectra where the cross-sections are temperature insensitive and fit the spectra with a temperature, the actual error will be much smaller. This concept is the basis of our data analysis technique used to retrieve the O<sub>2</sub> number density profile.

## 2.2 Recovery of Density and Temperature Profiles

### 2.2.1. Data Analysis

There are many techniques that can be used to recover the number density and the temperature profiles of the absorber from the measured stellar occultation spectra. Here we use a simple technique which filters out the temperature dependence of the absorption cross-sections first. Rewriting Eq. (2.1) in terms of  $\tau(\nu)$  defined in Eq. (2.10) and a weighted cross-section,  $\bar{\sigma}(\nu)$ , one obtains

$$I(\nu) = I_{\infty}(\nu) \exp \left\{ - \sum_i \int_{-\infty}^{\infty} n(s) \sigma_{ei}(\nu, T) ds \right\} = I_{\infty}(\nu) \exp \left\{ - N(O_2) \bar{\sigma}(\nu) \right\}, \quad (2.12)$$

where  $\bar{\sigma}(\nu)$  is

$$\bar{\sigma}(\nu) = \frac{\sum_i \int_{-\infty}^{\infty} n(s) \sigma_{ei}(\nu, T) ds}{\int_{-\infty}^{\infty} n(s) ds}. \quad (2.13)$$

The temperature filtering process can be accomplished by defining an effective temperature,  $\bar{T}$ , at which the absorption cross-sections best represent the weighted cross-sections. We can then



perform a non-linear least-square fit to the spectra to obtain  $\bar{T}$  and the column density at each tangent ray height. This is a good approximation since the departure of the actual  $\sigma(\nu)$  from the one given by  $\bar{T}$  is very small and represents only a second-order effect to the total extinction of the light. The error in the deduced column density therefore is negligible. Also if the atmospheric temperature does not vary rapidly with altitude, since most of the absorption takes place near the tangent point, the deduced effective temperature becomes very close to the one at the tangent altitude.

Let  $C_{ij}$  denote the occultation signal at wavenumber  $i$  and tangent height  $j$ , which is a function of the effective temperature  $\bar{T}_j$  and  $O_2$  column density  $N_j$ . The unknowns,  $\bar{T}_j$  and  $N_j$ , may be calculated from the measured spectra using a non-linear least-squares fitting technique. We first linearize the problem by expanding Eq. (2.11) about empirically determined approximations ( $\bar{T}_{oj}$ ,  $N_{oj}$ ) for the temperature and the  $O_2$  column density using only the first-order terms in the expansion:

$$C_{ij}(\bar{T}_j, N_j) \cong C_{ij}(\bar{T}_{oj}, N_{oj}) + \frac{\partial C_{ij}}{\partial T} (\bar{T}_j - \bar{T}_{oj}) + \frac{\partial C_{ij}}{\partial N} (N_j - N_{oj}). \quad (2.14)$$

The sum of the squares of the residuals between the theoretically computed signal and the measured signal is calculated by

$$\langle \delta^2 \rangle = \sum_i (M_{ij} - C_{ij})^2, \quad (2.15)$$

where  $M_{ij}$  is the measured signal at wavenumber  $i$  and tangent height  $j$ . By minimizing  $\langle \delta^2 \rangle$ , one can obtain a better set of estimates for  $T_j$  and  $N_j$ , or  $X_l^j$  ( $l=1,2$ ), a general representation of  $T_j$  ( $l=1$ ) and  $N_j$  ( $l=2$ ), from a single matrix multiplication operation:

$$X_l = \sum_{m=1}^2 \alpha_{lm} B_m, \quad (2.16)$$

where  $\alpha$  is the inverse matrix of  $A_{lm}$

$$A_{lm} = \sum_i \frac{\partial C_{ij}}{\partial X_l} \frac{\partial C_{ij}}{\partial X_m}, \quad (2.17)$$

and

$$B_m = \sum_i \left\{ C_{ij} - M_{ij} - \sum_{l=1}^2 \frac{\partial C_{ij}}{\partial X_l} X_{ol} \right\} \frac{\partial C_{ij}}{\partial X_m} . \quad (2.18)$$

The procedure is reiterated until the estimated values converge. The speed of convergence depends on the proximity of the initial values for  $(X_{01}^j, X_{02}^j)$  or  $(\bar{T}_j, N_j)$  to the actual values. The expression (Eq. 2.3) for the column density  $N_j$  at tangent height  $j$  is a simple Abel integral equation which can be inverted to give the number density profile of  $O_2$  (Hays and Roble, 1968a,b and Roble and Hays, 1972).

### 2.2.2 Statistical Error Analysis

The accuracy in retrieving the number density profile from the occultation intensity data depends upon (a) the number of data points per scan, (b) the number of spectral measurements per point, (c) the statistical noise inherent in the signal, (d) knowledge of the absorption cross-sections, (e) knowledge of the satellite position during occultation, and (f) departures from spherical symmetry. The first three items are examined in this chapter. Item (d) has been discussed in the previous section and is not included in the statistical error analysis performed here. Item (e) depends on the satellite tracking and the degree of accuracy in telescope pointing. Its errors will appear in the tangent ray height determination and will not be discussed in this work. The last item may be important for species which change rapidly with time. In this analysis, however, a spherical symmetry is assumed.

Considering that the occultation data  $M_{ij}$  has a Poisson random noise, we can analyze the accuracy of the fitted temperature and the fitted column density of  $O_2$  from the theory of error propagation,

$$\Delta X_l^2 = \sum_i \left\{ \sum_{M=1}^2 \alpha_{ln}^2 \left( \frac{\partial C_{ij}}{\partial X_m} \right)^2 \right\} \Delta M_{ij}^2 , \quad (2.19)$$

where  $\Delta M_{ij} = (M_{ij})^{1/2}$ .

The accuracy of the recovered number density of  $O_2$  depends upon the error in the column density and the technique used to invert the Abel integral. Here, we just use a simple linear matrix inversion technique to estimate the error. Writing Abel integral in a matrix form, one obtains

$$N_j = \sum_k W_{jk} n_k, \quad (2.20)$$

where  $n_k$  is the number density of  $O_2$  at altitude  $k$ , and  $W_{jk}$  is a geometric weighting function,

$$W_{jk} = 2 \int_{r_k - \Delta z/2}^{r_k + \Delta z/2} \frac{r}{\sqrt{r^2 - r_t^2}} dr \quad (2.21)$$

for a spherically symmetric atmosphere. Here  $\Delta z$  is the size of the altitude grid which the inversion is performed on. The errors in the inverted  $O_2$  number density,  $\Delta n_k$ , can then be estimated by

$$\Delta n_k^2 = \sum_j \omega_{kj}^2 \Delta N_j^2, \quad (2.22)$$

where  $\omega_{kj}$  is the element of the inverted matrix of  $W$ , and  $\Delta N_j$  is the error in the column density of  $O_2$  at tangent height  $j$  given by Eq. (2.19).

### 2.2.3 An Example: 39\_Lambda\_Orion

We consider an O-Type star, 39\_Lambda\_Orion, with a visual magnitude  $m_v$  of 3.39 to simulate the occultation sequence. The spectral irradiance of this star was measured, varying from  $\sim 1.5 \times 10^2$  photons/cm<sup>2</sup>/sec/Å near 40000 cm<sup>-1</sup> to  $2.5 \times 10^2$  photons/cm<sup>2</sup>/sec/Å near 60000 cm<sup>-1</sup> (Jamar, et al.). A constant value of  $2.0 \times 10^2$  photons/cm<sup>2</sup>/sec/Å is assumed in our simulation. The instrument parameters used are listed in Table 2.1, in which a specially coated CCD detector sensitive to ultraviolet radiation, is adopted.

**Table 2.1**  
**Ebert-Fastie Spectrometer Instrument Parameters**  
**Used in Stellar Occultation Simulation**

$A_0$	: 12.56 cm <sup>2</sup> (4 cm in diameter)
$T_r$	: 0.3
$Q_e$	: 0.20 (at $\sim 2000$ Å)
I.P.	: 1 second

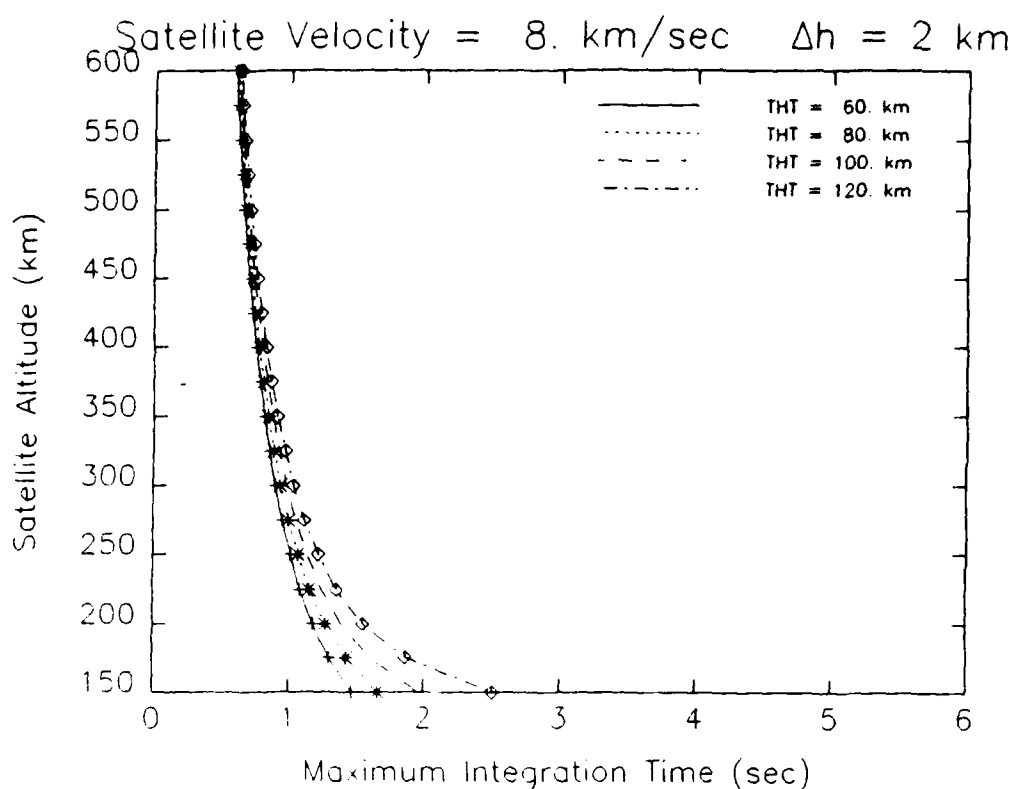


Figure 2.7

During a stellar occultation sequence, the rate at which the absorption path progresses deeper into the atmosphere is determined by the spacecraft orbital velocity and by the star location with respect to the orbital plane. In order to obtain a given vertical resolution in the recovered density profile, this rate limits the integration time allowed for an occultation measurement. Fig. 2.7 shows the time, or the maximum allowable integration period, computed for a star located on the orbital plane, during which the tangent ray height changes by 2 km as a function of satellite altitude. It varies from ~0.8 second at 60 km tangent altitude to ~1.1 seconds at 120 km tangent altitude for a satellite altitude of 300 km, and it increases as the star locates further away from the orbital plane. For our simulation we use an integration period of 1 second.

Fig 2.8 presents the results of simulated signal measurements at tangent ray altitudes of 60 km and 100 km for two instrument widths,  $50 \text{ cm}^{-1}$  (Fig. 2.8a) and  $1000 \text{ cm}^{-1}$  (Fig. 2.8b). Because the spectral region where total absorptions occur moves toward larger wavenumber (shorter wavelength) as the tangent height increases, we assume that the spectrometer steps its spectral coverage accordingly,  $150 \text{ cm}^{-1}$  per every 2 km. We have also included a noise of 40 counts to consider CCD detector read-out error. This noise value is insignificant for the low resolution measurements, but becomes statistically more important as the instrument width decreases. Although lower resolutions yield stronger signal levels, they result in a smaller number of spectral

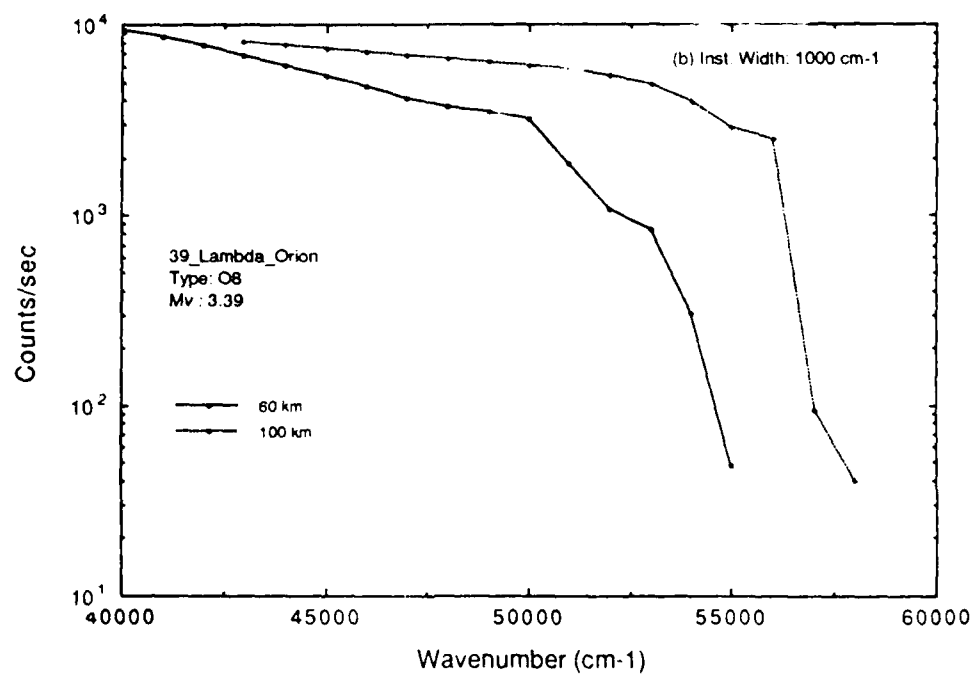
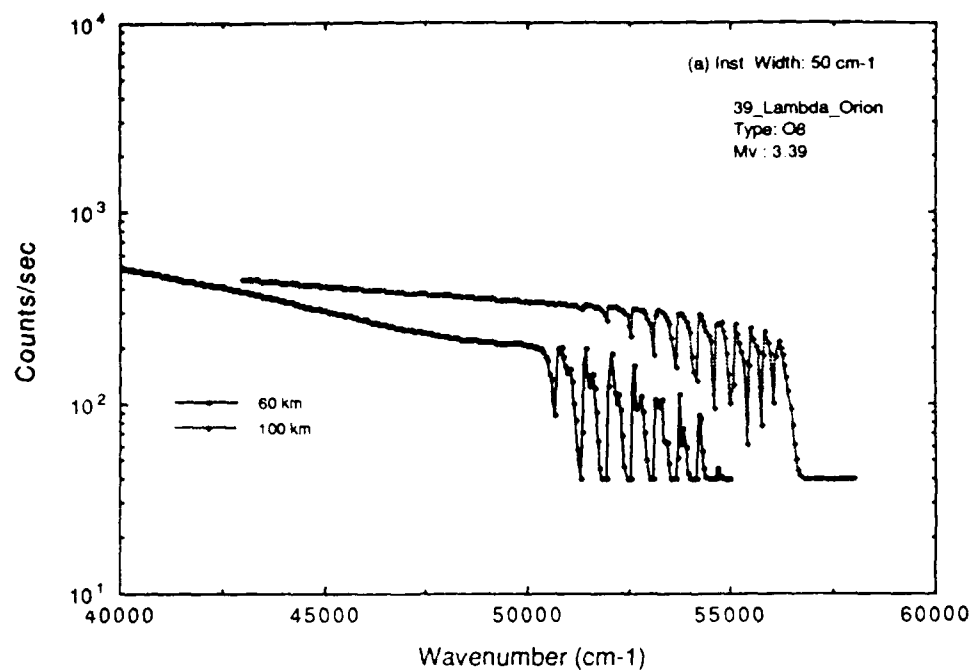


Figure 2.8

measurements and less resolution of the structure of the Schumann-Runge bands. Consequently, the estimation of the accuracies of the recovered density and temperature requires a complete statistical error analysis.

Fig. 2.9 illustrates the estimated percentage errors in the recovered density and temperature profiles based on the spectra shown in Fig. 2.8. It shows that the spectra obtained at  $50\text{ cm}^{-1}$  instrument width gives better determination of the densities and temperatures, less than 10 percent in density and 5 percent in temperature. Using spectra obtained at  $1000\text{ cm}^{-1}$  instrument width, however, we recover the density and temperature not only less accurately, but also with a large variability with altitude. This variability results directly from the change in temperature sensitivity as the spectral window shifts with tangent height. Also, as the tangent height moves above 100 km, the spectral window moves towards the Schumann-Runge continuum. Since the Schumann-Runge continuum is essentially temperature independent, this results in a gradual unretrievable loss of temperature information and an increasing error in the deduced temperature. At higher altitudes the technique becomes the one described by Hays and Roble (1973), where only a single wavelength, photometric measurement is needed. The  $\text{O}_2$  column density can then be easily obtained with an improved accuracy.

### 2.3 Summary and Discussion

A stellar occultation technique is presented for the determination the atmospheric density profile in the critical 60 to 120 km region from the  $\text{O}_2$  absorption spectra near the Herzberg continuum, Schumann-Runge bands, and Schumann-Runge continuum. Because the absorption cross-sections in the Schumann-Runge bands are temperature dependent, the data reduction technique is different from the ones used in the past. Multi-wavelength spectrometric measurements of the occultation spectra permits the simultaneous determination of the atmospheric temperature profile.

Using a simulated CCD Ebert-Fastie Spectrometer, we have demonstrated the feasibility of this technique and estimated the statistical accuracy in the recovered density and temperature profiles. The errors are estimated based on an instrument whose parameters are described in Table 2.1 and a source star, 39\_Lambda\_Orion, which has a spectral irradiance of  $\sim 200\text{ photons/cm}^2/\text{sec}/\text{\AA}$  near the ultraviolet spectral region. We have shown that the  $\text{O}_2$  density profile can be recovered with a statistical accuracy of less than 10 percent. Note that, while  $\alpha$  in Eq. (2.19) is inversely proportional to the square of the instrument sensitivity  $S$  and the star intensity,  $I_0$ ,  $\partial C_{ij}/\partial X$  and  $M_{ij}$  are proportional to  $S$  and  $I_0$ . As a result, the error in the recovered column density is inversely

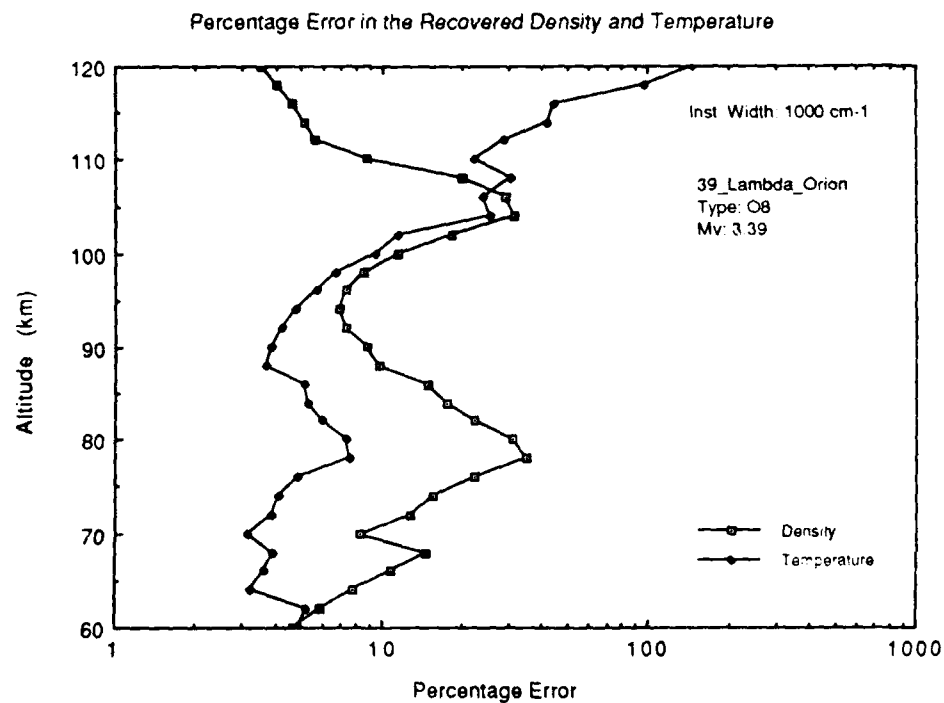
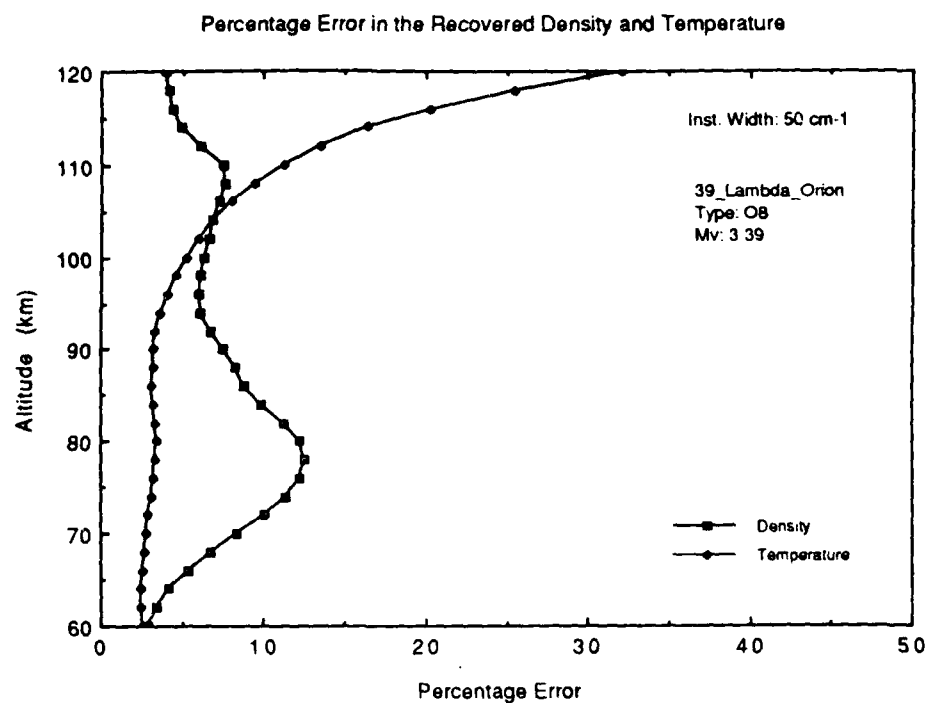


Figure 2.9

proportional to the square root of  $S$  and  $I_0$ . Thus an occultation experiment performed on a source star other than 39\_Lambda\_Orion would produce different observed signal,  $M_{ij}$ , and results in different errors in the  $O_2$  number density profile. Similarly, one can also improve the accuracy by designing an instrument with a larger telescope aperture in order to increase the instrument sensitivity. Fig. 2.10 shows the telescope diameter required in order to recover density with the same accuracy demonstrated here for various star temperatures and visual magnitudes. There are approximately 500 stars of visual magnitude 4.0 or brighter and of these, about 40% are in the spectral classes of O and B which have an effective temperature greater than 15,000K. A telescope size similar to the one used in this simulation is therefore enough to carry out the occultation experiment. Of course, this size is governed by the accuracy requirement in the recovered density profile and the distribution of stars near the orbital plane of the spacecraft.

There has recently been some interest in the role of photodissociation of isotopic oxygen in the production of ozone. The two isotopes of oxygen are  $O_{16}O_{18}$  with an abundance of 0.41% of  $O_{16}O_{16}$ , and  $O_{16}O_{17}$  with ~20% of the  $O_{16}O_{18}$  abundance. Although the isotopes differ slightly in

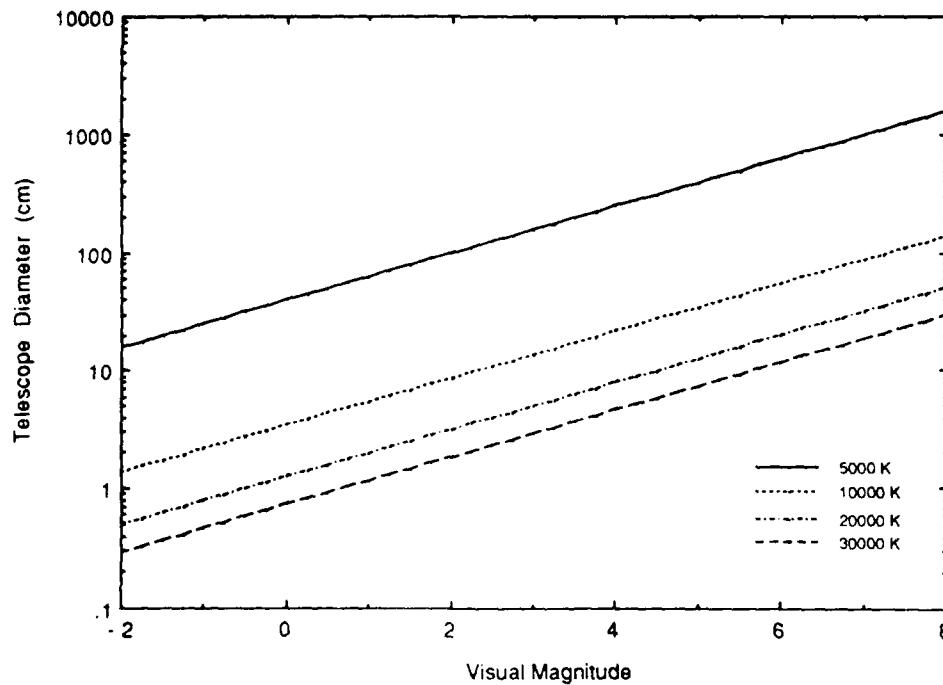


Figure 2.10



mass, they have quite different absorption properties from the ordinary oxygen molecules. The fact that the isotopes have twice as many lines does not increase the amount of absorption because the population of the initial rotational line also decreases by about 1/2. It is that the possibility of overlapping of lines and the variation of tangent altitude where the total absorption occurs might have some effect on our analysis. Because of the relatively small abundance of the isotope, we believe that the effect is small. However, it is still interesting enough to be worthy of further investigation.

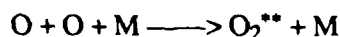
Although we have only simulated the occultation process for the altitude region between 60 and 120 km, this technique can also be used to obtain the  $O_2$  density profile above 120 km by measuring the absorption in the Schumann-Runge continuum (Roble and Hays, 1973). Near 60 km tangent height and below, however, the absorption by ozone in the Hartley bands becomes important. Ozone has a peak absorption cross-section of the order of  $10^{-17} \text{ cm}^2$  near  $40000 \text{ cm}^{-1}$ , giving an optical depth of 1.0 at approximately 65 km. Therefore, the technique presented here will work well in the region above 70 km. Between 60 and 70 km only the occultation data at  $\nu > 45,000 \text{ cm}^{-1}$  are useful and should be analyzed with extreme care.

There are many techniques which can be used to retrieve the density and temperature profiles from the occultation data. A method which first filters out the temperature dependence of the cross-section and obtains the column density of  $O_2$  for each tangent height was demonstrated. The systematic error caused by this approximation is believed to be very small. In fact, considering the rate of data acquisition, we believe that this technique is ideal because of its simplicity and efficiency.

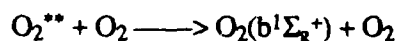
### 3. RESONANCE FLUORESCENCE OF O<sub>2</sub>

The Atmospheric bands of molecular oxygen originate in a transition between the excited  $b^1\Sigma_g^+$  state and the ground  $X^3\Sigma_g^-$  state. The emissions were first discovered by Meinel (1950) in the nightglow spectra shortly after the discovery of OH bands. Since then there has been an extensive set of observational data under nighttime and auroral conditions. The (0-0) band of the O<sub>2</sub> atmospheric system is completely absorbed by the lower atmosphere and can only be observed from altitudes above the stratosphere. As a result, all the ground-based measurements have been made on the (0-1) and (1-1) bands (Meinel, 1951; Chamberlain, et al, 1954; Wallace and Chamberlain, 1959), and the (0-0) band emissions were only observed by instruments on board rockets (Packer, 1961; Deans et al., 1976; Witt et al., 1979; McDade et al., 1986) and the shuttle (Torr et al., 1985).

Wallace and Hunten (1968) first observed the dayglow O<sub>2</sub> (0-0) and (0-1) bands with rocket-borne photometers and spectrometers in the altitude range between 39-128 km. In their classic paper, they presented what have become an accepted theory of the excitation mechanisms for the O<sub>2</sub>( $b^1\Sigma_g^+$ ) molecules: resonance fluorescence process in the region between 70 and 100 km and energy transfer reaction between O(<sup>1</sup>D) and O<sub>2</sub>, with the O(<sup>1</sup>D) atoms produced in Schumann-Runge O<sub>2</sub> dissociation above 100 km, and those produced in the Hartley dissociation of ozone near 45 km. They included a direct contribution from the photolysis of ozone, which later was found to be ineffective (Gauthier and Snelling, 1970, 1971). In order to account for an excess emission near 90 km, Wallace and Hunten (1968) also postulated a small three-body recombination or Chapman type chemical source. This chemical source is mainly responsible for the Atmospheric band emissions in the nightglow, and its exact mechanisms have been debated for many years. Later studies suggested the Barth mechanism, in which a two-step process is involved,



followed by



(Campbell and Gray, 1973; Greer et al., 1981; Slanger and Black, 1977).

The O<sub>2</sub> Atmospheric bands are one of the brightest emission features that are seen in the visible and near infra-red region of the airglow spectra. The total band brightness is strongly coupled to the O<sub>2</sub>

density through both the excitation mechanisms and the self-absorption processes (for the 0-0 band), with the brightness of each rotational line determined by the atmospheric temperature. Here we will describe how the observed intensities of the O<sub>2</sub> Atmospheric bands are used to retrieve the O<sub>2</sub> number density and temperature profiles in the region between 60 and 120 km.

### 3.1 The O<sub>2</sub> Atmospheric Bands

#### 3.1.1 Spectral Intensity of the Atmospheric bands

Fig. 3.1 shows the viewing geometry of a spacecraft-borne instrument measuring limb brightnesses of the O<sub>2</sub> Atmospheric band emissions. The measured brightness is an integrated volume emission rate along the slant path associated with a particular tangent ray altitude. When the absorption is important, such as the O<sub>2</sub> Atmospheric (0-0) band, the measured brightness is modified by the attenuation along the path between production region and the spacecraft.

If we denote the total band volume emission rate at a point along the line of sight by  $\eta(s)$ , the

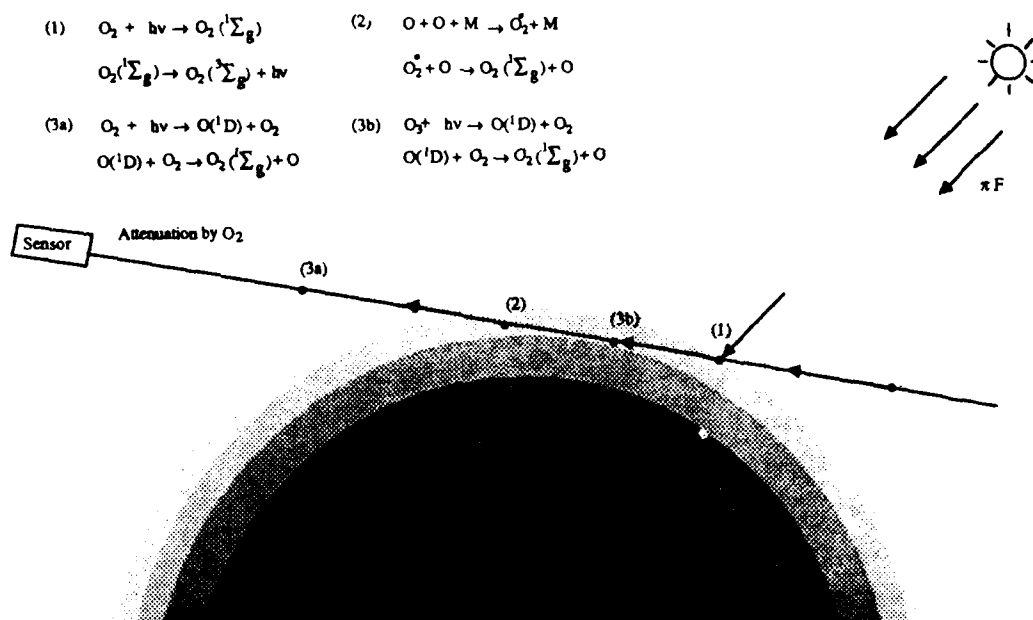


Figure 3.1

observed spectral brightness,  $B(v, z_t)$ , of a rotational line at  $v_j$  as a function of wavenumber  $v$  and tangent height  $z_t$  is given by

$$B(v, z_t) = \int_{-\infty}^{\infty} \eta(s) f(s) D(v, s) \exp \left\{ - \int_s^{\infty} n(s') \sigma(s') D(v, s') ds' \right\} ds \quad (3.1)$$

where  $f(s)$  is the line strength of the rotation line of interest, determined by the rotational temperature of the excited  $O_2(b^1\Sigma_g^+)$  molecules and  $\sum_{\text{all lines}} f = 1.0$ ,  $D(v, s)$  is the line shape at temperature  $T(s)$ ,  $n(s')$  is the number density of  $O_2$ , and  $\sigma(s)$  is the self-absorption cross-section.

Converting the line-of-sight integral in Eq.(3.1) to an integral in altitude  $z$ , one obtains

$$B(v, z_t) = \int_{z_t}^{\infty} \eta(z) f(z) D(v, z) W(z, z_t) \exp \{-\Gamma(v, z, z_t)\} dz \quad (3.2)$$

$$+ \int_{z_t}^{\infty} \eta(z) f(z) D(v, z) W(z, z_t) \exp \{-\Gamma(v, z_t, z_t) - \tau(v, z, z_t)\} dz$$

where  $W(z, z_t)$  is the Jacobian in the transformation ( $W = \partial s / \partial z$ ), or the geometric weighting function,

$$W(z, z_t) = \frac{R_e + z}{\sqrt{(R_e + z)^2 - (R_e + z_t)^2}}, \quad (3.3)$$

where  $R_e$  is earth radius, and

$$\Gamma(v, z, z_t) = \int_z^{\infty} n(z') \sigma(z') D(v, z') W(z', z_t) dz', \quad (3.4)$$

$$\tau(v, z, z_t) = \int_{z_t}^z n(z') \sigma(z') D(v, z') W(z', z_t) dz'. \quad (3.5)$$

Since

$$\Gamma(v, z, z_t) = \Gamma(v, z_t, z_t) - \tau(v, z, z_t), \quad (3.6)$$

and by defining

$$\Gamma(v, z_t) = \Gamma(v, z_t, z_t), \quad (3.7)$$

we can rewrite Eq. (3.2) as

$$B(v, z_t) = 2 \int_{z_t}^{\infty} \eta(z) f(z) D(v, z) W(z, z_t) \exp[-\Gamma(v, z_t)] \cosh[\tau(v, z, z_t)] dz. \quad (3.8)$$

The above equation computes the spectral brightness,  $B(v, z_t)$ , of any given rotational line when the self-absorption process is considered. Since  $f$ ,  $D$  and  $\sigma$  are a function of temperature the spectral brightness in this case not only depends upon the band volume emission rate and the  $O_2$  number density profiles, but also on the atmospheric temperature profile. For emissions that the self-absorption process is not important, such as the  $O_2$  Atmospheric (0-1) and (1-1) bands, Eq. (3.8) becomes the Abel integral equation (Hays et al., 1973),

$$B(v, z_t) = \int_{z_t}^{\infty} \eta(z) f(z) D(v, z) W(z, z_t) dz, \quad (3.9)$$

and the spectral brightness is determined by the volume emission rate and the atmospheric temperature profiles.

### 3.1.2 Characteristics of the $O_2$ Atmospheric Band Emission

#### *$O_2$ Atmospheric band Volume Emission Rate*

If we denote the various sources of production of  $O_2(b^1\Sigma_g^+)$  by  $P_{res}$ ,  $P_{O(1D)}$  and  $P_{chem}$  and consider loss processes due to quenching and radiation in a simple photochemical equilibrium situation, we can determine the total band volume emission rate as a function of altitude,

$$\eta_{v-v''}(z) = A_{v-v''} Q(v') \frac{P_{res} + P_{O(1D)} + P_{chem}}{A_{1_2} + k_{N_2} n_{N_2}(z) + k_{O_2} n_{O_2}(z)}, \quad (3.10)$$

where  $A_{v,v'}$  is the transition probability between  $O_2(b^1\Sigma, v')$  and  $O_2(X^3\Sigma, v'')$  states,  $A_{1\Sigma}$  is the transition probability of  $O_2(b^1\Sigma)$  state, and  $kN_2$  and  $kO_2$  are the quenching rate coefficients of  $O_2(b^1\Sigma)$  by  $N_2$  and  $O_2$  respectively.

Fig. 3.2 shows the volume emission rate profile of the (0,0) band in the daytime and its individual contribution due to each of the three production sources (Bucholtz et al., 1986). Note that the dominant sources of the excited  $O_2(b^1\Sigma)$  molecules in the 60 to 130 km range are resonance scattering and reaction of  $O(^1D)$  atom with  $O_2$  followed by photodissociation of  $O_2$ . In a region above ~90 km where quenching of  $O_2(b^1\Sigma)$  molecules is not important, the volume emission rate is therefore related to the number density of ground state  $O_2$ . As the quenching becomes important in the region between 60 and 90 km, the production rate and the loss rate of  $O_2(b^1\Sigma_g^+)$  are both proportional to the molecular oxygen number density. As a result, the total band volume emission rate remains independent with altitude, and provides little information about the number density of  $O_2$ . The capability of retrieving atmospheric density in this region lies not on the volume emission rate profile, but on the important characteristics of the (0-0) band, the self absorption processes. Here the volume emission rate profile computed by Bucholtz et al. (1986) and a model atmosphere listed in Table 3.1 are used in our study.

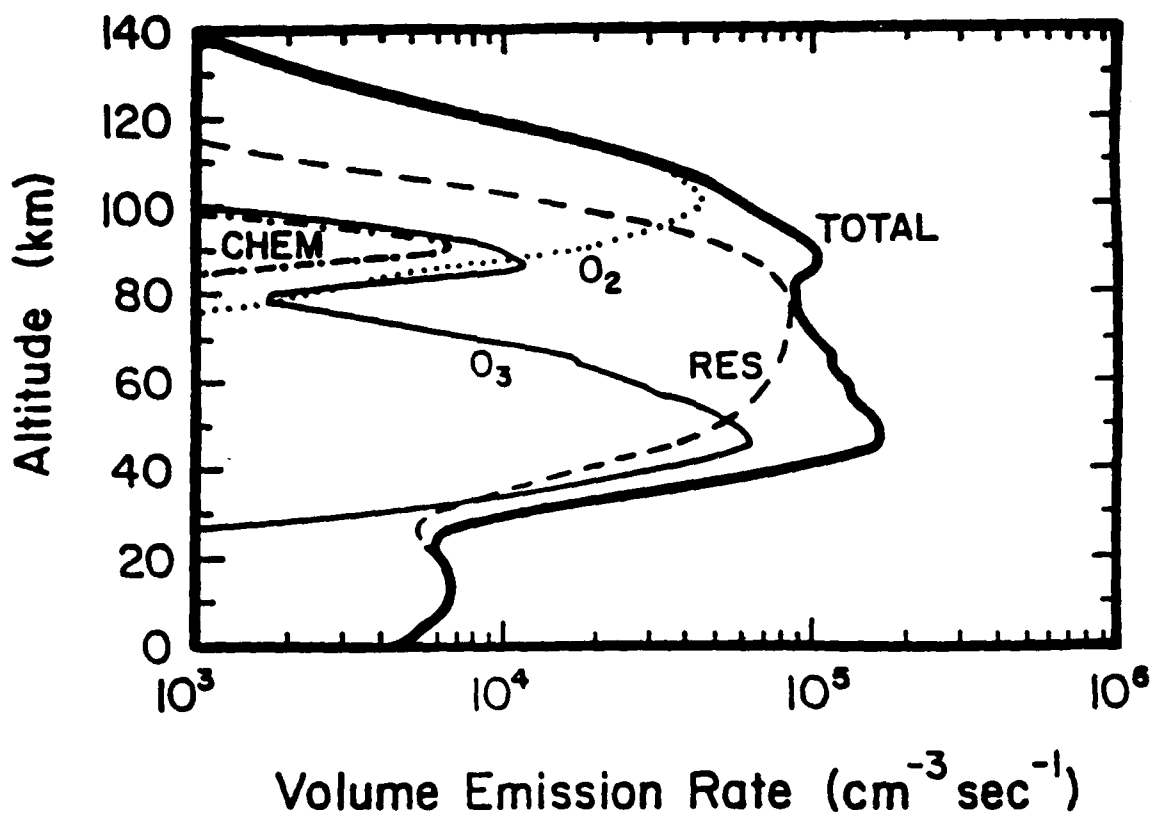


Figure 3.2

TABLE 3.1

<u>Altitude(km)</u>	<u>Temperature(K)</u>	<u>n(O<sub>2</sub>)</u>	<u>O<sub>2</sub>(0-0) band n(photons/cm<sup>3</sup>/sec)</u>	<u>Contiuum emission n(photons/cm<sup>3</sup>/sec/Å)</u>
60.0	252.4972	1.49 (15)	7323.35	7.47 (1)
62.0	244.3	1.18 (15)	7133.66	5.49 (1)
64.0	236.0	9.26 (14)	7089.15	4.04 (1)
66.0	227.8	7.19 (14)	7113.96	2.97 (1)
68.0	219.5	5.54 (14)	6934.56	2.18 (1)
70.0	211.2	4.22 (14)	6804.00	1.60 (1)
72.0	208.4	3.11 (14)	6653.63	1.18 (1)
74.0	205.3	2.28 (14)	6553.28	8.66 (0)
76.0	202.4	1.67 (14)	6468.28	6.37 (0)
78.0	199.5	1.22 (14)	6370.40	4.68 (0)
80.0	196.6	8.86 (13)	6281.98	3.44 (0)
82.0	193.5	6.39 (13)	6222.41	2.53 (0)
84.0	190.1	4.60 (13)	6278.27	1.86 (0)
86.0	188.6	3.24 (13)	6440.33	1.36 (0)
88.0	186.7	2.25 (13)	6570.99	1.00 (0)
90.0	183.8	1.54 (13)	6488.03	0.73 (0)
92.0	186.1	1.05 (13)	6086.06	0.54 (0)
94.0	187.9	7.15 (12)	5611.43	0.39 (0)
96.0	186.8	4.55 (12)	5134.98	0.29 (0)
98.0	189.3	2.75 (12)	4751.40	0.21 (0)
100.0	196.3	1.92 (12)	4424.45	0.15 (0)
102.0	205.7	1.26 (12)	4061.11	0.11 (0)
104.0	216.5	8.41 (11)	3653.11	8.58(-2)
106.0	228.4	5.63 (11)	3229.26	6.30(-2)
108.0	240.8	3.80 (11)	2786.08	4.63(-2)
110.0	253.7	2.59 (11)	2309.08	3.40(-2)
112.0	267.4	1.77 (11)	1822.02	2.50(-2)
114.0	283.4	1.22 (11)	1370.23	1.84(-2)
116.0	305.1	8.42 (10)	987.13	1.35(-2)
118.0	334.7	5.80 (10)	692.65	9.95(-3)
120.0	363.7	4.12 (10)	490.63	7.31(-3)
122.0	391.1	3.02 (10)	335.93	5.38(-3)
124.0	417.2	2.27 (10)	247.80	3.95(-3)
126.0	442.1	1.75 (10)	186.91	2.90(-3)
128.0	465.8	1.38 (10)	144.05	2.13(-3)
130.0	488.3	1.11 (10)	113.21	1.57(-3)
132.0	509.8	9.06 (9)	90.53	1.15(-3)
134.0	530.2	7.49 (9)	73.48	8.49(-4)
136.0	549.7	6.26 (9)	60.41	6.24(-4)
138.0	568.2	5.29 (9)	50.20	4.58(-4)
140.0	585.8	4.50 (9)	42.10	3.37(-4)

### Temperature Effect

The spectral brightness of any given rotational line depends on the atmospheric temperature profile in two different ways. One is the thermal distribution of the rotational levels of both the emitter, the excited  $O_2(b^1\Sigma_g^+)$  and the absorber, the ground state  $O_2(X^3\Sigma_g^-)$ . The former determines the line volume emission rate profile, while the latter determines the line absorption cross-section (McClatchey et al., 1973),

$$f = f_s \frac{T_s}{T} \exp \left\{ \frac{1.439 E' (T - T_s)}{T T_s} \right\}, \quad (3.11)$$

$$\sigma = \sigma_s \frac{T_s}{T} \exp \left\{ \frac{1.439 E'' (T - T_s)}{T T_s} \right\}, \quad (3.12)$$

where  $f_s$  is the emission line strength at standard temperature  $T_s$ ,  $\sigma_s$  is the self-absorption cross-section at  $T_s$ , and  $E'$  and  $E''$  are the energies in  $\text{cm}^{-1}$  for the upper and lower states of the rotational line respectively (Babcock and Herzberg, 1948).

Fig. 3.3 presents the rotational line intensity distributions of the  $O_2$  Atmospheric (0-1) band for temperatures of 150 and 300°K respectively. The band origin is located near 8645Å with the R-branch lines appearing on the shorter wavelengths side and the P-branch lines appearing on the longer wavelength side. Because collisions with the ambient atmospheric particles are very frequent in the region between 60 and 120 km, both the excited and the ground states of  $O_2$  are in rotational thermal equilibrium and have a rotational temperature equal to the ambient kinetic temperature. As the temperature increases, the lines near the bandhead and the bandtail, representing the transitions from higher rotational levels, become more pronounced. This apparent change in band structure can provide us with the temperature information of the atmosphere.

If the self-absorption process is important, such as for the  $O_2$  Atmospheric (0-0) band emission, the band structure will be modified due to variations in extinction from line to line. Fig.3.4a shows the computed intensities of all the rotational lines in the  $O_2$  Atmospheric (0-0) band at 60 km tangent height, and Fig. 3.4b shows the case when the self-absorption process is ignored. The effect of the self-absorption process is small for the lines near the bandhead and the bandtail whose line strengths are weak, and is large for lines near the band origin. The temperature deduced from the rotational band structure of the  $O_2$  Atmospheric (0-0) band emission therefore is larger than the rotational temperature of the emitters.



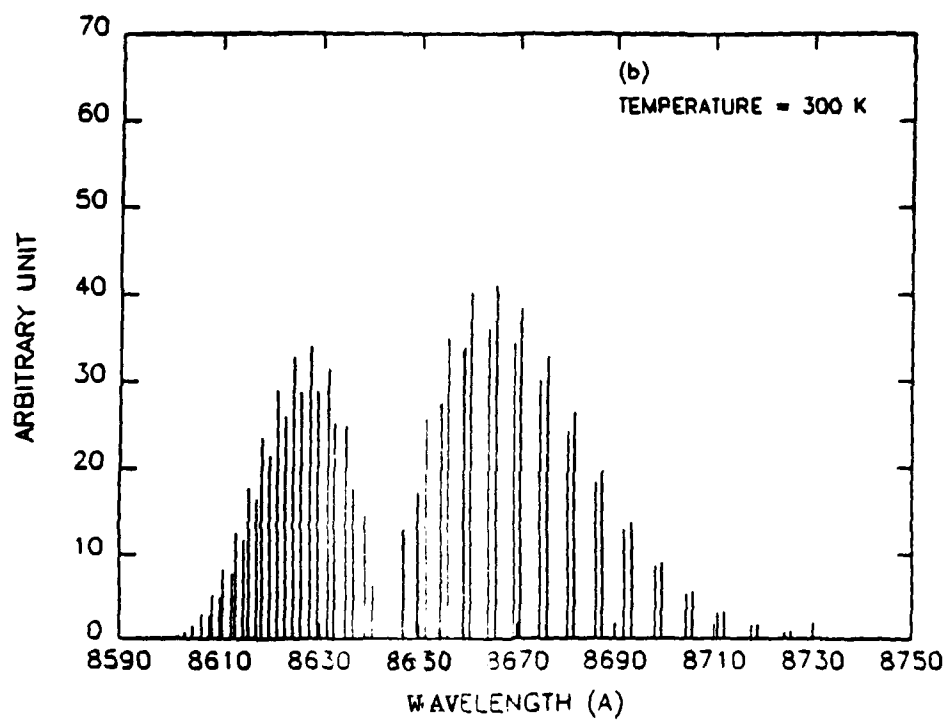
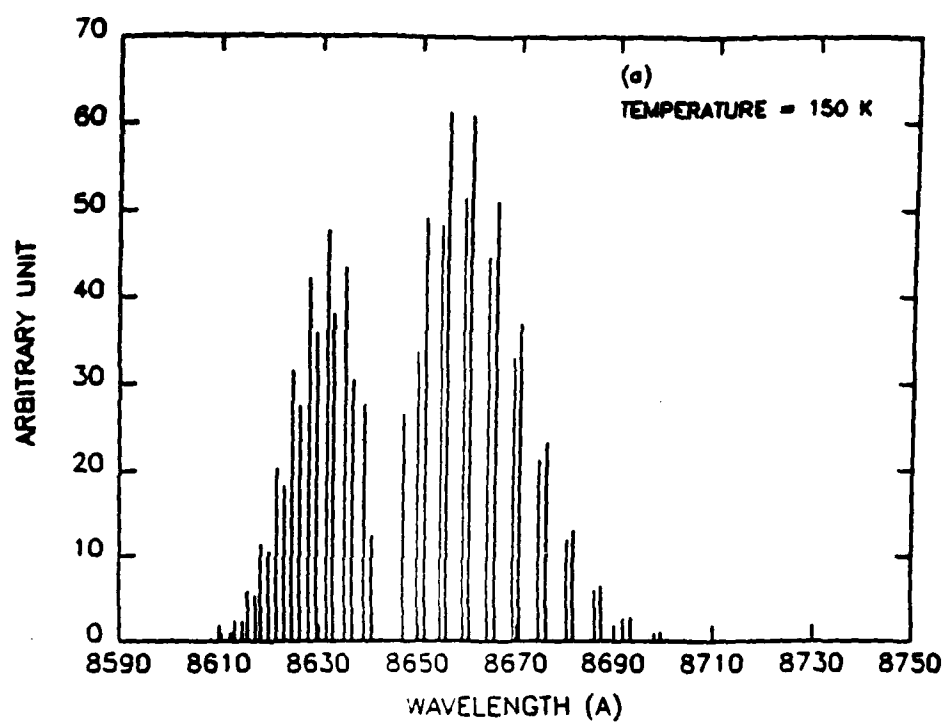


Figure 3.3

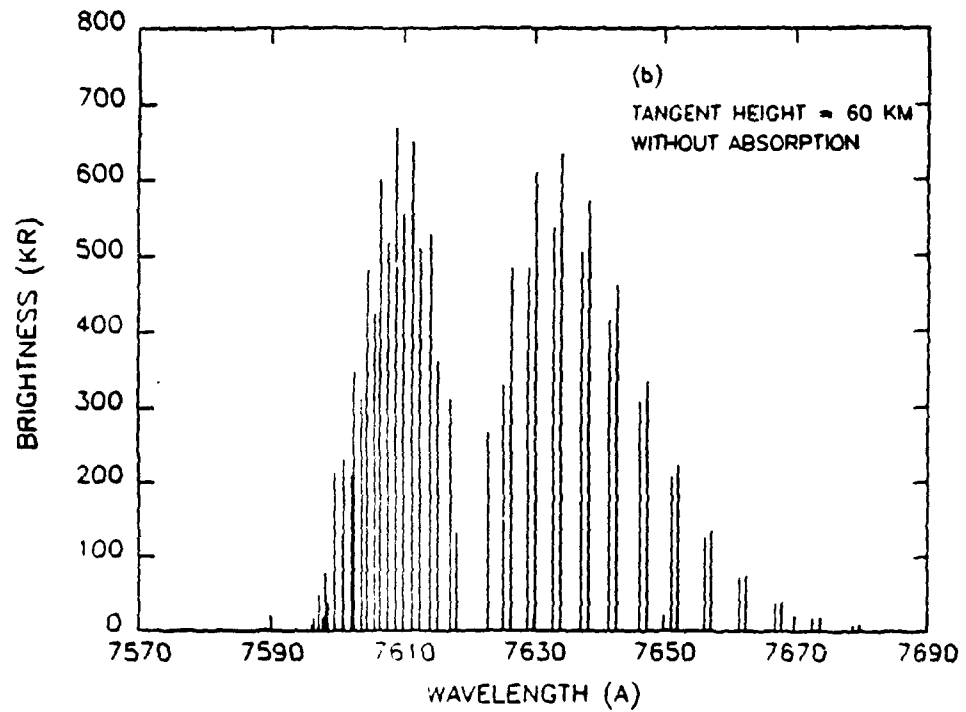
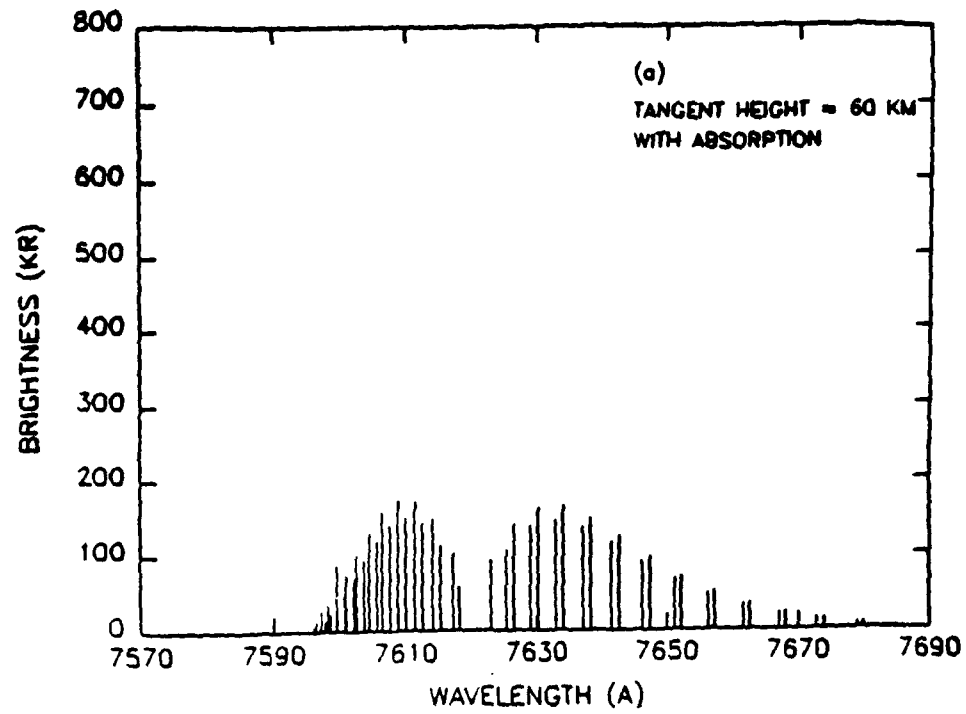


Figure 3.4

The other temperature dependence arises when the spectral line shapes of the emission and the absorption cross-section are considered. In the region above 60 km the pressure broadening effect is not very important. The spectral shapes of the emission line and the self-absorption cross-section are determined by the kinetic temperatures of the excited state  $O_2(b^1\Sigma_g^+)$  and the ground state  $O_2(X^3\Sigma_g^-)$  respectively,

$$D(\nu, T) = \frac{1}{\alpha_D} \left( \frac{\ln 2}{\pi} \right)^{\frac{1}{2}} \exp \left( -\frac{(\nu - \nu_0)^2 \ln 2}{\alpha_D^2} \right), \quad (3.13)$$

where  $\nu_0$  is the wavenumber at line center, and  $\alpha_D$  is the doppler width,

$$\alpha_D = \frac{\nu_0}{c} \left( \frac{2kT \ln 2}{m} \right)^{\frac{1}{2}}. \quad (3.14)$$

Fig. 3.5 shows the emission line shape of line  $^{PP}11$  ( $13118.0332 \text{ cm}^{-1}$ ) in the (0-0) band for a measurement at a tangent height of 60 km. The emission line shape for neglecting the self-absorption process is also shown. Since the magnitude of the self-absorption cross-section is the

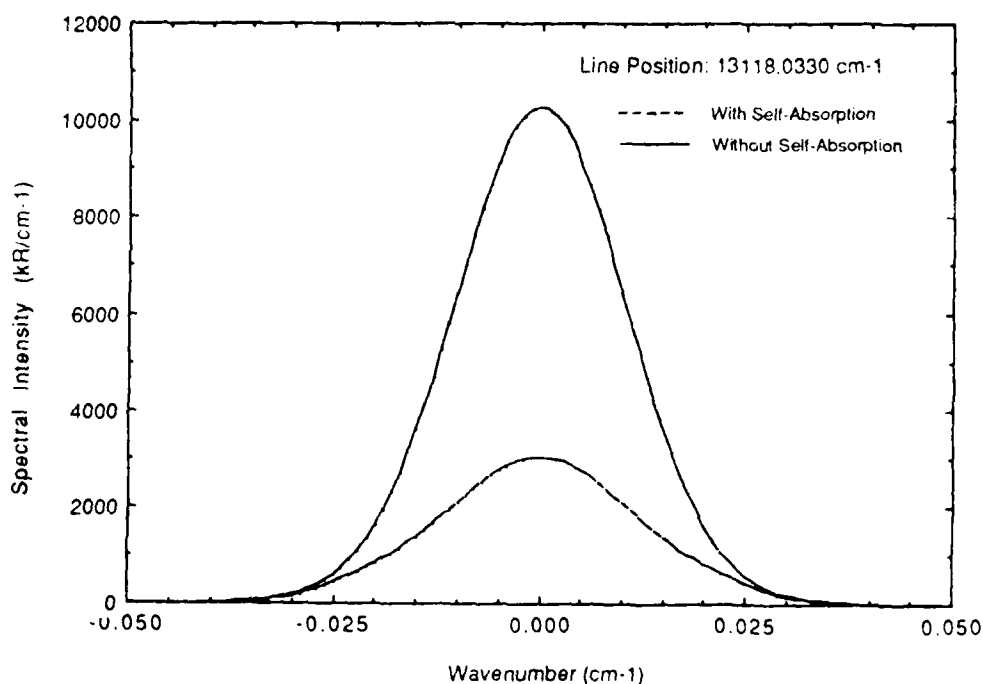


Figure 3.5

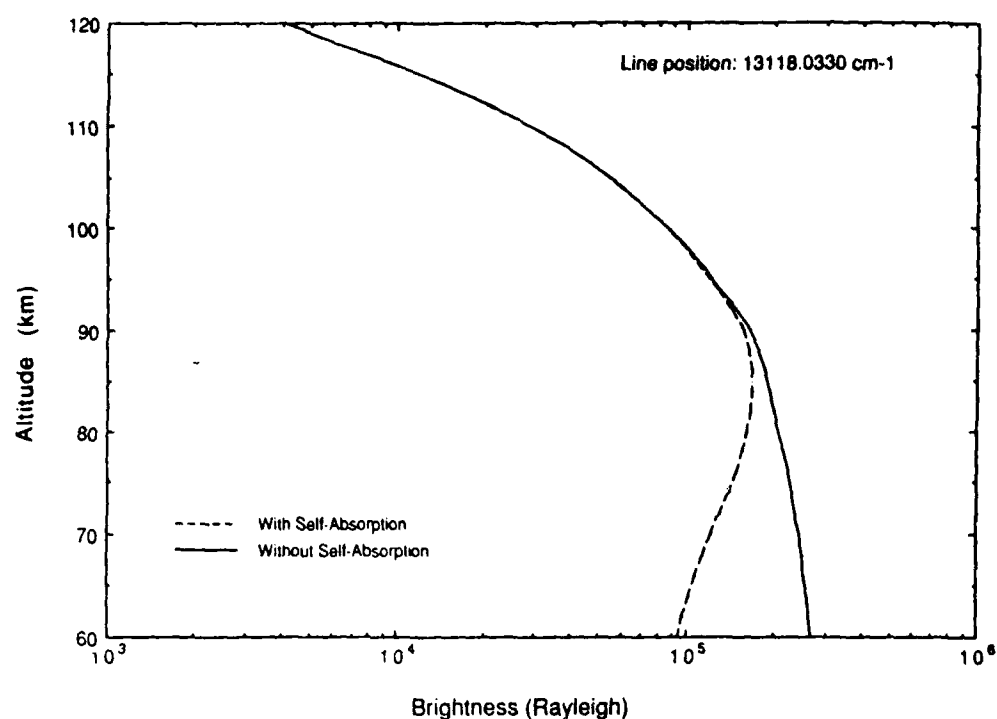


Figure 3.6

largest at the line center and decreases toward the wings, the effect of the self-absorption process gives rise to a broadened emission line shape and an effective temperature larger than the kinetic temperature of the emitters.

#### *O<sub>2</sub> number density*

One would also expect that emission spectral line shape at lower tangent heights will appear broader than the ones at higher tangent heights due to longer absorption paths and the larger extinctions near the line center. Consequently, the spectral intensity of lines in the (0-0) band not only contains the temperature information of the emitter, but also the column density of the absorber O<sub>2</sub>.

Fig. 3.4 clearly shows that for some rotational lines, approximately 60-80% of the intensities are absorbed. Fig. 3.6 presents the intensity as a function of tangent height for the line shown in Fig. 3.5. The variation of the amount of self-absorption with tangent height reflects the variation of the O<sub>2</sub> column density. Hence, by measuring the extinction of the O<sub>2</sub>(0-0) band emission intensity as a function of tangent height, one can, in principle, determine the number density profile of O<sub>2</sub>.

## 3.2 Recovery of Density and Temperature Profiles

### 3.2.1 Mathematical formulation

As the Eq.(3.8) indicates, the observed limb brightness  $B(v, z_l)$  of an emission line in the  $O_2$  Atmospheric (0-0) band is a non-linear function of the volume emission rate, temperature, and the  $O_2$  number density profiles. Using linear perturbation theory, we can express actual  $n(z)$ ,  $T(z)$ , and  $\eta(z)$  profiles as sums of guessed profiles,  $n_o(z)$ ,  $T_o(z)$  and  $\eta_o(z)$  and small perturbations  $n'(z)$ ,  $T'(z)$  and  $\eta'(z)$ , as follows:

$$n(z) = n_o(z) + n'(z), \quad (3.15)$$

$$T(z) = T_o(z) + T'(z), \quad (3.16)$$

and

$$\eta(z) = \eta_o(z) + \eta'(z). \quad (3.17)$$

We shall see below that Eq. (3.8) can be simplified, expressing any observed limb brightness in terms of a linear combination of the volume emission rate, temperature and the  $O_2$  number density profiles. The linear representation of the limb brightness can help us understand the relative importance or the contribution of the three parameters to the observed brightness.

Substituting Eqs. (3.15), (3.16) and (3.17) into the expressions for  $\Gamma(v, z_l)$  and  $\tau(v, z, z_l)$  and neglecting the terms involving the multiplication of two perturbations parameters, one obtains

$$\Gamma(v, z_l) = \Gamma_o(v, z_l) + \Gamma'_T(v, z_l) + \Gamma'_n(v, z_l), \quad (3.18)$$

and

$$\tau(v, z, z_l) = \tau_o(v, z, z_l) + \tau'_T(v, z, z_l) + \tau'_n(v, z, z_l), \quad (3.19)$$

where

$$\Gamma'_o(v, z_l, z_l) = \int_{z_l}^{\infty} n_o(z) \sigma_o(z) D_o(v, z) W(z, z_l) dz, \quad (3.20)$$

$$\Gamma'_T(v, z_l) = \int_{z_l}^{\infty} n_o(z) \frac{\partial(\sigma_o(z) D_o(v, z))}{\partial T} T'(z) dz, \quad (3.21)$$

$$\Gamma'_n(v, z_l) = \int_{z_l}^{\infty} n'(z) \sigma_o(z) D_o(v, z) W(z, z_l) dz, \quad (3.22)$$

and

$$\tau_o(v, z, z_l) = \int_{z_l}^z n_o(z) \sigma_o(z) D_o(v, z) W(z, z_l) dz, \quad (3.23)$$

$$\tau'_T(v, z, z_l) = \int_{z_l}^z n_o(z) \frac{\partial(\sigma_o(z) D_o(v, z))}{\partial T} T'(z) W(z, z_l) dz, \quad (3.24)$$

$$\tau'_n(v, z, z_l) = \int_{z_l}^z n'(z) \sigma_o(z) D_o(v, z) W(z, z_l) dz. \quad (3.25)$$

The terms  $e^{-\Gamma}$  and  $\cosh(\tau)$  in Eq. (3.8) can then be expanded as

$$e^{-\Gamma} = e^{-\Gamma_o} (1 - \Gamma'_T - \Gamma'_n), \quad (3.26)$$

$$\cosh(\tau) = \cosh(\tau_o) + (\tau'_T + \tau'_n) \sinh(\tau_o), \quad (3.27)$$

and Eq. (3.8) becomes

$$\begin{aligned} B(v, z_l) = & B_o(v, z_l) + \int_{z_l}^{\infty} [\tau'_T(v, z, z_l) \alpha(v, z, z_l) - \Gamma'_T(v, z_l) \beta(v, z, z_l)] dz \\ & + \int_{z_l}^{\infty} [\tau'_n \alpha(v, z, z_l) - \Gamma'_n \beta(v, z, z_l)] dz + \int_{z_l}^{\infty} T'(z) \gamma(v, z, z_l) dz \\ & + \int_{z_l}^{\infty} \eta'(z) \delta(v, z, z_l) dz, \end{aligned} \quad (3.28)$$

where

$$B_o(v, z_l) = \int_{z_l}^{\infty} 2\eta_o(z) f_o(z) D_o(v, z) W(z, z_l) \exp \{-\Gamma_o(v, z_l)\} \cosh [\tau_o(v, z, z_l)] dz, \quad (3.29)$$

and

$$\alpha(v, z, z_t) = 2\eta_0(z) f_0(z) D_0(v, z) W(z, z_t) \exp \{-\Gamma_0(v, z_t)\} \sinh [\tau_0(v, z, z_t)], \quad (3.30)$$

$$\beta(v, z, z_t) = 2\eta_0(z) f_0(z) D_0(v, z) W(z, z_t) \exp \{-\Gamma_0(v, z_t)\} \cosh [\tau_0(v, z, z_t)], \quad (3.31)$$

$$\gamma(v, z, z_t) = \beta(v, z, z_t) \left[ \frac{1}{D_0(v, z)} \frac{\partial D_0}{\partial T} + \frac{1}{f_0(z)} \frac{\partial f_0}{\partial T} \right], \quad (3.32)$$

$$\delta(v, z, z_t) = \beta(v, z, z_t) / \eta_0(z). \quad (3.33)$$

Here, the derivatives of  $f(T)$  and  $D(v, T)$  with respect to temperature  $T$  can be easily obtained from Eq. (3.11) and (3.13),

$$\frac{1}{f} \frac{\partial f}{\partial T} = \left\{ -\frac{1}{T} + \frac{1.439 E'}{T^2} \right\}, \quad (3.34)$$

$$\frac{1}{D} \frac{\partial D}{\partial T} = \frac{1}{2T} \left\{ \frac{2 \ln 2 (v - v_0)^2}{\alpha_D^2} - 1 \right\}. \quad (3.35)$$

Expressing the integration in Eq. (3.28) for a given tangent height measurement  $i$  in a form of matrix summation, one obtains

$$B_i(v) = B_{io}(v) + \sum_{k=1}^m \left( \frac{n_k'}{n_k} \right) X_{ik} + \sum_{k=1}^m T_k' Y_{ik} + \sum_{k=1}^m \left( \frac{\eta_k'}{\eta_k} \right) Z_{ik}, \quad (3.36)$$

where

$$B_{io} = \sum_{k=1}^m \beta_{ik}, \quad (3.37)$$

$$X_{ik} = n_k \sigma_k D_k W_{ik} \left[ \sum_{j=1}^m \alpha_{ij} - \sum_{j=1}^m \beta_{ij} \right], \quad (3.38)$$

$$Y_{ij} = n_k \sigma_k D_k W_{ik} \left[ \sum_{j=1}^m \alpha_{ij} - \sum_{j=1}^m \beta_{ij} \right] \frac{1}{\sigma_k D_k} \frac{\partial(\sigma_k D_k)}{\partial T} + \gamma_{ik}, \quad (3.39)$$

$$Z_{ik} = \beta_{ij}, \quad (3.40)$$

and

$$\frac{1}{\sigma D} \frac{\partial(\sigma D)}{\partial T} = -\frac{1}{T} + \frac{1.439 E''}{T^2} + \frac{1}{2T} \left[ \frac{2 \ln 2 (v - v_0)^2}{\alpha_D^2} - 1 \right]. \quad (3.41)$$

Note that  $B_i'(v)$  is wavenumber dependent, and for an instrument with transmission function  $I(v - v_0)$  and sensitivity  $S$  the perturbed signal in counts/sec at wavenumber  $v_0$  can be calculated as

$$\bar{B}_i(v_0) = \bar{B}_{io}(v_0) + \sum_{k=1}^m \left( \frac{\eta_k'}{\eta_k} \right) \bar{X}_{ik} + \sum_{k=1}^m T_k' \bar{Y}_{ik} + \sum_{k=1}^m \left( \frac{\eta_k'}{\eta_k} \right) \bar{Z}_{ik}. \quad (3.42)$$

where

$$\bar{B}_{io}(v) = \sum_{k=1}^m S \int_0^\infty \beta_k I(v - v_0) dv, \quad (3.43)$$

and

$$\bar{X}_{ik}(v_0) = S \int_0^\infty X_{ik} I(v - v_0) dv, \quad (3.44)$$

$$\bar{Y}_{ik}(v_0) = S \int_0^\infty Y_{ik} I(v - v_0) dv, \quad (3.45)$$

$$\bar{Z}_{ik}(v_0) = S \int_0^\infty Z_{ik} I(v - v_0) dv. \quad (3.46)$$

### 3.2.2 Data Analysis

Consider  $\bar{B}_i(v_0)$  as the measured signal at wavenumber  $v_0$  and  $\bar{B}_{io}(v_0)$  as the theoretically estimated signal based upon a guessed volume emission rate profile  $\eta_0$ , a temperature profile  $T_0(z)$ , and an  $O_2$  number density profile  $n_0(z)$ . Eq. (3.42) therefore determines  $\bar{B}_i(v_0) - \bar{B}_{io}(v_0)$ , the deviation of the observed signal from the estimated signal based upon the three guessed profiles.

The  $X, Y$ , and  $Z$  in Eq. (3.42), in general, are referred to as the weighting functions. They



represent the weightings of each parameters from various altitudes, in this case, the  $n'/n_0$ ,  $T$ , and  $\eta'/\eta_0$  respectively, to the difference between the observed and the computed signals. If  $X$  is the largest among the three, the observed deviation is most sensitive to the guessed  $n(z)$  profile, making the  $O_2$  number density the best parameter to be recovered.

There are many techniques that may be used to recover  $\eta(z)$ ,  $T(z)$  and  $n(z)$  from the measurements of  $\bar{B}_i(v)$ . One is the least-square fitting technique, in which iteration is performed to find the best  $\eta(z)$ ,  $T(z)$  and  $n(z)$  profiles that give the minimum deviation  $\bar{B}_i(n_0) - \bar{B}_{i0}(n_0)$  summed over all spectral measurements. Since there are three sets of profiles needed to be recovered, multi-wavelength spectroscopic measurements (at least three spectral region) of the  $O_2$  Atmospheric (0-0) band are required. The data analysis task involved in this technique is very inefficient and requires inversions of matrices in large dimensions. The large number of parameters involved in the fitting process not only makes the iteration convergence difficult, but also produces large errors in the recovered profiles.

Another alternative is to measure temperature and volume emission rate profiles simultaneously with the  $O_2$  Atmospheric (0-0) band emission. This can be accomplished by carrying out spectroscopic measurements of the (0-1) band emission. The volume emission rate of the  $O_2$  Atmospheric (0-1) band is linearly related to that of the (0-0) band with a proportional constant determined by the Franck-Condon factor. Because the (0-1) band emission is optical thin, the measured line-of-sight brightness is a simple Abel integral and its volume emission rate profile can be retrieved efficiently (Hays et al., 1973). In addition, the temperature can also be obtained from the spectroscopic measurements of the rotational structure of the (0-1) emission band.

#### *(0-1) band: Temperature and volume emission rate measurements*

If the (0-1) band emission is measured by a low resolution spectrometer whose instrument width is much wider than the doppler width of the emission line, the observed signal at wavenumber  $v_0$  is

$$\bar{B}(v_0, z_t) = \sum_{j=1}^{\infty} S \int_{z_1}^{\infty} \eta(z) f_j(z) W(z, z_t) I(v_j - v_0) dz, \quad (3.47)$$

where  $v_j$  is the wavenumber of the rotational line  $j$ , and  $I(v_j - v_0)$  and  $S$  are the instrument transmission function and the sensitivity respectively.

Fig. 3.7 shows the computed signals of the O<sub>2</sub> (0-1) band emission using a 12-channel Image Plane Detector Spectrophotometer (IPDS) (Appendix I) for two tangent height measurements: 60 and 80 km. A volume emission rate profile derived from the one for the (0-0) band (Bucholtz et al., 1986) and a continuum scattering background which decreases exponentially with altitude have been assumed. The instrument parameters of the IPD Spectrophotometer listed in Table 3.2 and a field-of-view corresponding to an image of 2km in the vertical and 300 km in the horizontal directions of the Earth's limb are used in the simulation.

**TABLE 3.2**  
**IPD Spectrophotometer Instrument Parameters**  
**Used in O<sub>2</sub> Resonance Fluorescence Simulation**

A <sub>0</sub>	:	45.603 cm <sup>2</sup> (3 inch in diameter)
W	:	1.5 x 10 <sup>-4</sup> ster (~2.0 km x 300 km at the limb)
Tr	:	0.3
Qe	:	4% (at 7620 Å) and 2% at (8650 Å)
I.P.	:	1 second

The volume emission rate at wavenumber  $\nu_0$  and altitude  $z$ ,  $\eta(\nu_0, z)$ , defined as

$$\bar{\eta}(\nu_0, z) = S \sum_{j=1} \eta(z) f_j(z) I(\nu_j - \nu_0), \quad (3.48)$$

can then be obtained by using the Abel inversion algorithm (Hays et al., 1973). After measurements at all the wavenumbers have been inverted, we can get the spectral information or the rotational band structure of the (0-1) band emission rate.

Fig. 3.8 gives the volume emission rates recovered at the 12 spectral regions of the IPDS at 60 and 80 km altitudes, revealing clearly the rotational emission band structures. By using a nonlinear least-square fitting method (Killeen and Hays, 1984; Appendix I), one can then obtain the total band volume emission rate and the rotational temperature of the O<sub>2</sub>(b<sup>1</sup>Σ<sub>g</sub><sup>+</sup>) molecules. In order to conserve computation, we first linearize the problem by expanding Eq. (3.48) about a set of approximations or initial guesses ( $\eta$ ,  $T$ ,  $\eta_c$ ) and keep only the first-order terms in the expansions:

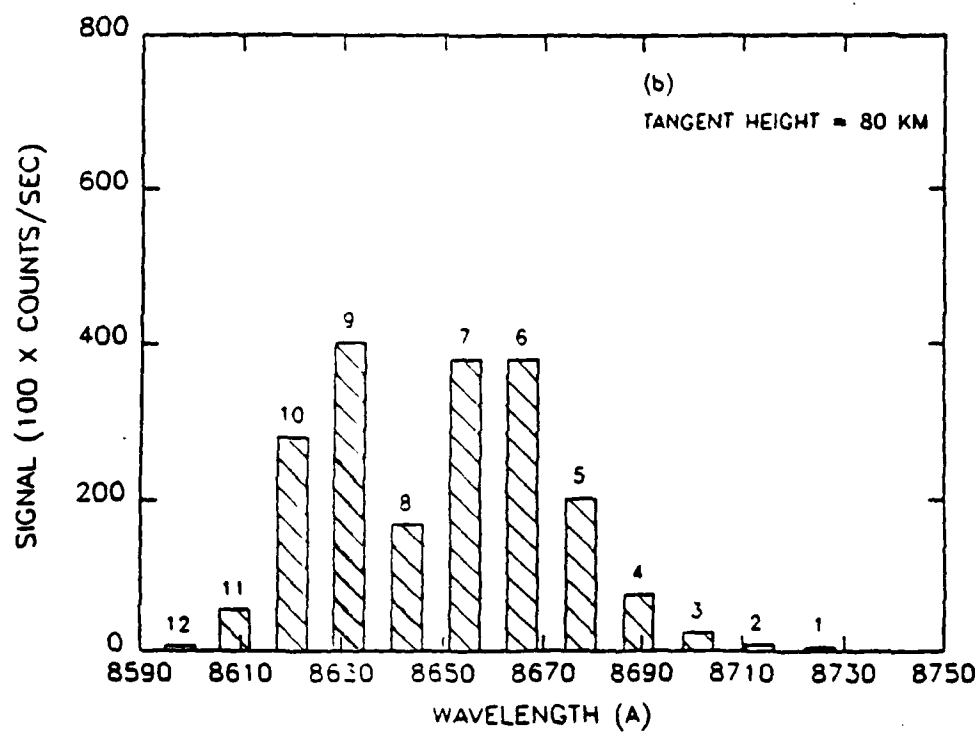
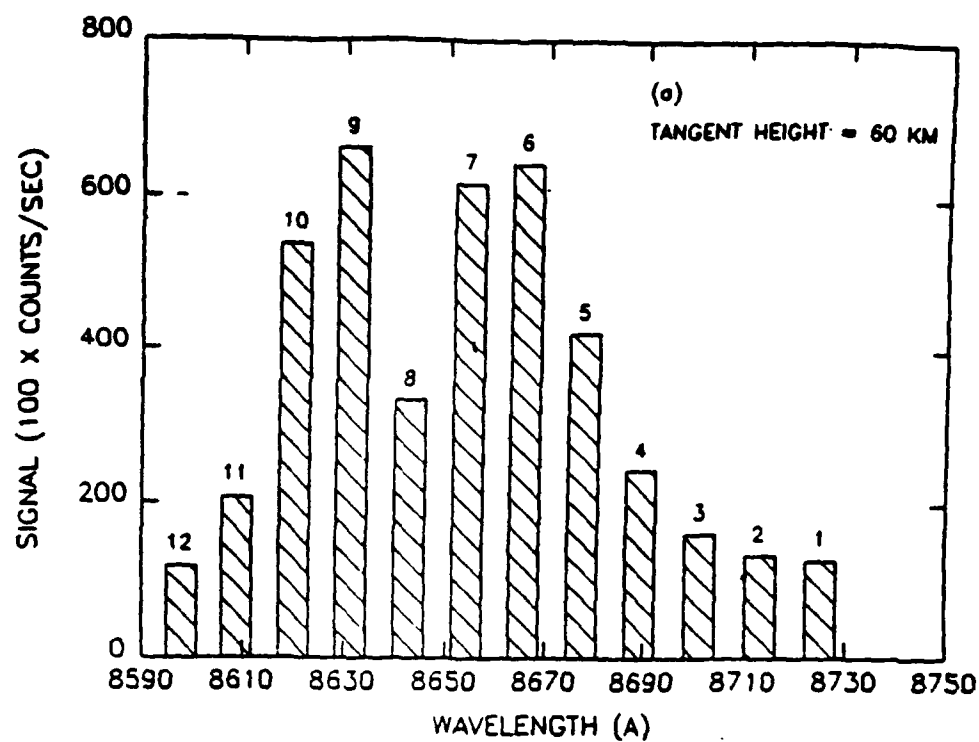


Figure 3.7

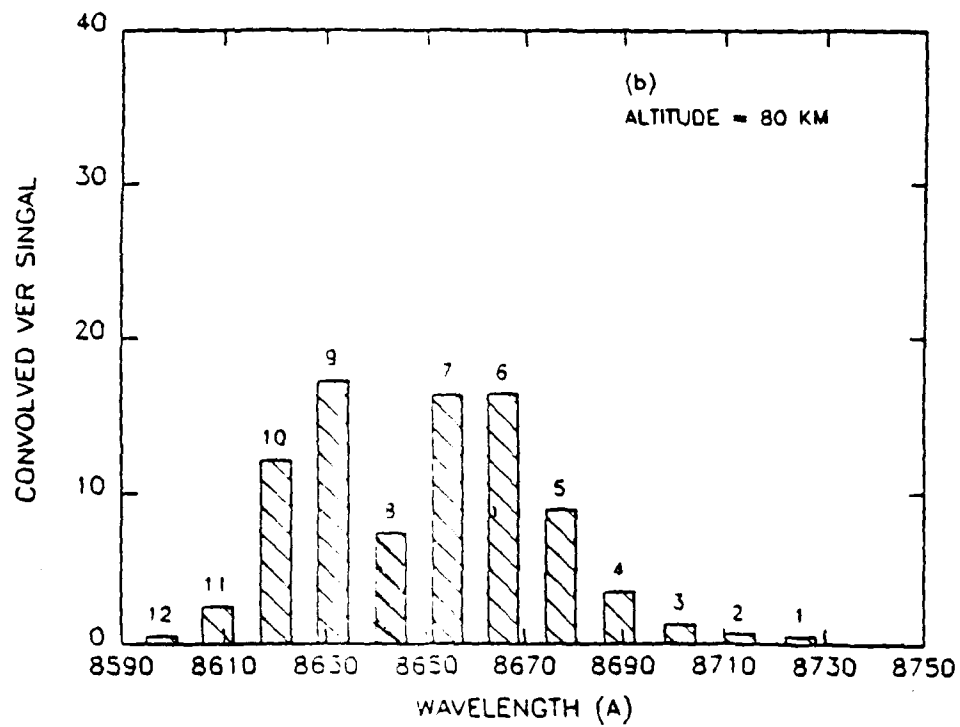
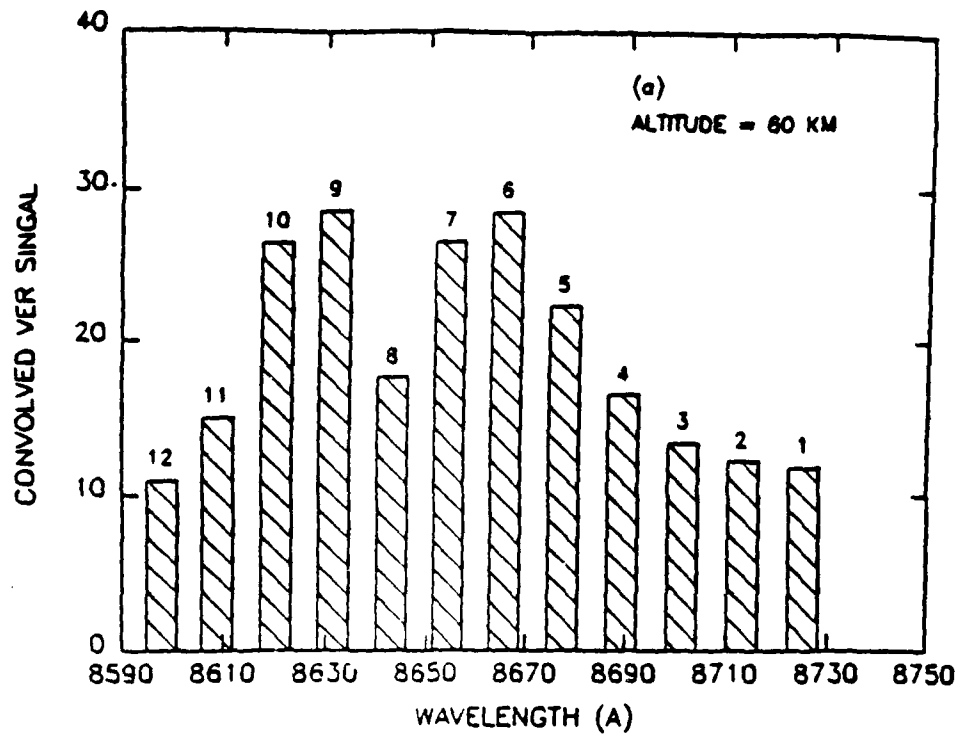


Figure 3.8

$$\bar{\eta}_{kn}(\eta_k, T_k, \eta_{ck}) \equiv \bar{\eta}_{kn}(\eta'_{ko}, T'_{ko}, \eta'_{ck}) + \frac{\partial \bar{\eta}_{kn}}{\partial \eta_k} (\eta_k - \eta'_{ko}) + \frac{\partial \bar{\eta}_{kn}}{\partial T_k} (T_k - T'_{ko}) + \frac{\partial \bar{\eta}_{kn}}{\partial \eta_{ck}} (\eta_{ck} - \eta'_{ck}) \quad (3.49)$$

where  $\eta_{kn}$  is the (0-1) band volume emission rate, at wavenumber channel  $n$  and  $\eta_{ck}$  is the continuum scattering rate at altitude  $k$  respectively.

If the measured volume emission rate at the  $n$ -th channel obtained from Eq. (3.49) is expressed by  $C_{kn}$ , the sum of the square of the residuals between the theoretically computed signal and the measured signal  $C_{kn}$  is calculated by

$$\langle \delta_k^2 \rangle = \sum_{n=1}^{12} (C_{kn} - \bar{\eta}_{kn})^2 \quad (3.50)$$

By minimizing  $\langle \delta_k^2 \rangle$ , one can obtain a set of better estimated  $\eta_k, T_k$  and  $\eta_{ck}$ , or  $P_k^l$  ( $l=1,2,3$  for  $\eta, T, \eta_c$  respectively), a general representation of the newly determined parameters from a single matrix multiplication operation:

$$P_k^l = \sum_{m=1}^3 M_{km}^l N_{km}, \quad (3.51)$$

where  $M_{kc}^1$  is an inverse matrix of  $L_{km}^1$ ,

$$L_{km}^1 = \sum_{n=1}^{12} \frac{\partial \bar{\eta}_{kn}}{\partial P_k^1} \frac{\partial \bar{\eta}_{kn}}{\partial P_k^m}, \quad (3.52)$$

and

$$N_{km} = \sum_{n=1}^{12} \left( \bar{\eta}_{kn} - C_{kn} - \sum_{l=1}^3 \frac{\partial \bar{\eta}_{kn}}{\partial P_k^l} P_k^l \right) \frac{\partial \bar{\eta}_{kn}}{\partial P_k^1}. \quad (3.53)$$

Iterations are performed in order to obtain convergence of the results. The speed of convergence depends upon the proximity of the initial guessed values to the actual values.

### (0-0) Atmospheric band: Density Measurement

After the (0-1) band volume emission rate and the atmospheric temperature profiles are determined, we can calculate from Eq. (3.42),  $\bar{B}_i(v_o) - \bar{B}_{io}(v_o)$ , the deviation of the observed signal at tangent height  $i$  and wavenumber  $v_o$  for the (0-0) band emission from the estimated signal based upon a guessed  $O_2$  number density profile  $n_o(z)$ ,

$$\bar{B}'_i(v_o) = \bar{B}_i(v_o) - \bar{B}_{io}(v_o) = \sum_{k=1}^m \left( \frac{n'_k}{n_k} \right) \bar{X}_{ik}. \quad (3.54)$$

We can solve the above linear equation for  $n'(z)$  to get a better estimate of  $n(z)$ ,  $n(z) = n_o(z) + n'(z)$  by minimizing the square of the deviation of  $\bar{B}_i(v_o) - \bar{B}_{io}(v_o)$  summing over all spectral and tangent heights. The  $n(z)$  profile is then used as a new guess to Eq.(3.54), and the process is repeated until  $n'(z)$  becomes very small compared to  $n_o(z)$ . This technique is identical to the one used for the (0-1) band data analysis and gives one best  $O_2$  number density profile based upon the measurements at all of the tangent heights and the spectral regions.

Because the  $O_2$  number density information can only be recovered if there is significant degree of extinction in the measured intensity of the  $O_2$  Atmospheric (0-0) band emission, the capability of this technique is therefore limited by the magnitude of the absorption cross-section. In other words, the  $O_2$  number density profile can only be directly measured up to an altitude of approximately 90 km. Since the temperature profile is obtained in the whole region between 60 and 120 km, the  $O_2$  density from 90 km to 100 km at the turbopause can be derived from the barostatic equation (Banks and Kockarts, 1973),

$$n(z) = n_o(z) \left[ \frac{T(z_o)}{T(z)} \right] \exp \left\{ - \int_{z_o}^z \frac{mg}{kT} dz \right\} \quad (3.55)$$

under perfect mixing condition, and above 100 km,

$$n(z) = n_o(z) \left[ \frac{T(z_o)}{T(z)} \right] \exp \left\{ - \int_{z_o}^z \frac{m_{O_2}g}{kT} dz \right\} \quad (3.56)$$

under diffusive equilibrium condition, where  $m$  and  $m_{O_2}$  are the mean molecular weights of the atmosphere and  $O_2$  respectively.

Fig. 3.9 shows the simulated signals that the IPDS measures for a one second integration time at a tangent height of 60 km. The unattenuated signals, derived from the (0-1) volume emission rate profile, are also shown. Although it is not a practical approach, we can still, in principle, recover the  $n(z)$  profile directly from Eq. (3.54) using measurements from a single channel. However, because the optical depth differs for each channel, the accuracy in the recovered density profile is different.

### 3.3 Statistical Accuracy Analysis

As indicated in Fig. (3.9), the difference in the observed and computed signal,  $\bar{B}_i - \bar{B}_{i0}$ , depends upon not only the  $O_2$  number density profile  $n/n_0$ , but also the temperature  $T$  and the volume emission rate profiles  $\eta/\eta_0$ . The uncertainties in the temperature and the volume emission rate determined from the (0-1) band emission would give rise to error in the recovered  $O_2$  number density.

#### *Statistical Errors in Temperature and Volume Emission rate*

The statistical errors  $\Delta P_k^1$  in the volume emission rate ( $P_k^1$ ) temperature ( $P_k^2$ ) and obtained from the (0-1) band measurements can be estimated from Eq. (3.51) using theory of error propagation,

$$(\Delta P_k^1)^2 = \sum_{n=1}^{12} \left\{ \sum_{m=1}^3 M_{km}^1 \left( \frac{\partial \bar{\eta}_{kn}}{\partial P_k^n} \right)^2 \right\} (\Delta C_{kn})^2, \quad (3.57)$$

where  $\Delta C_{kn} = C_{kn}^{1/2}$ , assuming that measured signal  $C_{kn}$  has a Poisson random noise. Fig. 3.10 presents the statistical accuracies in the temperature and total (0-1) band volume emission rate profiles obtained based upon the simulated measurements given in Fig. 3.8.

#### *Statistical Errors in $O_2$ number density*

The capability of recovering  $O_2$  number density profile from the (0-0) band emission depends upon the relative magnitude of its weighting function (X) in Eq. (3.42) compared to the ones of temperature (Y) and the volume emission rate (Z). For example, consider a case when the weighting function for the volume emission rate  $\eta/\eta_0$  is the largest among the three. A small error in the profile of  $\eta(z)$  would produce a large error in the computed signal  $\bar{B}_{i0}$ , which in turn is propagated to the recovered  $O_2$  number density profile.

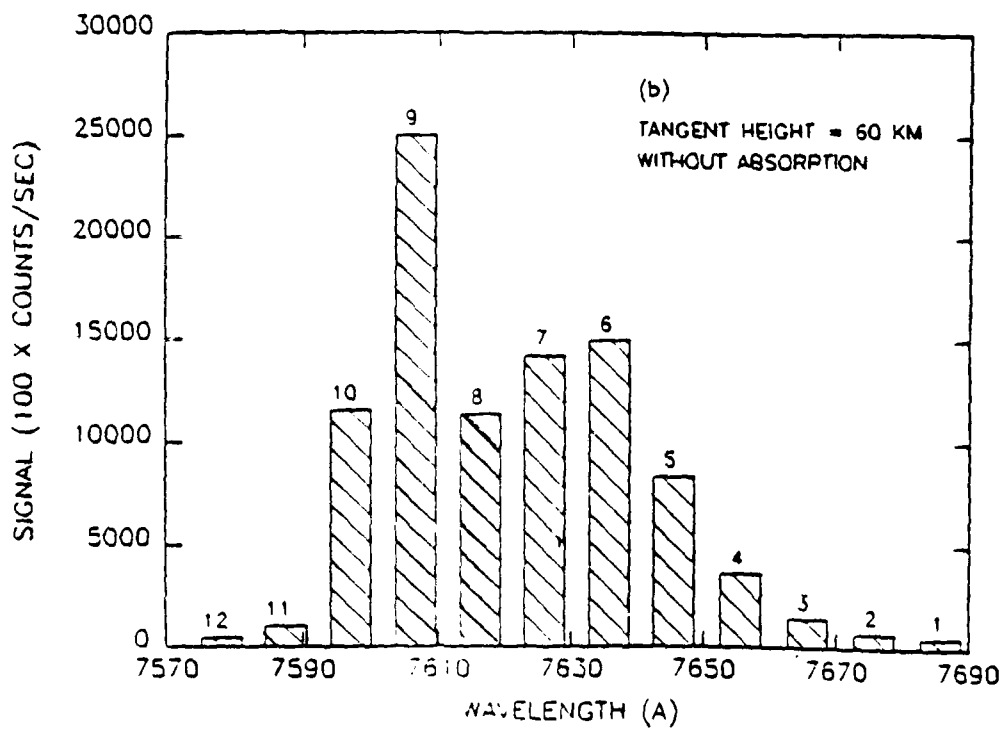
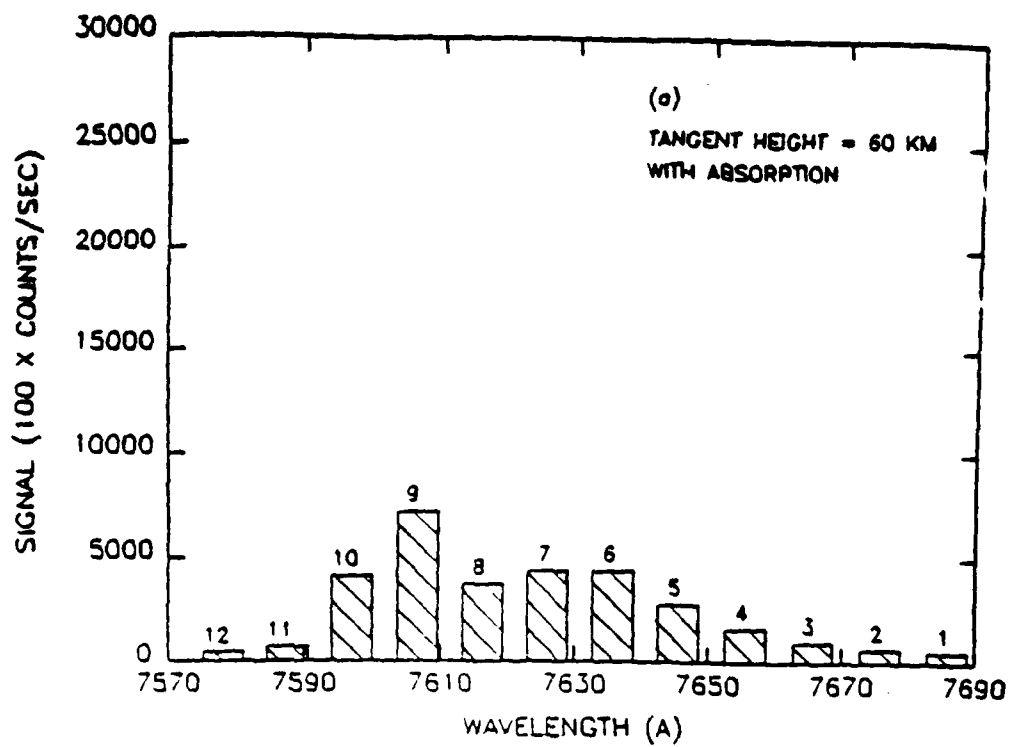


Figure 3.9



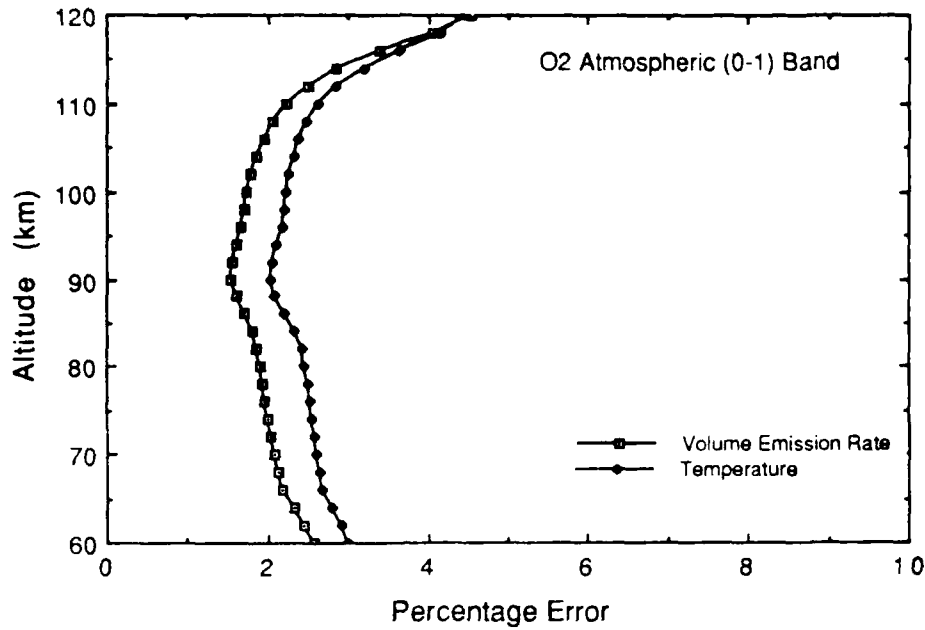


Figure 3.10

Fig. 3.11 shows the weighting functions  $X$ ,  $Y$ , and  $Z$  as a function of altitude for measurements at 60 km tangent height for both a weak (channel 3) and a strong (channel 9, absorption case respectively. The maximum weighting functions, especially for the weak absorption case, are found at the tangent altitude, resulting directly from the geometric enhancement effect. For the stronger absorption case, most of the emission originating from the tangent altitude region is absorbed and cannot be observed. As a result, the altitude that the  $O_2$  number density can be recovered is higher and the weighting function near the tangent altitude are reduced.

Expressing  $n'/n_0$  in terms of  $B'$ ,  $T'$ , and  $\eta'/\eta_0$ ,

$$\frac{n'_k}{n_k} = \sum_{i=1}^m \bar{X}_{ik}^{-1} \bar{B}_i - \sum_{k=1}^m \left( \sum_{i=1}^m \bar{X}_{ik}^{-1} \bar{Y}_{ik} \right) T'_k - \sum_{k=1}^m \left( \sum_{i=1}^m \bar{X}_{ik}^{-1} \bar{Z}_{ik} \right) \left( \frac{\eta'_k}{\eta_k} \right), \quad (3.58)$$

we can estimate the error in the recovered  $n'/n_0$  using theory of error propagation,

$$\Delta \left( \frac{n'_k}{n_k} \right)^2 = \sum_{i=1}^m (\bar{X}_{ik}^{-1})^2 (\Delta B_i)^2 + \sum_{k=1}^m \left( \sum_{i=1}^m \bar{X}_{ik}^{-1} \bar{Y}_{ik} \right)^2 (\Delta T'_k)^2 + \sum_{k=1}^m \left( \sum_{i=1}^m \bar{X}_{ik}^{-1} \bar{Z}_{ik} \right)^2 \Delta \left( \frac{\eta'_k}{\eta_k} \right)^2 \quad (3.59)$$

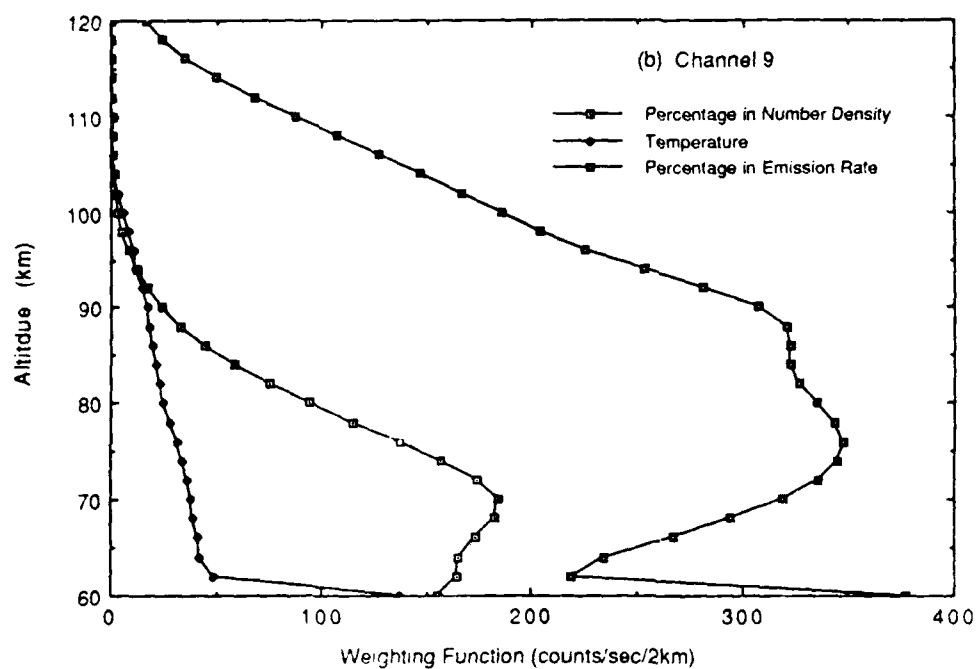
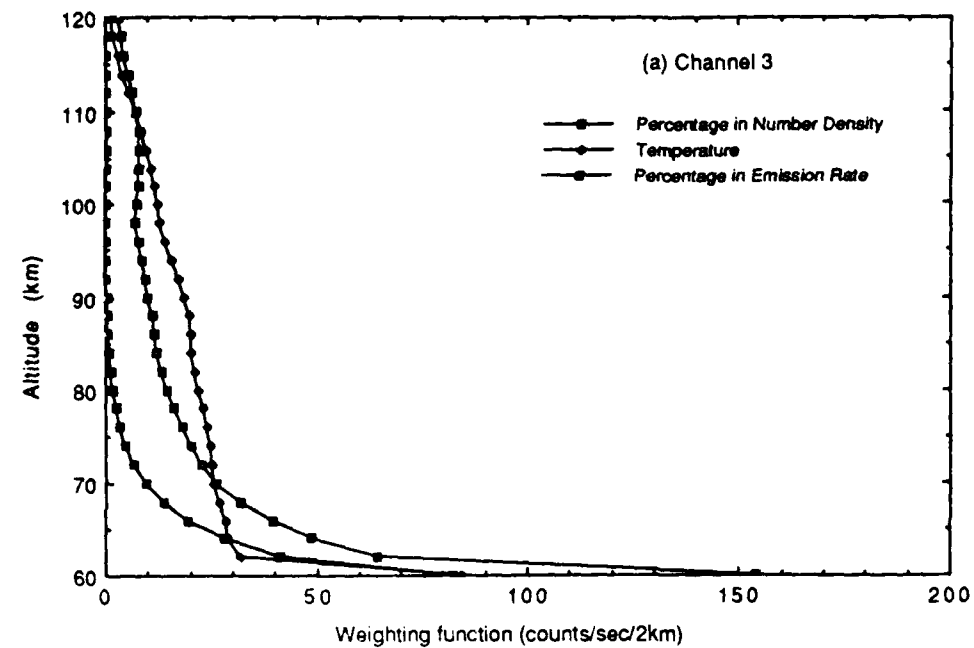


Figure 3.11

where  $\Delta B_i$  is the error in the measured signal,  $\Delta(n_k'/n_k)$ ,  $\Delta(\eta_k'/\eta_k)$  are the relative error in the  $O_2$  number density and the (0-0) band volume emission rate, and  $\Delta T_k'$  is the error in the temperature respectively.

Fig. 3.12 shows the accuracies of the retrieved  $O_2$  number density profile based on the (0-0) band 12-channel IPDS intensity signals shown in Fig. 3.9a. The accuracies of the temperature and volume emission rate profiles recovered from the (0-1) band measurements have been included. The measured signals at channel 12 ( $\sim 7570\text{\AA}$ ) have been used as the contribution of the scattering continuum background. Among the other eleven spectral regions measured, four are able to provide the  $O_2$  number density profile with an accuracy less than 10% below 90 km. Because both the emission signals and the self-absorption cross-sections are small in the spectral regions near the bandhead (channel 11) and the bandtail (channel 1), the accuracies in the recovered  $O_2$  number density are very poor. As the altitude increases above 90 km, the self-absorption process becomes less important, resulting in a rapid deterioration in the quality of the recovered  $O_2$  number density profile.

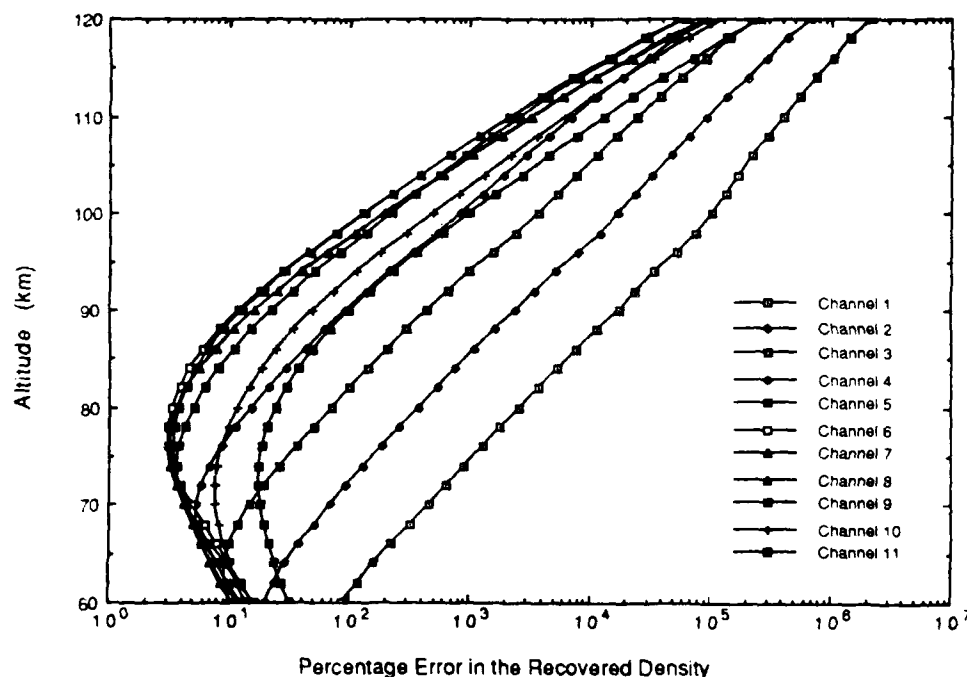


Figure 3.12

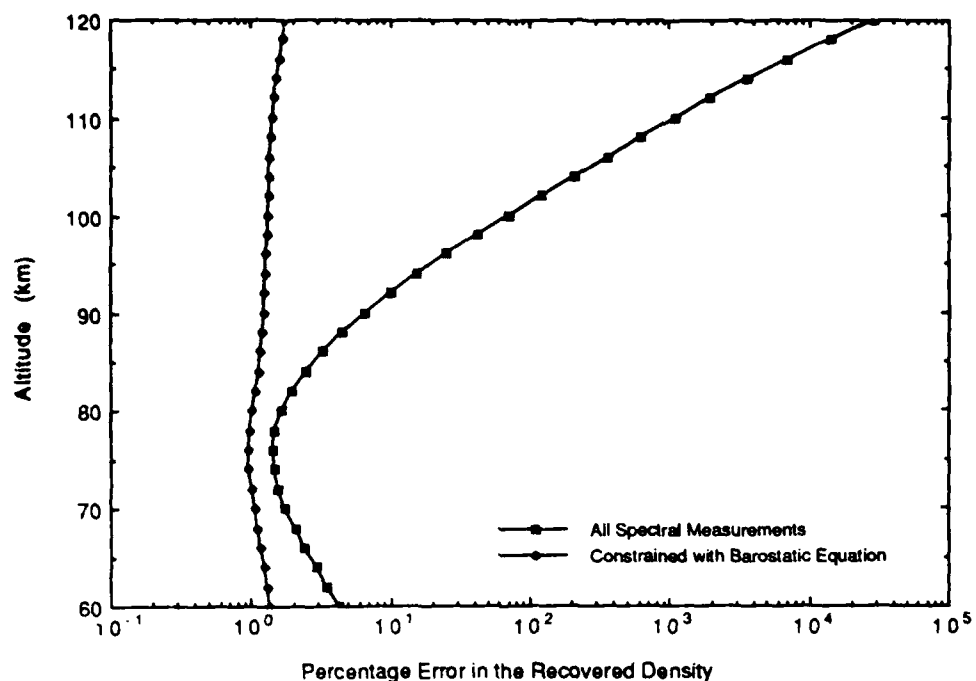


Figure 3.13

Fig. 3.13 presents the accuracy of the recovered  $O_2$  number density profile when the measurements from all the eleven channels are combined. It demonstrates that using a low resolution spectrometer, such as the IPDS used here, one can retrieve  $O_2$  number density profile below 90 km with an accuracy of less than 5% for one second integration time at each tangent height. If we use the barostatic equation to constrain the density profile to follow the temperature profile, the accuracy is improved, especially in the region above 90 km where the accuracy from the direct measurements is poor.

### 3.4. Summary and Discussion

A technique used to determine the atmospheric temperature and density profiles in the critical 60 to 120 km region from the  $O_2$  (0-0) and (0-1) Atmospheric band emissions is presented. The technique requires spectroscopic measurements of the (0-1) band emission to obtain the volume emission rate profile of the Atmospheric band and the atmospheric temperature profile. The (0-1) band emission is optically thin, and it relates to the (0-0) band emission by the Franck-Condon factor. The  $O_2$  number density profile is then obtained from the amount of self-absorption

determined from the measured (0-0) band emission brightness and the unabsorbed emission brightness computed from the (0-1) volume emission rate profile.

Here we have discussed a technique which is based upon daytime measurements of the O<sub>2</sub> Atmospheric band emissions. In principle, this technique should also apply to nighttime measurements, although the emission intensities are much weaker, approximately 1/20 of the intensities in the daytime. The O<sub>2</sub> Atmospheric bands at night are produced by the chemical source mainly and have a emission layer peaked at approximately 95 km. Using the data analysis technique discussed in the text, the temperature, O<sub>2</sub> density and the volume emission rate profiles can only be obtained in a region between 80 and 110 km. The O<sub>2</sub> density below 80 km therefore could only be obtained using the least-square fitting techniques to get the temperature and O<sub>2</sub> density profile simultaneously from the amount of self-absorptions.

Measurements at low tangent heights also include the scattered sunlight due to Rayleigh and aerosol scattering processes. The contribution due to these two processes are highly variable, depending upon the atmospheric and aerosol density profiles, the scattering angle, and the effective surface albedo. Among the factors which affect the continuum brightness, the scattering angle is the only one that we can control during measurement sequences. The scattered light, in general, is distributed equally in the forward and backward directions for the Rayleigh scattering process and concentrated mostly in the forward direction for the aerosol scattering process. In order to minimize the impact of the scattered sunlight on the accuracies of our measurements, the instrument should have a line-of-sight which points at 90 degree away from the Sun, or has a solar azimuthal angle of 90 degree. The continuum brightnesses included in our study here are obtained using a single scattering model developed at the University of Michigan's Space Physics Research Laboratory. A solar azimuthal angle of 90 degree is assumed.

We use a low resolution 12-channel IPD Spectrophotometer described in Appendix I to simulate the measurements of the O<sub>2</sub> Atmospheric band emissions from space. We demonstrate in this report that for one second integration time in each tangent height measurement, one can recover the temperature and the O<sub>2</sub> number density profiles with statistical accuracies of less than 2% at a vertical and horizontal resolution of 2 km and 300 km respectively. Because the quantum efficiencies of the IPD are small at the spectral regions near 7600 and 8600Å, a 3.0-inch diameter telescope is adopted in order to achieve the required signal levels. As the ring-type Charge-Coupled Device (CCD) detector becomes available, the quantum efficiency can be increased by at least a factor of 10. The size of the telescope in this case can either be reduced or be maintained to further improve the accuracies of the recovered density and temperature. Most important of all,

this would make the nighttime measurements of the temperature and density profiles more accurate.

The (0-1) band emission was used in our example to determine the atmospheric temperature profile between 60 and 120 km. Its emission brightness, however, becomes weaker as the tangent height increases above 100 km, resulting in a rapid deterioration in the accuracy of the recovered temperature profile (Fig. 3.7). In order to improve the accuracy, one can replace the (0-1) band emission by the stronger (0-0) emission which is optically thin above 100 km.

The  $O_2(b^1\Sigma_g^+)$  excited molecules are produced mainly by the energy transfer of  $O(^1D)$  atoms with  $O_2$  at altitudes above 100 km, following the photodissociation of  $O_2$  by the absorption in the Schumann-Runge continuum. By knowing the temperature and the  $O_2$  number density profiles in the region, one can quantitatively examine the role which this important photodissociation process plays in the Earth's energy budget.

#### 4. RAYLEIGH SCATTERING TECHNIQUE

The radiation that emerges from a planetary atmosphere is determined by a number of factors which depend on the character of the atmosphere, the nature of the planetary surface, and the solar spectrum. The atmospheric particles responsible for scattering cover a range of sizes from gas molecules ( $\sim 10^{-8}$  cm) to large raindrops and hail particles ( $\sim$  cm). The relative intensity of the scattering light depends strongly on the ratio of the particle size to the wavelength of the incident radiation. When this ratio is small, the scattered light is distributed equally into the forward and backward direction (Rayleigh scattering). When the particles are large, an increasing portion of the light is concentrated in the forward direction. In this case (Mie scattering), the distribution of scattering light intensity with scattering angle becomes very complex.

The major gases of the atmosphere scatter light due to the processes of Rayleigh scattering. In this case, the scattering coefficient is inversely proportional to the fourth power of the wavelength of the incident radiation. During the daytime period the blue sky results from this preferential scattering at shorter wavelengths. If the absorption processes are not important, the intensity of the scattering light contains the information of the number density of the atmospheric gases. Thus Rayleigh scattering can be used to determine the density of the atmosphere at high altitudes. This method of observation is illustrated in Fig 4.1 and have been used on the Solar Mesosphere Explorer Satellite to determine the density and temperature in the upper stratosphere (Rusch, et al., 1983).

However, questions regarding this method of measuring the density arise due to the presence of aerosols and Polar Mesospheric Clouds (Thomas and McKay, 1985). Rayleigh theory of scattering cannot be applied to these particles, because the size of the aerosols are of the same order of magnitude or larger than the wavelength of the incident light. The basic theory for the study of scattering light by aerosols was presented by Mie (1908). This theory generally assumes an ensemble of identical spherical particles and requires considerable computing resources for its solution. Simplified formula have often been used (Van de Hulst, 1957).

The capability of measuring the density of the atmospheric gases using Rayleigh scattering technique depends upon the relative magnitude of the aerosol scattering, since it causes scattering that is difficult to distinguish from density variations in the basic atmosphere. We will address this issue in the next section.

## Rayleigh Scattering

(1) Rayleigh Scattering:  $n(N_2), n(O_2), \alpha(\theta, \lambda), \alpha_s(\text{Albedo})$

(2) Aerosol Scattering:  $n(\text{Aerosol}), \sigma_{\text{Aerosol}}(\theta, \lambda), \alpha_s(\text{Albedo})$

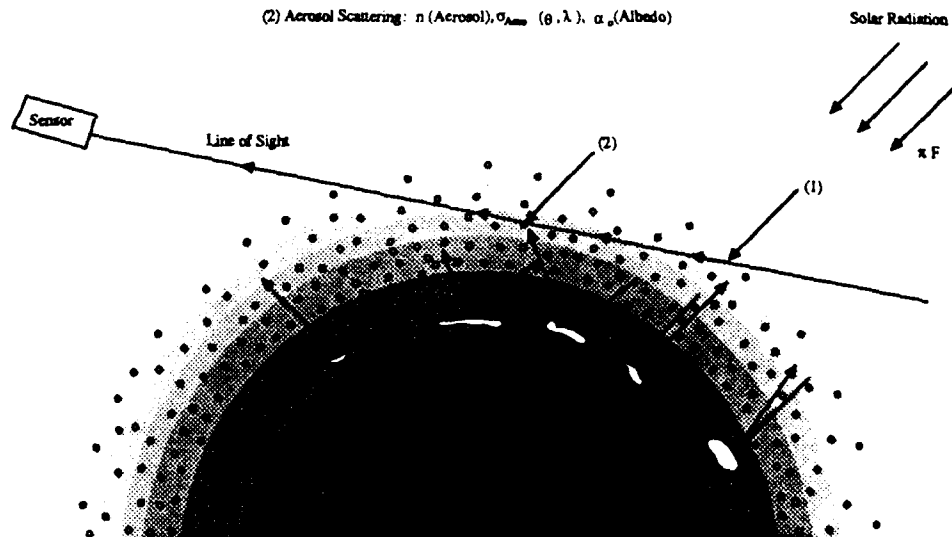


Figure 4.1

Another question regarding this technique arises due to the variability of the Earth's surface albedo. As illustrated in Fig. 4.1, the atmospheric particles along the line-of-sight scatter light which comes from two distinct sources. One comes directly from the sun and in this case, the emission rate is only a function of the solar flux, number density of the scattering volume, and the scattering phase angle. The other comes from the indirect solar radiation which is reflected by the Earth's surface. The relative importance of this source depends on the surface albedo and the tangent ray height of the measurement. As the surface albedo varies, the observed line-of-sight intensity changes. As a result, this technique might interpret this perturbation as density variations in the atmosphere.

In this report, we simulate the Rayleigh and aerosol scattering in the 50-120 km altitude region using a single scattering program generated here at the University of Michigan's Space Physics Research Laboratory. This single scattering model assumes that an incoming photon is scattered at most once by atmospheric major gases (Rayleigh) and aerosols (Mie). The effect of multiple scattering by underlying layers and reflection at the surface are simulated by numerous effective albedos. We will show how we can resolve the problem due to the existence of aerosol by using a multiplicity of wavelengths. We will also demonstrate the difficulty caused by the uncertainty in the surface albedo.



## 4.1 Scattering Intensity Simulation

### *Effect of Aerosols*

Fig. 4.2 shows the calculated scattering brightness as a function of tangent height due to Rayleigh only, aerosol only, and Rayleigh plus aerosol scattering for wavelengths at 4000Å, 5000Å, 6000Å and 8000Å respectively. The results shown here are simulated for a spacecraft located at an altitude of 450 km, solar zenith angle of 45 degree and a surface albedo of 0.2.

The presence of aerosols in the mesosphere significantly affects the scattered brightness as a function of wavelength. In general Rayleigh scattering takes place more efficiently at shorter wavelength, varying with  $1/\lambda^4$ . The aerosol scattering, however, goes as  $1/\lambda^n$ , where  $n < 4$ , and increases in importance at longer wavelength. This is readily apparent in Fig. 4.2. At 4000Å, the contribution to the brightness profile by aerosol scattering is an order of magnitude less than the contribution by Rayleigh scattering. The measured intensities in this short wavelength spectral region are therefore mostly produced by the Rayleigh scattering processes and are best suited for the determination of atmospheric densities.

For our calculations we have used an aerosol density profile contained in the LOWTRAN 5 model. The LOWTRAN 5 model allows the specification of aerosol levels (i.e. background, low, moderate and high volcanic activity, etc.) in the lower stratosphere and above which it allows the aerosol density profile to drop off exponentially with height. The question arises as how well we know the aerosol concentration in the atmosphere.

Few observations and studies of mesospheric aerosol concentrations and distributions have been made since a spate of observations in the early 1970's. Lidar shows promise as a technique capable of routine measurements of mesospheric aerosol density. Radiance measurements from the SME satellite are a potential database for mesospheric aerosol studies. Aerosol layers from volcanic and unidentified sources in the middle stratosphere have been readily observed by the SME satellite (Clancy, 1986). A significant enhancement in aerosol scattering over Rayleigh scattering occurred after the eruption of EL Chichon in 1982 (Naudet and Thomas, 1987). A preliminary SME data analysis indicates that for equatorial regions an enhancement in brightness of 10-15% is due to mesospheric aerosols, and that, if concentrations of aerosols exists in the mesosphere at midlatitudes, the aerosols are well-mixed. Clouds in the summer polar mesosphere display an enhancement in brightness in SME data that is one or two orders magnitude greater than the brightness due to Rayleigh or aerosol scattering (Thomas and McKay, 1986).

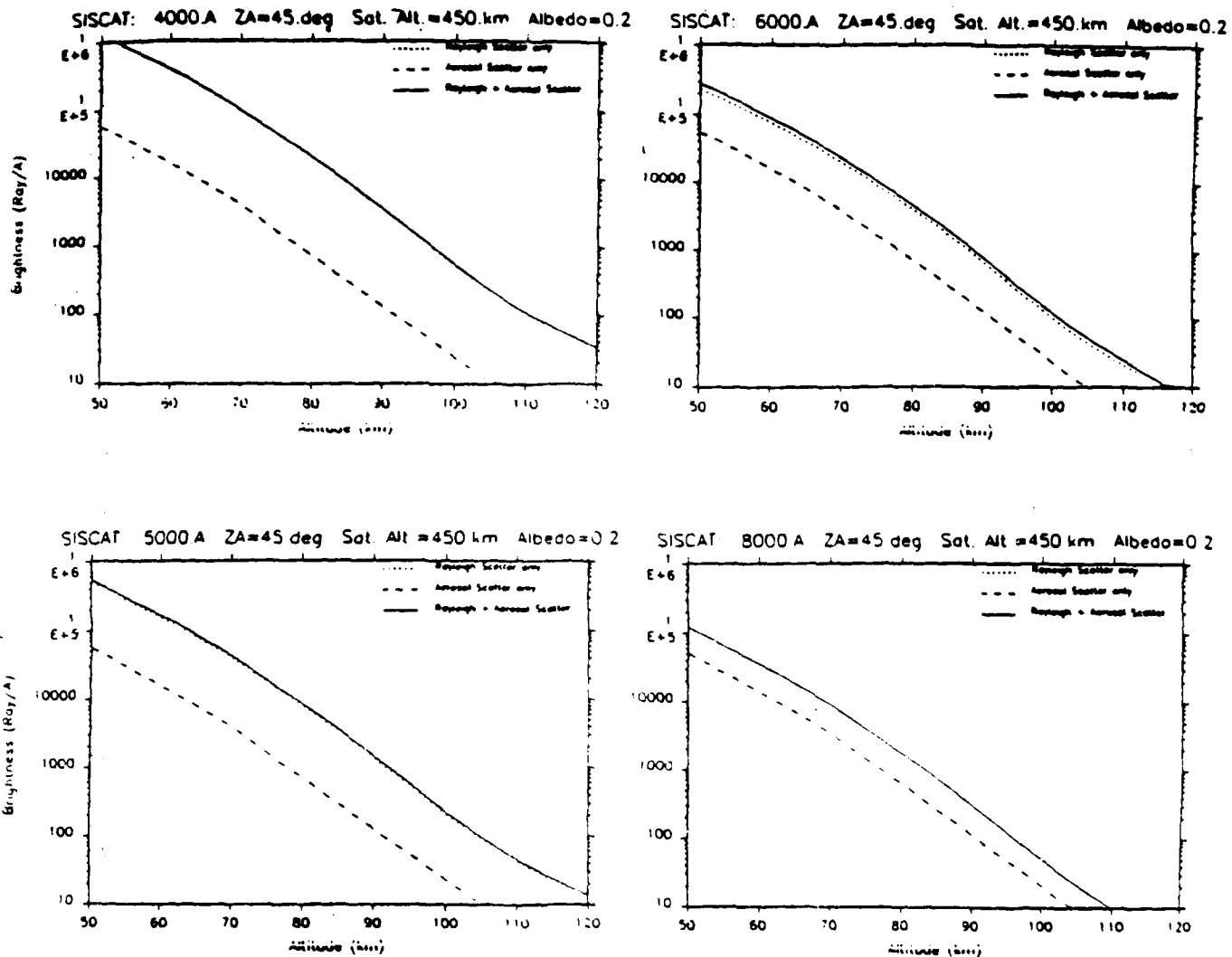


Figure 4.2

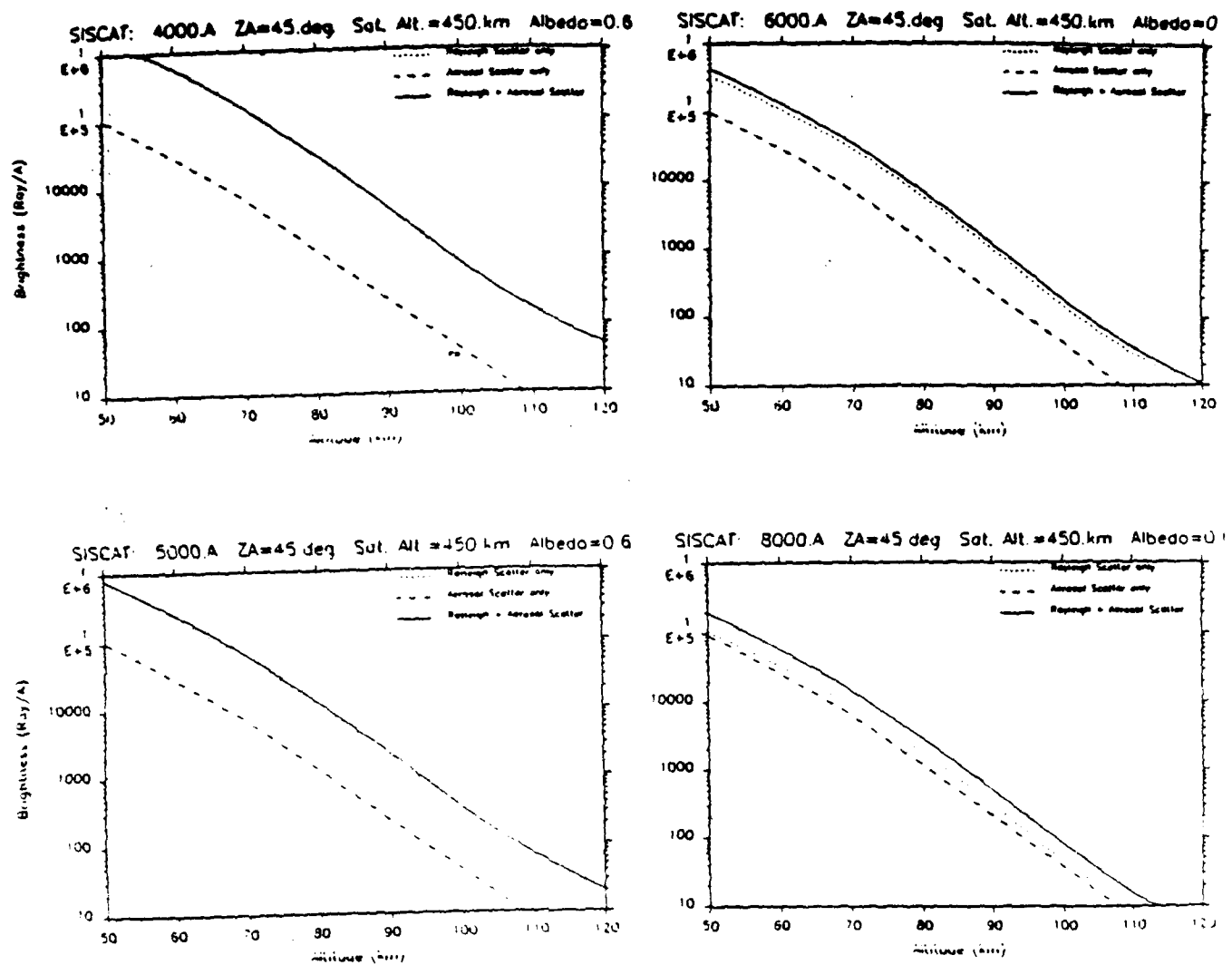


Figure 4.3

While a climatology and height distribution of mesospheric aerosols is not presently available, observations suggest that aerosols are a minor constituent in the mesosphere. Although the presence of a larger than expected concentrations of aerosols in the mesosphere would significantly and negatively impact on the Rayleigh scattering measurement technique of atmospheric density, the judicious selection of wavelength and strategy can still minimize the effects of aerosols.

#### *Surface Albedo Effect*

Fig. 4.3 shows the same results for Fig. 4.2 except that the surface albedo is increased to 0.6. As the surface albedo increases, the contribution to the scattered brightness from the ground reflection also increases. For example, a brightness of  $4.2 \times 10^5$  Rayleigh/Å at  $4000\text{Å}$  is obtained for a measurement at 60 km tangent height and an effective surface albedo of 0.2. As the surface albedo is increased to 0.6 while keeping the atmospheric condition and the observational geometry the same, an increase of approximately 50% to  $6.0 \times 10^5$  Rayleigh/Å in the scattered brightness is obtained. For measurements at 120 km tangent height this brightness also changes from  $3.3 \times 10^1$  to  $4.9 \times 10^1$  Rayleigh/Å. The effective surface albedo is highly variable due to the types of surface (continent or ocean, forest or ice covered, etc) and the amount of cloud coverage. The atmospheric density profile determined from the scattered intensity therefore is very uncertain.

#### **4.2 Summary and Discussion**

The Rayleigh scattering technique does not appear to be a viable remote sensing technique for the determination of atmospheric density. This is due to the lack of distinct differentiation between the contribution to the observed brightness from the Rayleigh scattering and the contributions from the aerosol scattering and ground reflection.

## 5. MERIT EVALUATION

Three techniques which have the potential to measure the atmospheric density in the altitude region between 60 and 120 km have been examined. Each of these techniques has inherent advantages as well as weakness. In this section we compare the relative merits of these related techniques.

### 5.1 Feasibility

#### *Rayleigh Scattering Technique*

- not feasible
  - due to its lack of distinct differentiation between the contribution to the observed brightness from the Rayleigh scattering and the contributions from the aerosol scattering and ground reflection,
  - An uncertainty in the knowledge of the effective ground albedo will produce errors beyond our requirements in the recovered atmospheric density profile.

#### *Stellar occultation and Resonance fluorescence of O<sub>2</sub> Techniques*

- are feasible
  - both techniques use classical theory of photoabsorption spectroscopy,
  - in addition to the atmospheric density profile, both techniques can recover the temperature profile since the absorption cross-sections used in both techniques are temperature dependent.

### 5.2 Accuracy

#### 5.2.1 Statistical Error

#### *Stellar Occultation Technique*

- varies depending upon the data analysis techniques and the instrument sensitivity,

- varies from one profile to another due to the changes of star brightness,
- cannot be improved by the integration time,
  - the integration time is fixed by the orbital velocity and the star location.
- can be improved by using barostatic equation since the temperature profile is also obtained.

#### *Resonance Fluorescence of O<sub>2</sub> Technique*

- also varies depending upon the data analysis techniques and the instrument sensitivity,
- is similar from one profile to another due to a steady emission brightness,
- can be improved by the integration time,
  - for example, the emission is weaker at higher altitudes, the accuracies in the recovered density and temperature can be improved by increasing the integration time.
- can also be improved by using barostatic equation.

#### 5.2.2. Systematic Error

##### *Stellar Occultation Technique*

- arises due to the uncertainty in the absorption cross-sections,
  - 4 percent and somewhat greater for  $\sigma < 5.0 \times 10^{-22} \text{ cm}^2$  (Yoshino et al., 1987),
- arises due to the uncertainty in the absorption line widths,
  - negligible considering the few percent error in the measured widths (Yoshino, 1988, private communication)
- arises due to the uncertainty in the line positions,
  - negligible considering the 0.0013 nm accuracy in the measured line positions (Cheung et al., 1986b)
- arises due to the uncertainty in the temperature dependency of the cross-sections.
  - negligible since the energies of both the upper and lower states are accurately known.

##### *Resonance Fluorescence of O<sub>2</sub> Technique*

- arises due to the uncertainty in the emission and absorption line strengths,
  - ~10 percent and varies from line to line (AFGL line compilation of McClatchey et al., 1973),
  - can be improved by using more accurately measured line strengths (photo-acoustic spectroscopy technique by Paul B. Hays at SPRL, the University of Michigan, 1988)

- arises due to the uncertainty in the Franck-Condon Factor (ratio between the transition probabilities of the O<sub>2</sub> Atmospheric (0-0) band and (0-1) band),
  - may be few tens of percent if calculated Franck-Condon factors of Nicholls (1965) are used,
  - can be improved if more accurate value determined from this resonance fluorescence experiment is used,
- arises due to the uncertainty of the line positions
  - negligible considering the accuracy in our knowledge of the line positions,
- arises when the temperature dependency on the cross-sections is considered,
  - negligible since the energies of both the upper and lower states are accurately known.

### 5.2.3. Pointing and Satellite Position Error

- arises due to the uncertainty in the tangent height determination,
  - can be improved by having accurate pointing and satellite tracking

## 5.3 Complexity

### 5.3.1 Operation

#### *Stellar Occultation Technique*

- requires accurate knowledge of the satellite position all the time as planning aids,
- requires accurate pointing in locating the star as the source of light,
- requires an on-board computer and an efficient algorithm to locate the best available star for the next occultation sequence for autonomous operation,
- involves frequent azimuthal and zenith movements of the telescope.

#### *Resonance Fluorescence of O<sub>2</sub> Technique*

- does not require accurate knowledge of the satellite position all the time,
- requires precise pointing for the accurate determination of tangent ray height,
- involves little azimuthal movement of the telescope, only zenith scan is required.

### 5.3.2 Data Analysis

#### *Stellar Occultation Technique*

- is simple and efficient

#### *Resonance Fluorescence of O<sub>2</sub> Technique*

- is less efficient because it involves the analysis of both the (0-0) and (0-1) band emissions.

## 5.4 Data Coverage

### 5.4.1 Spatial Coverage

#### *Stellar Occultation Technique*

- covers an altitude region between 70 and 200 km,
- covers a latitude region determined by the orbital inclination,
- covers geographical locations scattered around the orbital track,
- has limited capability of studying particular region of interest.

#### *Resonance Fluorescence of O<sub>2</sub> Technique*

- covers an altitude region between 60 and 150 km,
- covers a latitude region determined by the orbital inclination,
- covers geographical locations systematically along the orbital track.
- has the capability of studying particular region of interest.

### 5.4.2 Temporal Coverage

#### *Stellar Occultation Technique*

- requires special consideration to the instrumental design in order to have a capability of obtaining a complete local time coverage (to perform daytime measurements),
  - daytime measurements require small field-of-view to decrease the contribution from the atmospheric emissions and the scattered sunlight. Very accurate telescope pointing and



knowledge of satellite position thus are required.

- also requires daytime measurement capability in order to be able to obtain a complete seasonal coverage (for high inclination orbits),
  - there will be periods of time in a year that the satellite is continuously exposed in the twilight condition for high inclination orbits.
- time scale is not continuous because of the frequent telescope azimuthal movements,
- has more dead time (time that instrument is not taking measurement).

#### *Resonance Fluorescence of O<sub>2</sub> Technique*

- has the capability of obtaining a complete local time coverage,
- has the capability of obtaining a complete seasonal coverage,
- time scale is continuous,
- has less dead time.

### **5.5 Scientific Merits**

#### *Stellar Occultation Technique*

- is a dedicated technique to measure the density and temperature profiles of the atmosphere.

#### *Resonance Fluorescence of O<sub>2</sub> Technique*

- allows us to investigate the photochemistry of the O<sub>2</sub> Atmospheric band emissions,
- allows us to examine the role that the O<sub>2</sub> photodissociation plays in the Earth's thermal budget (see text),
- allows us to study the effects of planetary and gravity waves in the mesospheric region not only from the measured perturbations of density and temperature, but also from the airglow emissions.

### **5.6 Summary**

The Rayleigh scattering technique is not a viable technique to measure the atmospheric density in the region between 60 and 120 km compared to other two techniques: the stellar occultation and the resonance fluorescence of O<sub>2</sub>. The latter two are equally attractive and both are worthy to be considered and tested for confirmation of science and accuracy requirements.

## 6. CONCEPTUAL INSTRUMENT DESIGN

The conceptual design of an instrument for the remote measurement of upper atmospheric density includes three basic components, i.e., a scanning telescope, a light dispersion unit, and a detector (Figure 6.1). Two instrument types are the leading candidates for the trade-off study during this conceptual design phase; the Image Plane Detector (IPD) Spectrophotometer and the grating spectrometer (GS).

### 6.1 Image Plane Detector Spectrophotometer (IPDS)

The IPDS is an evolutionary combination of a variety of photometer using the Image Plane Detector developed earlier for satellite instruments (Hays, et al., 1981). It is very similar to a tilting filter photometer. It uses a multichannel Image Plane Detector as the spectral selector to detect the emission spectrum dispersed by an interference filter. An extensive description of this low resolution instrument is included in the appendix, and only a brief description is given here.

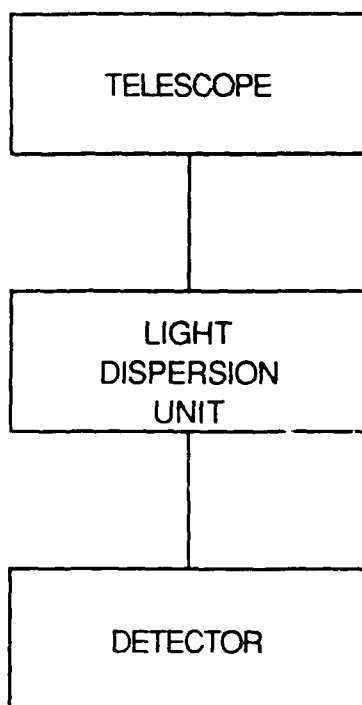


FIGURE 6.1

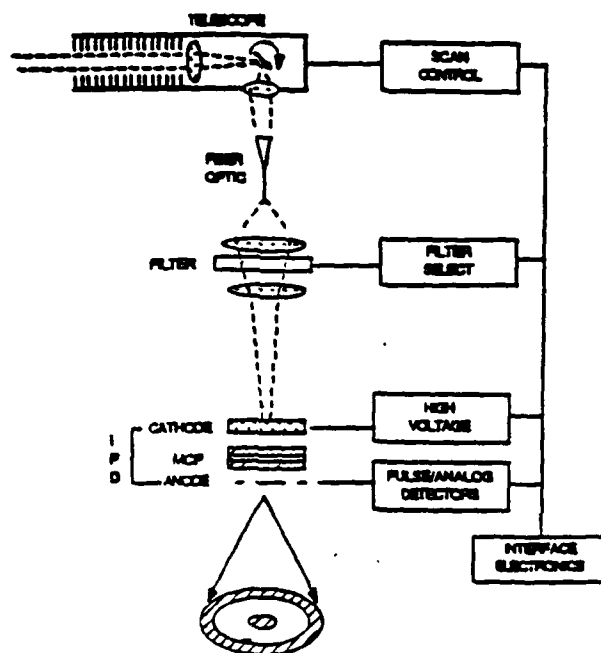


IMAGE PLANE DETECTOR SPECTROPHOTOMETER

Figure 6.2

Figure 6.2 presents a schematic diagram of the instrument. Energy collection is provided by a telescope coupled to a scan mirror (or a scanned telescope) with a fibre optic line-to-circle converter. The line-to-circle converter transforms the rectangular altitude elements; narrow vertical resolution and wide horizontal resolution, to a circular output. The circular output of the energy collection subsystem then feeds the optical energy to a wavelength determination subsystem which consists of a dielectric interference filter. The interference filter has a property that the wavelength of maximum transmission varies with the incident angle of incoming light. It therefore disperses the light coming from all angles and generates an interference pattern which is imaged by the objective lens onto the Image Plane Detector (IPD).

The function of the IPD here is twofold. First, it converts light to electric signals. Light energy is converted to photoelectrons at the photo-cathode, and proximity-focussed to the input of the micro-channel plate imaging multipliers. The imaging electric multipliers amplify the signals by  $\sim 10^6$  and collect them in different concentric, constant area metallic anodes. The second function of an IPD is to collect the light dispersed by the filter so that each anode samples a different part of the spectra with equal wavelength interval. The signals from the anodes are then fed to the amplifiers and sent out to the data collection system for data processing.

## 6.2 Ebert-Fastie Grating Spectrometer (EFGS)

Two experiments meet the criteria for the measurement of neutral density in the altitude region 60-120 km, i.e., stellar occultation and O<sub>2</sub> resonance. In the previous section we discussed the conceptual design of IPDS as it could be used for the remote measurement of atmospheric density by looking at spectral features of the Atmospheric bands of molecular oxygen, i.e., O<sub>2</sub> resonance.

In this section we discuss the conceptual design of the Ebert-Fastie Grating Spectrometer as it could be used for the measurement of O<sub>2</sub> resonance or stellar occultation. Both types of EFGS configurations consist of 1/8th meter Ebert-Fastie monochromators with off-axis telescopes containing spherical mirrors. Both contain plane gratings to disperse the image over the desired spectral range and both detectors would be Charge-Coupled-Devices (CCD) (Figure 6.3). Although the monochromator is expected to be similar for either measurement scheme the design of the telescope, the plane grating, and the CCD are unique to the individual measurement technique as are the operational requirements.

### 1/8 METER SPECTROMETER SYSTEM

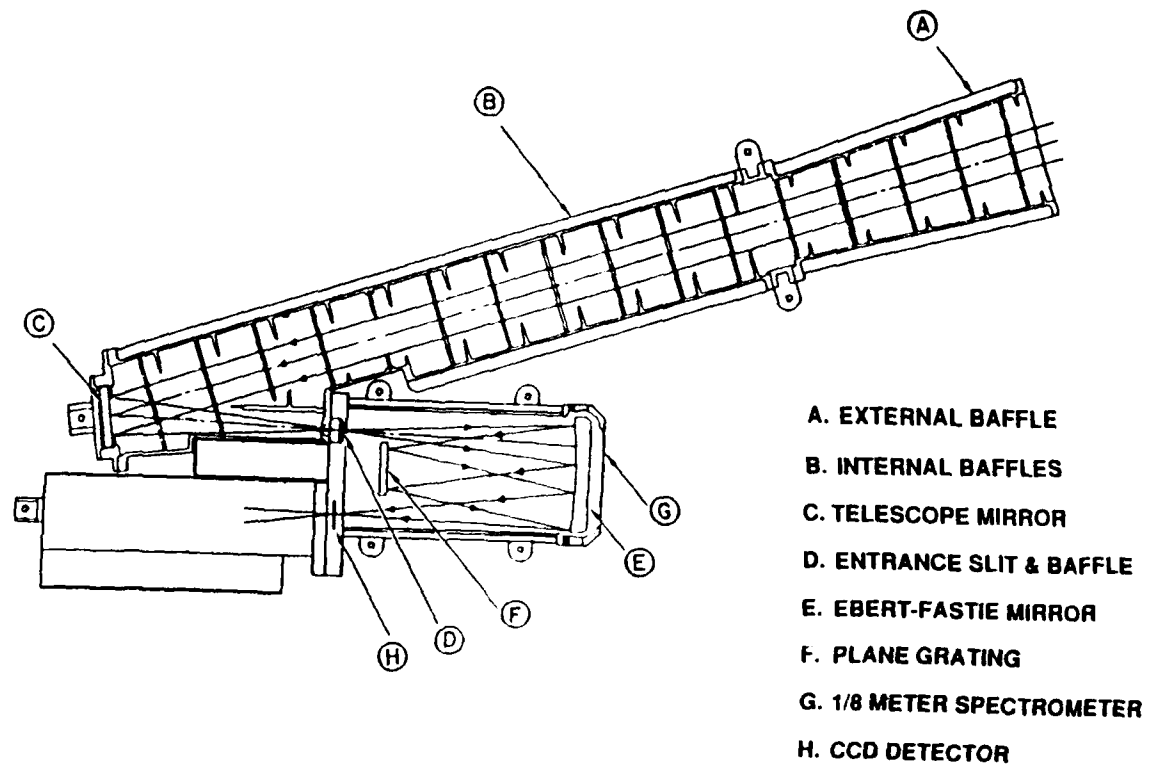


Figure 6.3

## 6.2.1 The O<sub>2</sub> Resonance Measurement

### 6.2.1.1 Field-of-View Determination

It is desirable in a limb measurement to use a low altitude satellite to obtain a large field of view for a given spatial resolution. For the purpose of estimating the requirements on the instrument that will be used for these measurements we can choose a satellite with a circular orbit of 550 km. The orbital inclination angle is arbitrary at this point and depends upon the decision to concentrate on the coverage of the earth's surface (high inclination) or concentrate on coverage of the local times (low inclination). For a satellite positioned 550 km above the earth the line of sight distances to the tangent points at altitudes of 60 km and 120 km are approximately 2560 km and 2400 km respectively. If a height resolution is selected to be 2 km, the field of view, in the vertical, will be

$$\begin{aligned}\delta &= \tan^{-1} \left[ \frac{2 \text{ km}}{2560 \text{ km}} \right] = 0.044938^\circ \\ &= 2.697 \text{ arc min.}\end{aligned}\tag{6.1}$$

### 6.2.1.2 Telescope Selection and Input Slit Width Determination

The initial selection for the telescope has a focal length of 250 mm with an F number of  $f/5$ . If we match the telescope requirements with the required field of view (F.O.V.) for the 2 km resolution we determine the entrance slit width to be  $w=0.196$  mm, i.e.,

$$w = (250 \text{ mm}) \cdot \tan (0.044938^\circ)\tag{6.2}$$

This value relates to a tangent altitude of 60 km. An equivalent calculation shows that the altitude resolution at 120 km, using this slit dimension, would be 1.88 km. We should note, also, that we would need to install a simple light filter to prevent interference from low order harmonic frequencies.

The numerical aperture for the telescope, and spectrometer, is calculated to be

$$f/5_{\text{spec}} = f/5_{\text{tel}} = 1/2 \text{ N.A.} = 1/2 \sin \phi,\tag{6.3}$$

$$2 \sin \phi = 1/5\tag{6.4}$$

$$\phi = \sin^{-1}(0.1) = 5.739 \text{ degrees (half angle)} \quad (6.5)$$

Thus the total field of view for the telescope would be 11.478 degrees.

### 6.2.1.3 Grating Selection

In order to maximize the signal level for our measurement we choose an Ebert-Fastie spectrometer with a focal length of 125 mm (1/8 meters). For a spectrometer of  $f/5$  the grating size is given by

$$D_g \cos \theta = 125/5 \text{ mm} = 25 \text{ mm.} \quad (6.6)$$

where  $\theta$  is the angle of rotation as determined by the spectrometer axis and the normal vector to the plane of the grating. This angle will be determined in a later section.

## EBERT-FASTIE GRATING SPECTROMETER

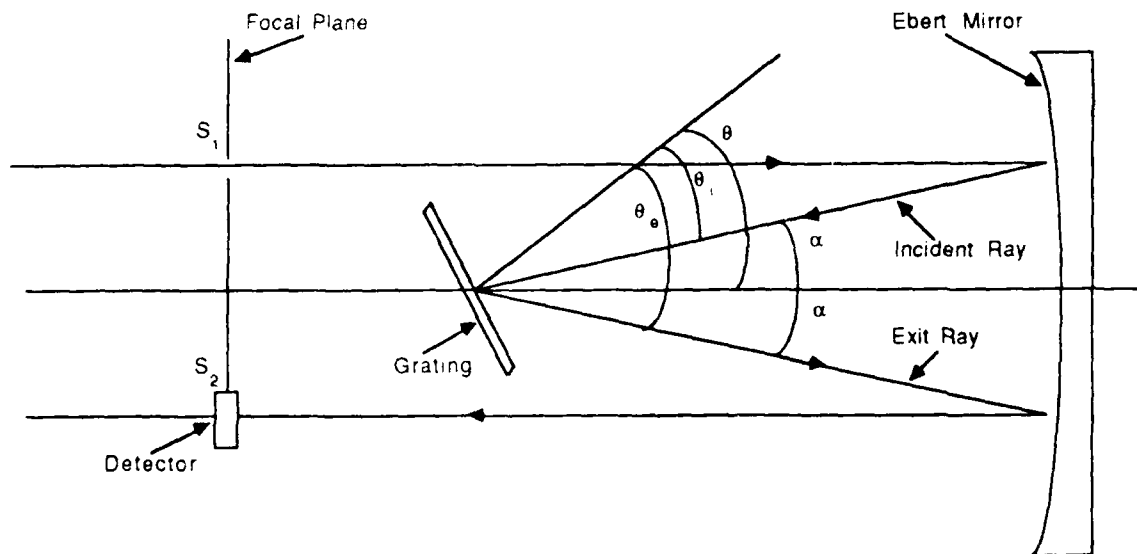


FIGURE 6.4

The grating equation is given as

$$d[\sin(\theta_i) + \sin(\theta_e)] = m\lambda, \quad (6.7)$$

where

$\theta_i$  = incidence angle of the light ray,

$\theta_e$  = exit angle of the light ray,

$d$  = separation of the ruled lines,

$m$  = interference order number,

$\lambda$  = wavelength of the light ray.

The angles  $\theta_i$  and  $\theta_e$  are measured with respect to the coordinates of the plane grating where the x-y plane coincides with the grating surface and the z axis is normal to the surface. These angles can be measured with respect to the spectrometer coordinate system, as shown in Fig. 6.4 where

$s_1$  = inlet slit,

$s_2$  = exit slit (position of the detector),

$\theta$  = the angle defined by the z-axis of the plane grating and the axis of the spectrometer,

$\alpha$  = the angle determined by the incident and exit light rays with respect to the spectrometer axis. Note: this angle is fixed and is determined only by the spectrometer geometry.

The incident and exit angles can be redefined for the spectrometer coordinate system as

$$\theta_i = \theta - \alpha \quad (6.8)$$

$$\theta_e = \theta + \alpha$$

and grating equation becomes

$$d[\sin(\theta - \alpha) + \sin(\theta + \alpha)] = m\lambda, \quad (6.9)$$

or

$$2d \sin \theta \cos \alpha = m\lambda. \quad (6.10)$$

This equation is specific for the Ebert-Fastie spectrometer configuration. The angle  $\alpha$  is a function of the geometry, but for the purpose of preliminary design, may be assumed to have a value on the order of 8-10 degrees. The quantities  $d$ ,  $m$ , and  $\theta$  all depend on the wavelength,  $\lambda$ , and in general are a compromise depending on the specific instrument requirements.

#### *Grating requirements*

The wavelength region for this measurement lies in the near infrared (NIR), 7650Å and 8650Å. If we select 7650Å for  $\lambda$ , and for a starting point choose  $d = 1/1800$  lines/mm, e.g., these are the values that the NUV spectrometer uses in the RAIDS (McCoy, et al., 1986) experiment, then we can determine the values of  $\theta$  as a function of the interference order by using Eq. (6.10).

For example, at  $m = 1$ , and  $\lambda = 7650 \text{ Å}$

$$\begin{aligned} \theta &= \sin^{-1} \left[ \frac{m \lambda}{2 d \cos \alpha} \right] \\ &= 44.193^\circ. \end{aligned} \quad (6.11)$$

If we repeated the last calculation but used a  $\lambda$  equal to 8650Å we could obtain  $\theta$  equal to 52.018°.

#### *Physical size*

Using the  $\theta$  of 44.193° required for a wavelength at 7650Å, we can calculate the dimension of the grating,  $D_g$ , for a 125 mm spectrometer at  $f/5$  from Eq. (6.6),

$$D_g = 30.684 \text{ mm.}$$

Repeating this calculation for  $\lambda$  equal to 8650Å, where  $\theta$  is 52.018°, the value of  $D_g$  becomes 40.623 mm.

If we are to maximize the signal at 8650Å we probably should use the larger physical size for the grating.



### *Grating Dispersion*

The dispersion,  $P_e$ , for a grating spectrometer is calculated by

$$P_e = (mf_{\text{eff.}})/d \cos(\theta_e) \quad (6.12)$$

where

$$f_{\text{eff.}} = 125 \text{ mm,}$$

$$\theta_e = 53.193^\circ \text{ (at } \lambda \text{ equal to } 7650 \text{ \AA),}$$

$$d = 1/1800 \text{ mm,}$$

$$m = 1.$$

The dispersion at the exit position in the focal plane is then calculated to be

$$P_e = 0.037555 \text{ mm/\AA,}$$

$$\text{or about } 26\,6276 \text{ \AA/mm.}$$

Thus the resolution for a slit width of 0.196 mm would be equal to 5.219 Å.

#### 6.2.1.4 Detector Selection: A CCD Device

First, we need to assume something about the CCD. For example, we need to know something about its array size, its dark current, its read noise, its spectral range, its charge collection efficiency, the pixels sizes, and probably some other things but this should get things started. Lets assume that we have a Tektronix CCD (Janesick, et al., 1987). Its array size is 512 x 512 and the individual pixel size is 27  $\mu\text{m}$ . The physical array size is 13.8 x 13.8 mm<sup>2</sup>. A CCD of this physical size gives a length dimension of the inlet slit no greater than 13.8 mm long. It also determines the required dispersion. For example, if we wish to disperse the emission band over the entire face of the CCD we need a large dispersion. Using the dispersion of the exit ray at the focal plane of 0.037555 mm/Å, or inversely 26.6276 Å/mm, one would obtain a spread of 367.5 Å over the face of the CCD.

Carrying out the calculation of the dispersion for  $\lambda = 8650 \text{ \AA}$ , we get

$$P_e = 0.046436 \text{ mm/\AA},$$

or inversely,  $21.53488 \text{ \AA/mm}$ . A wavelength spread of  $297.2 \text{ \AA}$  over the  $13.8 \text{ mm}$  width of the CCD is then obtained.

The two  $\text{O}_2$  Atmospheric bands that we are considering both cover a spectral region about  $200 \text{ \AA}$ . It is therefore reasonable at this point to consider the initial design as adequate.

## 6.2.2 The Occultation Measurement

### 6.2.2.1 Telescope Selection

First we start with an  $f/5$   $125 \text{ mm}$  Ebert-Fastie spectrometer. The telescope should be matched to the spectrometer, i.e., it should have the same F number. Using an objective lens diameter of  $40 \text{ mm}$  which we run a statistical error analysis on (See Section 2), we obtain, for an  $f/5$  telescope, a corresponding focal length of  $200 \text{ mm}$  and numerical aperture (N.A.) of  $5.739$  degrees. Since the total field of view of  $11.478$  degrees ( $2 \times \text{N.A.}$ ) would be too large for the occultation measurement, a field stop is required in order to to exclude the stars other than the one selected. The field stop would be the effective input slit for the spectrometer.

### 6.2.2.2 Grating Selection

In order to maximize the signal level for this measurement we need to match the grating size with the spectrometer, i.e., for an  $f/5$  spectrometer with a focal length of  $125 \text{ mm}$ ,

$$D_g \cos \theta = (125/5) \text{ mm} = 25 \text{ mm} \quad (6.13)$$

where  $\theta$  is the angle of rotation as determined by the spectrometer axis and the normal vector to the plane of the grating surface, and will be determined later.

The grating equation is given as

$$d[\sin \theta_i + \sin \theta_e] = m\lambda, \quad (6.14)$$

where

$$\theta_i = \theta - \alpha$$

$$\theta_e = \theta + \alpha$$

and equation (6.14) can be reduced to give

$$2d \sin \theta \cos \alpha = m\lambda. \quad (6.15)$$

Note that  $\alpha$  is a constant angle as determined by the geometry of the spectrometer. Its value is on the order of  $8^\circ$ - $10^\circ$ . We choose a value of  $9^\circ$  for our calculations.

### *Grating Requirements*

The wavelength region for this measurement lies in the Schumann-Runge Bands, 1750-2000 Å. If we select 1750 Å for  $\lambda$ , and for a starting point choose  $d = 1/1200$  lines/mm we can determine values of  $\theta$  as a function of the interference order by using equation (2).

For example, at  $m_i = 1, 2, \dots$ , and  $\lambda = 1750$  Å then

$$\theta = \sin^{-1} \left\{ \left[ \frac{m \cdot 1750}{2d \cos \alpha} \right] \cdot 10^{-7} \right\} \quad (6.16)$$

and we get the values in Table 6.1.

Table 6.1

m	$\theta$
1	$6.10^\circ$
2	$12.28^\circ$
3	$18.60^\circ$
4	$25.17^\circ$
5	$32.11^\circ$
6	$39.63^\circ$
7	$48.09^\circ$

### *Physical Size*

Using the  $\theta$  of  $18.60^\circ$  at  $m=3$  required for a wavelength at  $1750\text{\AA}$ , we can calculate the dimension of the grating,  $D_g$ , for a 125 mm spectrometer at  $f/5$  from Eq. (6.6),

$$D_g = 26.4 \text{ mm.}$$

### *Grating Dispersion*

The dispersion,  $P_e$ , for a grating spectrometer can be calculated by

$$P_e = (mf_{\text{eff.}})/d \cos(\theta_e) \quad (6.17)$$

where

$$f_{\text{eff.}} = 125 \text{ mm,}$$

$$\alpha \approx 9^\circ \text{ ( assumed ),}$$

$$m = 3,$$

$$\theta_e = 18.60^\circ + 9^\circ = 27.60^\circ,$$

$$d = (1/1200) \text{ mm.}$$

The dispersion at the exit position in the focal plane of the spectrometer is then

$$P_e = 0.05078 \text{ mm/\AA,}$$

or  $19.693 \text{ \AA/mm}$ .

#### 6.2.2.3 Detector Selection: A CCD Device

The CCD assumed for our instrument has an array size of  $512 \times 512$  pixels square. The physical array size is  $13.8 \times 13.8 \text{ mm}^2$ . For a dispersion  $0.05078 \text{ mm/\AA}$  we calculate that we would be able

to spread 271 Å over the surface of the CCD, i.e., we would be able to record on the CCD the entire wavelength spectrum for each selected integration period. The integration period would correspond to the period of time for the tangent height ray to change by 2 km during the occultation sequence as described earlier.

### 6.3 Summary of Instrument Parameters for EFGS

	O <sub>2</sub> Resonance	Stellar Occultation
Wavelength Range (Å)	7550, 8750	1750-2000
F-number	f/5	f/5
Objective Diameter (mm)	50.0	40.0
Field of View (deg <sup>2</sup> )	0.045 x 6.7	3.0 x 3.0
Input Slit Size (mm <sup>2</sup> )	0.196 x 29.1	10.5 x 10.5
Grating Area (mm <sup>2</sup> )	40 x 40	27 x 27
Grating Density (lines/mm)	1800	1200
Interference Order	1	3
Exit Aperture (mm <sup>2</sup> )	13.8 x 13.8	13.8 x 13.8
Detector Array Size	512 x 512	512 x 512
Spectral Coverage (Å)	368, 297*	250
Detector Pixel Size	27 x 27 μm <sup>2</sup>	27 x 27 μm <sup>2</sup>

\* the spectral coverage is given for the lines at 7650 Å and 8650 Å respectively.

## 7. OPERATIONAL REQUIREMENTS

Although some of the operational requirements of the  $O_2$  resonance and stellar occultation measurements are similar, fundamentally the requirements are quite diverse. The optimum orbit plane for either measurement is expected to have an inclination on the order of  $60^\circ$ . This inclination angle would provide global coverage of the earth's surface while, at the same time, providing reasonable local time coverage. It is also desirable for the satellite to have a relatively low earth orbit for either measurement technique but for different reasons.

### 7.1. $O_2$ Resonance

There are two reasons why it is desirable to have a low earth orbit for the  $O_2$  resonance measurement. The 2 km height resolution imposed for the density measurement places a restriction on the spectrometer input slit width dimension that is inversely proportional to the distance between the position of the satellite and the tangent height altitude. Any reduction in slit width is inversely proportional to the amount of light flux that can be passed through the instrument which effectively reduces the signal to noise. But, perhaps, a more important consideration relates to the pointing requirements for resonance measurement. We not only need to resolve 2 km altitude increments discussed above, over the altitude range 60 - 120 km but we need to know precisely where these height increments lie such that we can calculate the integrated contents of each height package within 5%. If we assume an isothermal atmosphere then the density can be expressed as

$$\rho = \rho_0 e^{-\frac{\Delta h}{H}} \quad (7.1)$$

where

$\rho_0$  = density at  $h_0$ ,

$\rho$  = density at  $h_0 + \Delta h$ ,

$H$  = density scale height.

The uncertainty in the computed density due only to the uncertainties in these parameters can be expressed as

$$\delta \rho = \sqrt{\left(\frac{\partial \rho}{\partial \rho_0}\right)^2 (d\rho_0)^2 + \left(\frac{\partial \rho}{\partial H}\right)^2 (dH)^2 + \left(\frac{\partial \rho}{\partial \Delta h}\right)^2 (d\Delta h)^2} \quad (7.2)$$

where

$$\frac{\partial \rho}{\partial \rho_0} = e^{-\frac{\Delta h}{H}}, \quad (7.3)$$

$$\frac{\partial \rho}{\partial H} = \frac{\Delta h}{H} e^{-\frac{\Delta h}{H}}, \quad (7.4)$$

$$\frac{\partial \rho}{\partial \Delta H} = -\frac{\rho_0}{H} e^{-\frac{\Delta h}{H}}, \quad (7.5)$$

with  $\delta \rho$ ,  $\delta \rho_0$ ,  $\delta H$  and  $\delta \Delta h$  the uncertainties in the respective parameters. For the purpose of determining the pointing requirements imposed on the satellite we can ignore the uncertainty in the density scale height,  $H$ , and  $\rho_0$ , the reference density, which leaves

$$\delta \rho = \sqrt{\left( -\frac{\rho_0}{H} e^{-\frac{\Delta h}{H}} \right)^2} (\delta \Delta h)^2 \quad (7.6)$$

or

$$\frac{\delta \rho}{\rho} = \frac{\Delta h}{H}. \quad (7.7)$$

Now if we require a 5% uncertainty in the density and if we select any reasonable value for the scale height, for example select  $H = 7.0$  km, then the corresponding uncertainty in the altitude is found to be 0.350 km. In section 6.2 we found that the distance from the satellite to the tangent height altitude was approximately 2560 km, for a 550 km circular orbit altitude, thus we can define an angle

$$\psi_p = \tan^{-1} \left[ \frac{0.350}{2560} \right] = 0.007833;$$

$$\psi_p = 0.4700 \text{ minutes}^{-1}, \quad (7.8)$$

$$\psi_p = 28.2 \text{ seconds}^{-1}.$$

Thus for a remote measurement of O<sub>2</sub> resonance the pointing requirements are rather stringent. The pointing accuracy would have to be on the order of 20 arc seconds.

While the pointing accuracy is rather severe for this measurement technique accurate knowledge of the satellite position is not critical. The uncertainty in this parameter is translated into an uncertainty in the measurement track. The measurement bins, i.e., the horizontal dimensions, are not expected to be impacted by normal tracking uncertainties.

Both of the instrument types that could be employed for the O<sub>2</sub> resonance measurement, the Image Plane Detector Spectrophotometer (IPDS) and the Ebert-Fastie Grating Spectrometer (EFGS), have the same satellite operational requirements. In addition to the pointing requirements described above, the instrument telescope must be capable of 360 degree movement in azimuth and approximately 10 degrees in elevation with respect to a stabilized platform that is fixed horizontal to its sub-satellite position. The instrument telescope should, at all times, be pointed at ~90° away from the sun vector to avoid the scattered sunlight. The measurement can be obtained in daytime and/or nighttime conditions.

## 7.2 Stellar Occultation

As we have discussed in the previous section on the O<sub>2</sub> resonance technique, the atmospheric density was resolved in 2 km layers by imaging the contents of a spectrometer input slit, of appropriate width, onto a CCD while the telescope, or telescope mirror, was sequentially scanned over the 60-120 km altitude region. We also found that the accuracy in the measured density profile was tied directly to our knowledge of the pointing direction and that if we want to measure with 5% accuracy we need good pointing accuracy, on the order of 20 arc seconds.

In contrast, the stellar occultation measurement resolves the layered density information by selecting appropriate integration periods as the occulted star descends on the earth's horizon aft of the satellite motion. It is desirable to have a low orbital altitude to increase the occultation period and corresponding integration time per altitude increment.

Also in section 7.1 we found the necessity of resolving the tangent height to approximately 0.350 km in order to obtain a 5% measure of atmospheric density. For the occultation measurement an error in satellite position induces a tangent height measurement error. If we refer to Figure 7.1 we see that



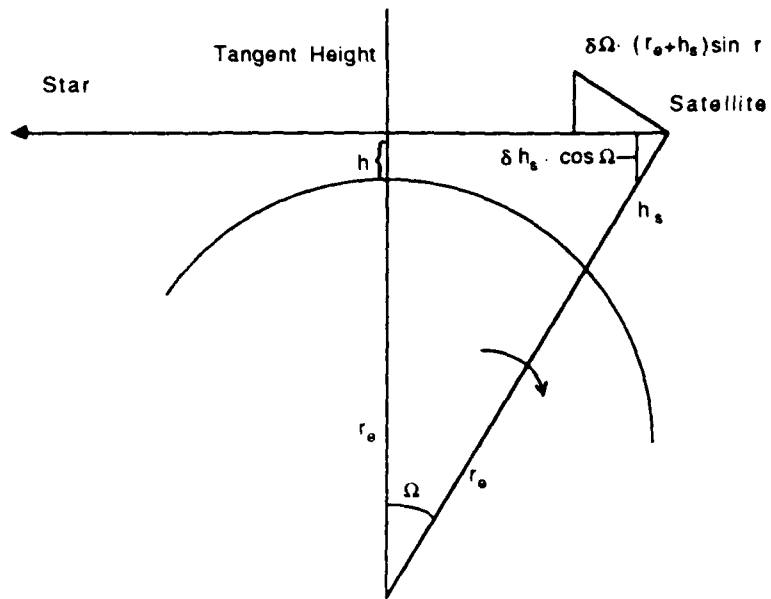


Figure 7.1

$$\cos(\Omega) = (r_e + h) / (r_e + h_s) \quad (7.9)$$

$$h = (r_e + h_s) \cos(\Omega) + r_e \quad (7.10)$$

where

$W$  = satellite nadir angle =  $21.69^\circ$  (at assumed) condition).

$r_e$  = radius of earth (assumed to be 6371 km),

$h_s$  = satellite altitude (assumed to be 550 km),

$h$  = tangent height altitude.

$W_s$  = satellite radian frequency

=  $1.095755 \times 10^{-3}$  rad./sec. (at assumed altitude)

Note: Off orbital track error considered negligible for this calculation.

The uncertainty in the tangent height altitude as a function of the variable parameters can be expressed as

$$\delta h = \sqrt{\left(\frac{\partial h}{\partial h_s}\right)^2 \left(dh_s\right)^2 + \left(\frac{\partial h}{\partial \Omega}\right)^2 \left(d\Omega\right)^2}, \quad (7.11)$$

where

$$\frac{\partial h}{\partial h_s} = \cos \Omega, \quad (7.12)$$

$$\frac{\partial h}{\partial \Omega} = -(r_e + h_s) \sin \Omega, \quad (7.13)$$

thus

$$\delta \Omega \approx W_s \delta t. \quad (7.14)$$

From equation (7.6) we see that, in order to resolve 0.350 km in the tangent height altitude the uncertainty in the satellite altitude would have to be

$$\delta h_s < \frac{\delta h}{\cos \Omega} \approx \frac{0.350}{\cos 21.69} \approx 0.377 \text{ km} \quad (7.15)$$

and the uncertainty in the nadir angle would have to be

$$\begin{aligned} \delta \Omega &< \frac{\delta h}{(r_e + h_s) \sin \omega} \\ &< 1.368 \times 10^{-4} \text{ radian,} \end{aligned} \quad (7.16)$$

and we can translate the uncertainty in angle to an uncertainty in time, through Eq. (7.7),

$$\delta t < \frac{1.368 \times 10^{-4}}{1.095755 \times 10^{-3}} = 0.125 \text{ seconds} \quad (7.17)$$

These calculations were made for a specific satellite altitude and tangent height measurement in order to establish the order of magnitude for the parameter uncertainties.

## References

- Allison, A.C., A. Dalgarno, and N. W. Pasachoff, (1971) Absorption by vibrationally excited molecular oxygen in the Schumann-Runge continuum, Planet. Space Sci., **19**, 1463.
- Allison, A.C., S. L. Guberman, and A. Dalgarno, (1986) A model of the Schumann-Runge Continuum of O<sub>2</sub>, J. Geophys. Res., **91**, 10193.
- Atreya, S. K., (1981) Measurement of Minor Species (H<sub>2</sub>, Cl, O<sub>3</sub>, NO) in the Earth's Atmosphere by the Occultation Technique, Planetary Aeronomy and Astronomy, (S. K. Atreya, and J. J. Caldwell, ed.) Pergamon Press, 127.
- Babcock, H. D., and L. Herzberg, (1948) Fine structure of the red system of atmospheric oxygen bands, Astrophys. J., **108**, 167.
- Banks, P. M. and G. Kockarts, (1973), *Aeronomy*, Academic Press.
- Bucholtz, A., W.R. Skinner, V. J. Abreu, and P. B. Hays, (1986) The Dayglow of the O<sub>2</sub> Atmospheric Band system, Planet. Space Sci., **34**, 1031.
- Buisson, H., G. Jausseran, and P. Rouard, (1933) La transparence de la basse atmosphere, Rev. Opt., **12**, 70.
- Campbell, I. M., and C. N. Gray, (1973) Rate constants for O(<sup>3</sup>P) recombination with N(<sup>4</sup>S), Chem. Phys. Lett., **18**, 607.
- Chamberlain, J. W., C. Y. Fan, and A. B. Meinel, (1954) A new O<sub>2</sub> band in the infrared auroral spectrum, Astrophys. J., **120**, 560.
- Champion, K. S. W., (1986) Atmospheric Structure for Low Altitude Satellite and Aerobraked Orbital Transfer Vehicles, AIAA 24th Aerospace Sciences Meeting, Reno, Nevada, Jan., paper AIAA-86-0186.
- Cheung, A. S.-C., K. Yoshino, W. H. Parkinson, and D. E. Freeman, (1984) Herzberg Continuum Cross Section of Oxygen in the Wavelength Region 193.5-204.0 nm and Band Oscillator Strength of the (0,0) and (1,0) Schumann-Runge Bands, Can. J. Phys., **62**, 1752.
- Cheung, A. S.-C., K. Yoshino, W. H. Parkinson, S. L. Guberman, and D. E. Freeman, (1986a) Absorption Cross-section Measurements of Oxygen in the Wavelength Region 195-241 nm of the Herzberg Continuum, Planet. Space Sci., **34**, 1007.
- Cheung, A. S.-C., K. Yoshino, W. H. Parkinson, D. E. Freeman, (1986b) Molecular Spectroscopic constants of O<sub>2</sub>(B<sup>3</sup>Σ<sub>u</sub><sup>-</sup>): The upper state of the Schumann-Runge bands, J. Mole Spect., **119**, 1.
- Clancy, R. Todd, (1986) El Chichon and "Mystery Cloud" aerosols between 30 and 55 km Global observations from the SME Visible Spectrometer, Geophys. Res. Lett., **13**, No. 9 937-940.
- Deans, A. J., and G. G. Shepherd, (1976) A rocket measurement of the O<sub>2</sub> (b<sup>1</sup>Σ<sub>g</sub><sup>+</sup> - X<sup>3</sup>Σ<sub>g</sub><sup>-</sup>

- atmospheric band nightglow altitude distributions, Geophys. Res. Lett., **3**, 441.
- Ditchburn, R. W., and P. A. Young, (1962) The Absorption of Molecular Oxygen Between 1850 and 2500 Å, J. Atmos. Terr. Phys., **24**, 127.
- Frederick, J. E., and R. Hudson, (1980) Dissociation of Molecular Oxygen in the Schumann-Runge Bands, J. Atmos. Sci., **37**, 1099.
- Gauthier, M., and D. R. Snelling, (1970) Formation of singlet molecular oxygen from the ozone photochemical system, Chem. Phys. Lett., **5**, 93.
- Gauthier, M., and D. R. Snelling, (1971) Mechanism of singlet molecular oxygen formation from photolysis of ozone at 2537 Å, Chem. Phys., **54**, 4317.
- Götz, F. W. P., and H. Maier-Leibnitz, (1933) Zur Ultraviolett Absorption Bodennaher Luftschichten, Z. Geoph., **9**, 253.
- Greer, R. G. H., E. J. Llewellyn, B. H. Solheim, and G. Witt, (1981) The excitation of  $O_2(b^1\Sigma_g^+)$  in the nightglow, Planet. Space Sci., **29**, 383.
- Hall, L. A., W. Schweizer, and H. E. Hinteregger, (1965) Improved Extreme Ultraviolet Absorption Measurements in the Upper Atmosphere, J. Geophys. Res., **70**, 105.
- Hays, P. B., and R. G. Roble, (1968) Atmospheric Properties from the Inversion of Planetary Occultation Data, Planet. Space Sci., **16**, 1197.
- Hays, P. B., and R. G. Roble, (1968) Stellar Spectra and Atmospheric Composition, J. Atmos. Sci., **25**, 1141.
- Hays, P. B., and R. G. Roble, (1973) Stellar Occultation measurements of Molecular Oxygen in the lower thermosphere, Planet. Space Sci., **21**, 339.
- Hays, Paul B., (1988), private communication, University of Michigan.
- Herzberg, G., (1950) *Spectra of Diatomic Molecules*, Van Nostrand, New York.
- Hinteregger, H. E., and L. A. Hall, (1969) Thermospheric Densities and Temperatures from EUV Absorption Measurements by OSO-III, Space Res., **IX**, 519. North-Holland.
- Hudson, Robert D., and Stephen H. Mahle, (1972) Photodissociation Rates of Molecular Oxygen in the Mesosphere and Lower Thermosphere, J. Geophys. Res., **77**, 2902.
- Hudson, R. D., Virginia L. Carter, and J. A. Stein, (1966) An Investigation of the Effect of Temperature on the Schumann-Runge Absorption Continuum of Oxygen, 1580-1950 Å, J. Geophys. Res., **71**, 2295.
- Huffman, R. E., Y. Tanaka, and J. C. Larrabee, (1964) Nitrogen and oxygen absorption cross sections in the vacuum ultraviolet, Discussions Faraday Soc., **37**, 159.
- Janesick, et al., (1987), Optical Engineering, Aug., **26**, No. 8, 692.
- Johnson, F. S., J. D. Purcell, and R. Tousey, (1951) Measurements of the Vertical Distribution of Atmospheric Ozone from Rockets, J. Geophys. Res., **56**, 583.
- Killeen, T. L., and P. B. Hays, (1984) Doppler line profile analysis for a multichannel Fabry-

- Perot interferometer, Appl. Opt., **23**, 612.
- Kreusler, H., (1901) Ann. Phys., **6**, 412.
- Ladenburg, R., and C. C. Van Voorhis, (1933) The Continuous Absorption of Oxygen Between 1750 and 1300 Å and its Bearing Upon the Dispersion, Phys. Rev., **43**, 315.
- Lewis, B. R., L. Berzins, and J. H. Carver, (1987) Predissociation Linewidths for the Schumann-Runge Bands of  $^{16}\text{O}^{18}$ , J. Quant. Spectros. Radiat. Transfer, **37**, 243.
- McClatchey, R. A., et al., (1973) AFCRL Atmospheric absorption line parameters compilation, AFCRL-TR-73-0096, AD762904.
- McDade, I. C., D. P. Murtagh, R. G. H. Greer, P. H. G. Dickinson, G. Witt, J. Stegman, E. J. Llewellyn, L. Thomas, and D. B. Jenkins, (1986) ETON 2: Quenching parameters for the proposed precursors of  $\text{O}_2(\text{b}^1\Sigma_g^+)$  and  $\text{O}(^1\text{S})$  in the terrestrial nightglow, Planet. Space Sci., **34**, 789.
- Meinel, A. B., (1950c.)  $\text{O}_2$  emission bands in the infrared spectrum of the night sky, Astrophys. J., **112**, 464.
- Meinel, A. B., (1951) The auroral spectrum from 6200 to 8900 Å, Astrophys. J., **113**, 583.
- Metzger, P. H. and Cook, G. R., (1964) A reinvestigation of the absorption cross sections of molecular oxygen in the 1050-1800 Å region, J. Quant. Spectrosc. Radiat. Transfer, **4**, 107.
- Mie, G., (1908) Beitrage zur optik trueber Medien, Speziell koloidaller metaloesungen, Ann. der Phys., **25**, 377.
- Naudet, J. P., and Thomas, G. E. (1987) Aerosol optical depth and planetary albedo in the visible from the Solar Mesosphere Explorer, J. Geophys. Res., **92**, No. D7, 8373-8381.
- Nicholls, R. W., (1965) Franck-Condon Factors to high vibrational quantum numbers V:  $\text{O}_2$  band systems, J. Res. NBS, **69A**, 369.
- Omidvar, K., and J. E. Frederick, (1987) Atmospheric Odd Oxygen Production Due to the Photodissociation of Ordinary and Isotopic Molecular Oxygen, Planet. Space Sci., **35**, 769.
- Packer, D. M., (1961) Altitudes of the night airglow radiations, Ann. Geophys., **17**, 67.
- Roble, R.G., and P. B. Hays, (1972) A Technique for Recovering the Vertical Number Dnesity Profile of ATmospheric Gases from Planetary Occultation Data, Planet. Space Sci., **20**, 1727.
- Rusch, D.W., G.H. Mount, J.M. Zawodny, C.A. Barth, G.J. Rottman, R.J. Thomas, G.E. Thomas, T.W. Sanders, and G. M. Lawrence, (1983) Temperature Measurements in the Earth's Stratosphere Using a Limb Scanning Visible Light Spectrometer, Geophy. Res.Lett., **10**, 261.
- Skinner, W.R., and P.B. Hays, (1985) Brightness of the  $\text{O}_2$  Atmospheric Bands in the Daytime Thermosphere, Planet. Spce Sci., **33**, 17.
- Slanger, T. G., and Black, G., (1977)  $\text{O}(^1\text{S})$  in the lower thermosphere Chapman vs. Barth, Planet. Space Sci., **25**, 79.

- Steinbach, W., and W. Gordy, (1975) Microwave Spectrum and Molecular Constants of  $^{16}\text{O}^{18}\text{O}$ , Phys. Rev. A, **11**, 729.
- Tatum, J. B., and J. K. G. Watson, (1971) Rotational Line Strengths in  $^3\Sigma^+-^3\Sigma^+$  Transitions with Intermediate Coupling, Can. J. Phys., **49**, 2693.
- Thomas, Gary E., and McKay, Christopher P., (1985) On the mean particle size and water content of polar mesospheric clouds, Planet. Space Sci., **33**, No. 10, 1209-1224.
- Torr, Marsha R., D. G. Torr, and R. R. Laher, (1985) The  $\text{O}_2$  atmospheric 0-0 band and related emissions at night from spacelab 1., J. Geophys. Res., **90**, 8525.
- Van de Hulst, H. C., (1957) Light Scattering by Small Particles, Wiley, New York.
- Venkateswaran, S. V., J. G. Moore, and A. J. Krueger, (1961) Determination of the Vertical Distribution of Ozone by Satellite Photometry, J. Geophys. Res., **66**, 1751.
- Wallace, L., and Chamberlain, (1959) Excitation of  $\text{O}_2$  atmospheric bands in the aurora, Planet. Space Sci., **2**, 60.
- Wallace, L., and D.M. Hunten, (1968) Dayglow of the Oxygen A Band, J. Geophys. Res., **73**, 4813.
- Wasser B. and T. M Donahue, (1979) Atomic Oxygen between 80 and 120 km: Evidence for Latitudinal Variation in Vertical Transport Near the Mesopause, J. Geophys. Res., **84**, 1287.
- Watanabe, K., M. Zelikoff, and E. C. Y. Inn, (1953) Absorption Coefficients of Several Atmospheric Gases, Geoph. Res. Papers, No. 21, 1-80.
- Watanabe, T., N. Masatoshi, and T. Ogana, (1981) Rocket measurements of  $\text{O}_2$  atmospheric and OH Meinel bands in the airglow, J. Geophys. Res., **86**.
- Wilkinson, P. G., and R. S. Mulliken, (1957) Dissociation Process in Oxygen Above 1750 Å. Ap. J., **125**, 594.
- Witt, G., J. Stegman, B. H. Solheim, and E. J. Llewellyn, (1979) A measurement of the  $\text{O}_2$  ( $b^1\Sigma_g^+ - X^3\Sigma_g^-$ ) atmospheric band and the  $\text{OI}(^1\text{S})$  greenline in the nightglow, Planet. Space Sci., **27**, 341.
- Yoshino, (1988), private communication.
- Yoshino, K., D. E. Freeman, J. R. Esmond, and W. H. Parkinson, (1987) High Resolution Absorption Cross-Sections and Band Oscillator Strengths of the Schumann-Runge Bands of  $\text{O}_2$  at 79 K, Planet. Space Sci., **35**, 1067.
- Yoshino, K., D. E. Freeman, and W. H. Parkinson, (1984) Atlas of the Schumann-Runge Absorption Bands of  $\text{O}_2$  in the Wavelength Region 175-205 nm, J. Phys. Chem. Ref. Data, **13**, 207.
- Yoshino, K., D. E. Freeman, J. R. Esmond, and W. H. Parkinson, (1983) High Resolution Absorption Cross-section Measurements and Band Oscillator Strengths of the (1.0)-(12.0) Schumann-Runge Bands of  $\text{O}_2$ , Planet. Space Sci., **31**, 339.

APPENDIX I

**Image Plane Detector spectrophotometer (IPDS)  
— Application to O<sub>2</sub> atmospheric band nightglow**

Mingzhao Luo  
Jeng - Hwa Yee  
and  
Paul B. Hays

University of Michigan  
Department of Atmospheric & Oceanic Science  
Space Physics Research Laboratory  
Ann Arbor, Mich 48109-2143

Submitted to Applied Optics, 1987

## Abstract

A new variety of low resolution spectrometer is described in this study. This device, an Image Plane Detector Spectrophotometer, has high sensitivity and modest resolution sufficient to determine the rotational temperature and brightness of molecular band emissions. It uses interference filter as dispersive element and a multichannel Image Plane Detector (IPD) as photon collecting device. The data analysis technique used to recover the temperature of the emitter and the emission brightness is presented. The 'Atmospheric' band of molecular oxygen is used to illustrate the application of the device.



## I. Introduction

The temperature of emitting atoms or molecules is reflected in their spectral line shape or the emission band structure.<sup>1</sup> The width of an individual atomic or molecular line can be used to obtain the doppler temperature.<sup>2,3</sup> This is, however, difficult for the emissions originating in the mesosphere where the temperature is low and the line width is narrow. Under these circumstances, a high resolution instrument is required. An alternative remote sensing technique to monitor the temperature is to obtain the rotational temperature from the molecular band structure by using a scanning spectrometer.<sup>4,5</sup> A finite period of time is usually required to scan a whole emission band system, consequently lowering the temporal resolution. For a measurement made by instruments on board rocket or satellite, this would result in a lower spatial resolution. Our intent here is to design a spectrophotometer with a relatively high throughput and with spectral resolution sufficient to resolve the molecular band structure without the necessity of scanning.

The tilting-filter photometer has been used frequently in the past to examine the emissions in the airglow and aurora.<sup>6-8</sup> It has a spatially fixed aperture, and the wavelength scan is carried out by mechanically tilting the filter with respect to the optical axis of the instrument. Although it has relatively high throughput, its instrument broadening varies with tilt angles of the filter, and consequently, the wavelength. In order to correct this problem, a multi-spiral sector spectrophotometer was developed.<sup>9</sup> In this instrument a field stop, made of a sector shaped masking disk and a disk with a spiral slit, was put in front of the detector so that the signals of the emission can be selectively collected at a given wavelength range. The spectral scan is accomplished by rotating the spiral slit, and is capable of obtaining a nearly constant peak transmittance and band pass for large tilt angles. This instrument has been successfully used in monitoring auroral O<sup>+</sup> (<sup>2</sup>P - <sup>2</sup>D) emissions at 7320Å by Swenson *et al.*<sup>9</sup> Both the tilting-filter photometer and the spiral spectrophotometer scan the selected spectrum by either tilting the interference filter to shift the center wavelength or moving a shaped aperture across the interference pattern created by a dielectric interference filter, while the detector (photomultiplier) is in a fixed position.

The instrument described here is very similar in principle to the tilting-filter photometer and the spiral spectrophotometer. It uses a multichannel Image Plane Detector (IPD) as the spectral selector to detect the emission spectrum dispersed by an interference filter. The Image Plane Detector was first used on the Fabry-Perot Interferometer flown on the Dynamic Explorer Satellite.<sup>10</sup> The geometrical parameters and characteristics of the IPD have been described in details by Killeen *et al.*<sup>11</sup> In brief, the IPD is an electro-optical device which converts the intensity distribution of light falling on the image plane into a set of discrete electron pulse. It collects the light falling on several

equal area annular anodes, arranged in the shape of a 'Bullseye' pattern. This pattern, as we shall see, is such that every channel samples a range of the spectrum with equal wavelength interval. The usage of the IPD make this photometer not only have almost identical transmission function for each channel, but also be able to obtain spectral information with no mechanical scanning.

This paper will describe a low resolution spectrophotometer using Image Plane Detector (IPD) as the spectral selector. The data analysis technique to recover the brightness of the emission source and the rotational temperature of the emission band will be discussed as will the associated errors. The  $O_2$  (0-1) atmospheric band emission will be used as an example for demonstration.

## II. Description of the Image Plane Detector Spectrophotometer

The instrument discussed here is intended to measure the molecular emission band structure with relatively low spectral resolution. It consists of three major elements: interference filter, objective lens and Image Plane Detector. The schematic diagram of the instrument is shown in figure 1. The light coming from a radiative source is collected and passes through the interference filter with a wide angular range. The interference filter here acts as a spectrum separating elements, generating an interference pattern which is imaged by the objective lens onto an Image Plane Detector (IPD). In principle, the interference filter is a Fabry-Perot etalon with very narrow spacer. For a monochromatic incident light, a concentric Fabry-Perot ring pattern, characterized by a gradually narrowing fringe width with increasing radial distance from the optical axis, can be formed. A single fringe here corresponds to the maximum light transmission at the special wavelength of the incoming light. The Image Plane Detector uses a concentric-ring multiple anode and incorporates a three-stage microchannel plate electron multiplier. The unique anode pattern shape of the IPD was designed to match the interference pattern formed by the filter or etalon so that the equal area anodes monitor the equal interval of the wavelength spectrum.

The relationship between incident angle of light  $\theta$  to the filter surface normal and the wavelength of maximum transmission  $\lambda_\theta$  is given by <sup>6</sup>

$$\frac{\lambda_\theta - \lambda_0}{\lambda_0} = - \frac{\theta^2}{2 \mu^{*2}}, \quad (1)$$

where  $\lambda_0$  is the wavelength of maximum transmittance for  $\theta = 0^\circ$ , and  $\mu^*$  is an effective refractive

AD-A199 292

REMOTE MEASUREMENT OF UPPER ATMOSPHERIC DENSITY A

2/2

FEASIBILITY STUDY(U) MICHIGAN UNIV ANN ARBOR SPACE

PHYSICS RESEARCH LAB P B HAYES ET AL. 10 JUN 88

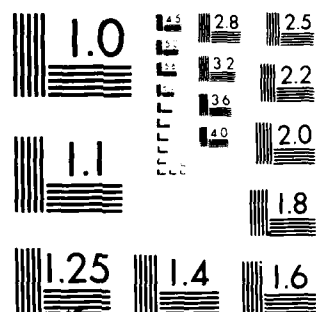
UNCLASSIFIED

AFGL-TR-88-0139 F19628-87-K-0039

F/G 16/2

NL

END  
DATE  
FILMED  
11 88



MICROCOPY RESOLUTION TEST CHART  
NATIONAL BUREAU OF STANDARDS-1963-A

index of the filter which lies between the two refractive indices of the dielectric materials. The center wavelength  $\lambda_0$ , the width of the filter and the focal length of the objective lens have to be selected based on the spectral coverage of the emission of interest. It can be seen from equation (1) that as the incident angle of light increases, the  $\lambda_\theta$  shifts toward shorter wavelength. Therefore in order to use the filter as the spectrum dispersive element, the center wavelength of the filter  $\lambda_0$  has to be selected at the longest possible wavelength of any emission band to be monitored. The outmost anode of the IPD measures the light coming from the maximum incident angle  $\theta_{\max}$ , consequently determining the instrument field of view and the spectral coverage. The width of the filter and the focal length of the objective lens have to be chosen so that the instrument transmission function not only be able to cover the whole emitting band, but also be able to resolve the features observed by two adjacent anodes.

In order to illustrate this issue we consider a theoretical double cavity interference filter shown in figure 2, built by following Lissberger's theory.<sup>12</sup> The two refractive indices for the dielectric materials are 2.30 and 1.35 respectively. The center wavelength, at which the transmission is maximum for normal incident light, is selected to be 8730 Å, corresponding to the longest wavelength of O<sub>2</sub> (0-1) atmospheric band, and the full width at half maximum transmittance (FWHM) is about 12 Å. The effective refractive index  $\mu^*$  for this filter is about 1.49. From equation (1), the center wavelength shift,  $\lambda_\theta - \lambda_0$ , is proportional to the square of the incident angle  $\theta^2$ . Therefore in order for the instrument to have a spectral coverage of about 150 Å (the spectrum range of O<sub>2</sub> (0-1) atmospheric band), the maximum  $\theta$  should be in the neighborhood of 15°. Figure 3 shows the filter transmission functions  $T_k$  for twelve different incident angles  $\theta_k$ , where  $\theta_k = (k - 1)^{1/2} \theta_c$ , and  $k = 1, 2, \dots, 12$ . The angle  $\theta_1$  corresponds to the normal incident angle and equals to zero, and angle  $\theta_{12} = \theta_c$  is selected so that by using the filter shown in figure 2, the transmission function at two adjacent angles  $\theta_k$  and  $\theta_{k+1}$  can be clearly resolved. Here,  $\theta_c$  is equal to 4.4°. The anode geometry of the detector allows us to collect light signals at different wavelength dispersed by the filter, and subsequently defines the focal length of the objective lens required for the instrument. Note that a 12 channel IPD similar to the one used in the Fabry-Perot interferometer on board the Dynamic Explorer Satellite<sup>11</sup> is used here. As the geometric parameter or the number of anodes of the IPD changes,  $\theta_c$  will be different. The focal length of the objective lens in this case is determined to be 2.27 cm.

Due to the finite width of the detector ring, the instrument transmission function  $T_k$  at a given anode  $k$  is broadened and can be evaluated as

$$\bar{T}_k(\lambda) = \frac{1}{\Omega_k} \int_0^{2\pi} d\phi \int_0^{\pi} T(\lambda, \theta) D_k(\theta) \sin \theta d\theta, \quad (2)$$

with

$$\begin{aligned} D_k(\theta) &= 1 & \theta_k < \theta < \theta_k + \Delta\theta_k \\ &= 0 & \text{else,} \end{aligned}$$

where  $\Omega_k$  is the field of view of the k-th anode,  $T(\lambda, \theta)$  is the filter transmission function, and  $\theta_k$ ,  $\theta_k + \Delta\theta_k$  are the angles defined by k-th anode of the detector assuming that  $D_k$  is an ideal square function. Here  $T_k$  is normalized by  $\Omega_k$  so that the peak transmission is unity.

For small angles of  $\theta$ , equation (2) can be approximated as

$$\bar{T}_k(\lambda) = \frac{1}{\Omega_k} \int_0^{2\pi} d\phi \int_0^{\pi} T(\lambda, \theta) D_k(\theta) \theta d\theta. \quad (3)$$

Writing equation (3) in terms of  $\lambda$  from its relationship with  $\theta$ , one obtains

$$\bar{T}_k(\lambda) = -\frac{2 \mu^2 \pi}{\Omega_k \lambda_0} \int_0^{\infty} T(\lambda, \lambda_{\theta}) D_k(\lambda_{\theta}) d\lambda_{\theta}. \quad (4)$$

The normalized square function  $D_k(\lambda_{\theta})$  limits the integration between two center wavelengths which correspond to the inner and outer edges of the k-th detector ring. Mathematically,  $T_k$  can be considered as a convolution of the filter transmission function  $T(\lambda, \theta)$  and a detector broadening square function  $D_k'$ ,

$$\bar{T}_k = T * D_k', \quad (5)$$

where

$$\begin{aligned} D_k' &= 1/\Delta\lambda_{\theta k} & |\lambda_{\theta} - \lambda| < \Delta\lambda_{\theta k} \\ &= 0 & \text{else,} \end{aligned}$$

and

$$\Delta\lambda_{\theta k} = -\frac{\lambda_0 \Omega_k}{2\pi\mu^2}.$$

Figure 4 presents the simulated instrument transmission functions  $T_k$  multiplying by  $\Omega_k$  for the 12 channels of the IPD. The result is calculated based upon the convolution of the double cavity interference filter transmission function (Figure 3) and the transmission function, represented by a square function, of the 12 channel IPD. We note the constant spectral resolution for this device, compared to devices like tilting filter photometer which exhibits large changes in resolution with wavelength shift.

If the radiative source of interest is a molecular emission band, one can obtain the output in counts for the k-th channel as

$$\begin{aligned} N_k &= \frac{10^6}{4\pi} R_s A_0 Q \Delta t [B(\lambda) * \bar{T}_k \Omega_k] + \frac{10^6}{4\pi} R_c A_0 Q \Delta t \int_{\lambda} \bar{T}_k \Omega_k d\lambda \\ &\approx \frac{10^6}{4\pi} A_0 Q \Delta t \left\{ R_s [B(\lambda) * \bar{T}_k \Omega_k] + R_c \int_{\lambda} \bar{T}_k \Omega_k d\lambda \right\}, \end{aligned} \quad (6)$$

by convolving the instrument function with the band brightness function. Here  $R_s$  is the total band brightness in Rayleighs;  $B(\lambda)$  is normalized band strength;  $A_0$  is the effective area of the instrument in  $\text{cm}^2$ ;  $Q$  is the instrument detection quantum efficiency;  $\Delta t$  is the integration period in second and  $R_c$  is the continuum background brightness in Rayleigh/ $\text{\AA}$ . The instrument detection quantum efficiency  $Q$  is equal to  $Q_k T_{\text{sys}}$ , where  $Q_k$  is the quantum efficiency of the detector at the wavelength corresponding to the k-th channel and  $T_{\text{sys}}$  is the total system transmission. If we consider  $Q_k$  to be independent of channel, the only parameters in equation (6) which vary with channel number are  $T_k$  and  $\Omega_k$ .

### III. Data Inversion and Error Analysis

The total band brightness and the rotational temperature of the emitting molecule can be recovered from the measured multichannel IPD signals. The instrument function shown in figure 3 can be affected by the thermal state of the instrument. All the simulations shown previously have

assumed that the instrument is at a reference temperature. As the temperature changes, the instrument function will be shifted, and the amount of the shift  $\Delta\lambda$  is determined by the filter characteristics. The dark counts of the IPD would also vary with the temperature, and they can usually be corrected before any data analysis is performed. Here, we have assumed that the dark counts are very small and are excluded in the present analysis. Therefore, there are four parameters which could be recovered from the measured spectrum: (1) the total brightness of the band system  $R_s$ , (2) the rotational temperature of the emitter  $T_r$ , (3) the continuum background brightness  $R_c$ , and (4) the center wavelength shift due to the changes of the thermal state of the instrument  $\Delta\lambda$ .

There exist many numerical techniques which can be used for our data analysis. Here we use a non-linear least square fitting technique. In order to conserve computations, we linearize the problem by expanding equation (6) about a set of approximations or initial guesses ( $R_s^{(\alpha)}$ ,  $T_r^{(\alpha)}$ ,  $R_c^{(\alpha)}$ , and  $\Delta\lambda^{(\alpha)}$ ) and keep only the first order terms in the expansion:<sup>10</sup>

$$\begin{aligned}
 N_k = & \frac{10^6}{4\pi} A_0 Q \Delta t \left[ R_s^{(\alpha)} [B(\lambda) * \bar{T}_k \Omega_k]^{(\alpha)} + R_c^{(\alpha)} \int_{\lambda} \bar{T}_k \Omega_k d\lambda + \right. \\
 & [B(\lambda) * \bar{T}_k \Omega_k]^{(\alpha)} [R_s^{(\alpha+1)} - R_s^{(\alpha)}] + R_s^{(\alpha)} \left[ \frac{\partial}{\partial T_r} (B(\lambda) * \bar{T}_k \Omega_k) \right]^{(\alpha)} (T_r^{(\alpha+1)} - T_r^{(\alpha)}) + \\
 & \left. R_s^{(\alpha)} \left[ \frac{\partial}{\partial \Delta\lambda} (B(\lambda) * \bar{T}_k \Omega_k) \right]^{(\alpha)} (\Delta\lambda^{(\alpha+1)} - \Delta\lambda^{(\alpha)}) + \left( \int_{\lambda} \bar{T}_k \Omega_k d\lambda \right) (R_c^{(\alpha+1)} - R_c^{(\alpha)}) \right]. \quad (6a)
 \end{aligned}$$

If measured counts for k-th channel is expressed as  $(10^6 A_0 Q \Delta t / 4\pi) N_{mk}$ , the square of deviation from the theoretical computed signal summing over all the anodes can be calculated by

$$\langle \delta^2 \rangle = (10^6 A_0 Q \Delta t / 4\pi)^2 \sum_k (N_{mk} - N_k')^2, \quad (7)$$

where  $N_k' = N_k / (10^6 A_0 Q \Delta t / 4\pi)$ . By minimizing  $\langle \delta^2 \rangle$ , one can obtain a better estimated value of  $R_s$ ,  $T_r$ ,  $R_c$  and  $\Delta\lambda$  (denoted by superscript  $\alpha+1$ ), or  $X_i^{(\alpha+1)}$  a general representation of the newly estimated parameters from a single matrix multiplication operation:<sup>13</sup>

$$X_i^{(\alpha+1)} = M_{ij}^{-1} P_j, \quad (8)$$

with



$$\begin{aligned}X_1 &= R_s^{(\alpha+1)}, \\X_2 &= T_r^{(\alpha+1)}, \\X_3 &= \Delta\lambda^{(\alpha+1)}, \\X_4 &= R_c^{(\alpha+1)},\end{aligned}$$

$$M_{ij} = \sum_k A_{kj} A_{ki},$$

and

$$P_j = - \sum_k A_{kj} D_k,$$

where

$$\begin{aligned}A_{k1} &= - [B(\lambda) * \bar{T}_k \Omega_k]^{(\alpha)}, \\A_{k2} &= - R_s^{(\alpha)} \left[ \frac{\partial}{\partial T_r} (B(\lambda) * \bar{T}_k \Omega_k) \right]^{(\alpha)}, \\A_{k3} &= - R_s^{(\alpha)} \left[ \frac{\partial}{\partial \Delta\lambda} (B(\lambda) * \bar{T}_k \Omega_k) \right]^{(\alpha)}, \\A_{k4} &= - \int_{\lambda} \bar{T}_k \Omega_k d\lambda,\end{aligned}$$

and

$$D_k = N_{mk} + R_s^{(\alpha)} \left\{ T_r^{(\alpha)} \left[ \frac{\partial}{\partial T_r} (B(\lambda) * \bar{T}_k \Omega_k) \right]^{(\alpha)} + \Delta\lambda^{(\alpha)} \left[ \frac{\partial}{\partial \Delta\lambda} (B(\lambda) * \bar{T}_k \Omega_k) \right]^{(\alpha)} \right\}.$$

The degree of precision obtained depends on the proximity of the input guess values to the actual values. Iterations are performed in order to obtain convergence of the results.

The accuracy of any measurement is governed by the accuracy of the instrument calibration and the counting statistics. Assuming there is no calibration error, the standard deviation of the four deduced parameters,  $\Delta X_i = (\delta X_i^2)^{1/2}$ ,  $i = 1$  to 4, can be simply derived from the theory of error propagation,

$$\begin{aligned}\Delta X_i &= \sqrt{\delta X_i^2} = \frac{1}{\frac{10^6}{4\pi} A_0 Q \Delta t} \left[ \sum_k (C_{ik} N_k) \right]^{1/2} \\ &= \frac{1}{\sqrt{\frac{10^6}{4\pi} A_0 Q \Delta t}} \left[ \sum_k (C_{ik} N_k) \right]^{1/2},\end{aligned}\quad (9)$$

where  $N_k$  is the output count from the  $k$ -th channel of the detector and  $C_{ik}$  is a matrix derived from equation (7). We note that the random errors of the detector can be described by a Poisson distribution and the standard deviation of measured signal is given as  $(N_k)^{1/2}$ .

#### IV. An Example: O<sub>2</sub> (0-1) Atmospheric Band

This instrument is well suited to measuring the molecular emission band structure, such as the O<sub>2</sub> Atmospheric band,<sup>1</sup> and OH Meinel band etc. The O<sub>2</sub> Atmospheric band is one of the strongest band in both terrestrial dayglow and nightglow and has an emission profile peaked at about 95 km.<sup>4,14-16</sup> It originates from the metastable transition between the excited  $b^1\Sigma_g^+$  state and the ground state  $X^3\Sigma_g^-$  of O<sub>2</sub> and has a radiative lifetime of about 12 seconds. The (0-0) band of the O<sub>2</sub> Atmospheric system is completely absorbed by the lower atmosphere and can only be observed from altitude above the stratosphere. The (0-1) band, however, is not attenuated thus is best suitable for ground-based observation.<sup>5,7,8</sup> Figure 5 gives the emission spectra of O<sub>2</sub> (0-1) Atmospheric band at temperatures of 150 K and 300 K for an arbitrary band intensity of 1 kR. The line positions and strengths are calculated based upon the molecular constants of Babcock and Herzberg,<sup>17</sup> the intensity measurements of Miller,<sup>18</sup> and the Frank-Condon factor of Nicholls.<sup>19</sup> The band origin corresponds to a forbidden transition between two rotationless states  $J' = 0$  and  $J'' = 0$  near 8645 Å. The band head is formed in the R branch and lies on the short-wavelength side of the band origin. The lines of the P branch are located on the long-wavelength side of the band origin. Because of rotational level redistribution, the emission spectrum shows different structure as temperature changes. Near the R branch band head and the P branch band tail, the line intensities increase with temperature. This provides us with a tool of monitoring the rotational temperature of the excited O<sub>2</sub>( $b^1\Sigma_g^+$ ) from the changes in band structure with temperature.

Typical zenith O<sub>2</sub> (0-1) Atmospheric band brightness at night is approximately 500

Rayleighs.<sup>5,15</sup> Figure 6 shows the calculated instrument 12 channels output signals at emission temperatures of 150 K and 300 K respectively. The continuum background emission is assumed to be 2.0 R/Å. The instrument parameters used in the simulation are given in Table 1. For an integration time of 10 seconds, the maximum signals of approximately 3000 counts can be obtained, and the variation in signals with the emission temperature is very clear.

Following equation (8), it usually takes approximately 5 iterations to recover the total band brightness, the temperature, the brightness of the background emission and the filter center wavelength shift. Table 2 illustrates the rate of convergence for the spectrum shown in figure 6(b), starting from a set of rather poor guess values.

Figure 7(a) presents the estimated error in the deduced brightness,  $\Delta R_s$ , for emission temperatures of 150 K and 300 K as a function of brightness  $R_s$ . The integration period used here is 10 seconds, and the continuum background is 2.0 R/Å. The error  $\Delta R_s$  in this case increases from 8 R at  $R_s = 10^2$  R to approximately 110 R at  $R_s = 10^5$  R for emission temperature of 300 K. This constitutes an accuracy in the deduced brightness of less than 1% for  $R_s$  greater than  $10^3$  R, and it improves as the emission temperature decreases. As it was indicated in equation (9),  $\Delta R_s$  is proportional to the square root of the output counts. Therefore  $\Delta R_s/(R_s)^{1/2}$  approaches a constant as  $R_s$  increases to a level when continuum background emission is negligible ( Figure 7b). Figure 8 gives the error in the deduced emission temperature. Note that the output counts  $N_k$  is proportional to  $10^6 A Q \Delta t / 4\pi$ , implying that the error in the deduced physical quantities,  $\Delta X_i$  is inversely proportional to the square root of the instrument parameters,  $A_0$ ,  $Q$ , and the integration period  $\Delta t$ . By observing O<sub>2</sub> (0-1) Atmospheric band system at night ( ~ 500 Rayleighs), the instrument described here is able to measure the band brightness with an accuracy of  $\pm 10$  Rayleighs and the temperature with an accuracy of  $\pm 6$  K, for an integration period of 10 seconds, and  $\pm 4$  Rayleighs and  $\pm 2.6$  K for a integration period of 1 minute.

## V. Summary

In this paper, we introduced a low resolution spectrophotometer with an interference filter as wavelength dispersive element and a multichannel Image Plane Detector as light collecting device. This instrument, characterized by its relatively high throughput and modest resolution, is suited to monitoring the brightness and rotational temperature of molecular band emission. A simulated instrument was presented here as an example to demonstrate its capability in measuring the O<sub>2</sub> (0-1) Atmospheric band emission in the nightglow. For an integration period of 10 seconds, this

instrument is able to measure temperature with an accuracy of  $\pm 6$  K and brightness with an accuracy of  $\pm 10$  Rayleighs for a typical zenith emission brightness of 500 Rayleighs.

### **Acknowledgements**

This research was supported at the University of Michigan by Air Force Geophysical Laboratory grant DOD-F19628-87-K-0039 and partly by NASA grant NAG5-465.

## References

1. G. Herzberg, *Molecular spectra and molecular structure*. (D. Van Nostrand Company, New York, 1947).
2. G. Hernandez, "Analytical Description of a Fabry-Perot photoelectric Spectrometer," *Appl. Opt.* **5**, 1745 (1966).
3. P. B. Hays, A. F. Nagy and R. G. Roble, "Interferometric measurements of the 6300 Å Doppler temperature during a magnetic storm," *J. of Geophys. Res.* **74**, 4162 (1969).
4. L. Wallace and D. M. Hunten, "Dayglow of the oxygen A band," *J. of Geophys. Res., Space Physics* **73**, 4813 (1968).
5. J. F. Noxon, "Effect of internal gravity waves upon night airglow temperatures," *Geophys. Res. Letters* **5**, 25 (1978).
6. R. H. Eather, and D. L. Reasoner, "Spectrophotometry of faint light sources and a tilting-filter photometer," *J. Applied Optics.* **8**, 227 (1969).
7. K. Misawa and I. Takeuchi, "Correlations among O<sub>2</sub>(0-1) atmospheric band, OH(8-3) band and [OI] 5577 Å line and among P1(2), P1(3) and P1(4) lines of OH(8-3) band," *J. of Atmospheric and Terrestrial Physics* **40**, 421 (1978).
8. H. Takahashi, P. P. Batista, Y. Sahai and B. R. Clemisha, "Atmospheric wave propagations in the mesopause region observed by the OH(8,3) band, NaD, O<sub>2</sub>A (8645) band and OI 5577 Å nightglow emissions," *Planet. Space Sci.* **33**, 381 (1985).
9. G. R. Swenson, *A study of a sector spectrometer and auroral O<sup>+</sup> (<sup>2</sup>P - <sup>2</sup>D) emissions*. (Ph.D. Thesis, University of Michigan, 1975)
10. P. B. Hays, T. L. Killeen, and B. C. Kennedy, "The Fabry-Perot interferometer on Dynamics Explorer," *Space Sci. Instrumentation* **5**, 395 (1981).
11. T. L. Killeen, B. C. Kennedy, P. B. Hays, D. A. Symanow and D. H. Ceckowdki, "An Image Plane Detector for the Fabry-Perot photoelectric spectrometer," *Appl. Opt.* **22**, 3503 (1983).
12. P. H. Lissberger, "Properties of all-dielectric interference filters. I. a new method of calculation," *J. of the Optical Society of America* **49**, 121 (1959).
13. T. L. Killeen and P. B. Hays, "Doppler line profile analysis for a multichannel Fabry-Perot interferometer," *Appl. Opt.* **23**, 612 (1984).
14. M. R. Torr, D. G. Torr and R. R. Laher, "The O<sub>2</sub> Atmospheric 0-0 band and related emissions at night from spacelab 1," *J. of Geophys. Res.* **90**, 8525 (1985).
15. I. C. McDade, D. P. Murtagh, R. G. H. Greer, P. H. G. Dickinson, G. Witt, J. Stegman, E. J. Llewellyn, L. Thomas and D. B. Jenkins, "ETON 2: Quenching parameters for the proposed precursors of O<sub>2</sub>(b<sup>1</sup>Σ<sub>g</sub><sup>+</sup>) and O(<sup>1</sup>S) in the terrestrial nightglow," *Planet. Space*

- Sci. **34**, 789 (1986).
16. A. Bucholtz, W. R. Skinner, V. J. Abreu, and P. B. Hays, "The dayglow of the O<sub>2</sub> Atmospheric band system," Planet. Space Sci. **34**, 1031 (1986).
  17. H. D. Babcock, and L. Herzberg, "Fine structure of the red system of atmospheric oxygen band," Astrophys. J. **108**, 167 (1948).
  18. J. H. Miller, "Intensity measurements and rotational intensity distribution for the oxygen A-Band," J. Quant. Spectrosc. Radiat. Transfer **9**, 1507 (1969).
  19. R. W. Nicholls, "Frank-Condon factors to high vibrational Quantum numbers V: O<sub>2</sub> band systems," J. Res. NBS **69A**, 369 (1965).

**Table 1. Parameters of Simulated Instrument**

---

Interference Filter		
center wavelength, $\lambda_0$		8730 Å
full width at half height (FWHH)		~12 Å
maximum transmittance		0.5
Objective Lens		
focal length		2.27 cm
IPD		
anode structure		12 concentric ring, equal area anodes
area of anode		0.076 cm <sup>2</sup>
radius of anode ring		(see Killeen <i>et al.</i> 1983)
quantum efficiency at $8730 \pm 50 \text{ Å}$ , $\theta_k$		0.005
Aperture		
effective area, $A_0$		1 cm <sup>2</sup>
Total System Transmission, $T_{\text{sys}}$		0.4

---

Table 2. An Example of Data Analysis Output

Integration	Brightness (kR)	Temperature (K)	Shift of Filter Center Wavelength (Å)	Continuum Background (R/Å)
guess	5.0	400.	-1.0	0.0
1	10.0	163.	1.37	45.0
2	9.0	242.	1.09	13.5
3	9.9	295.	0.13	5.6
4	10.0	300.	0.03	5.0
5	10.0	300.	0.03	5.0
True	(10.0)	(300.)	(0.00)	(5.0)



## FIGURE CAPTIONS

- Fig 1: Schematics of the Image Plane Detector Spectrophotometer.
- Fig 2: The transmission function of a simulated double cavity interference filter with peak transmission normalized to 1.0.
- Fig 3: The filter transmission functions for 12 light incident angles:  $\theta_k = (k-1)^{1/2}\theta_c$ ,  $k = 1, 2, \dots, 12$  and  $\theta_c = 4.4^\circ$ .
- Fig 4: Instrument transmission function  $\bar{T}_k$ , multiplying the field of view  $\Omega_k$  ( $k = 1, 2, \dots, 12$ ).
- Fig 5:  $O_2$  (0-1) Atmospheric band emission spectra with total band brightness of 1kR at a temperature of (a) 150 K and (b) 300 K.
- Fig 6: The calculated 12 channel IPD Spectrophotometer signals for a (0-1) band source brightness of 500 Rayleighs at an emission temperature of (a) 150 K and (b) 300 K (integration time = 10 seconds).
- Fig 7: (a) Absolute error  $\Delta R_s$ , and (b) normalized error  $\Delta R_s / (R_s)^{1/2}$  in the deduced brightness for an integration period of 10 seconds.
- Fig 8: Absolute error in the deduced temperature for an integration period of 10 seconds.

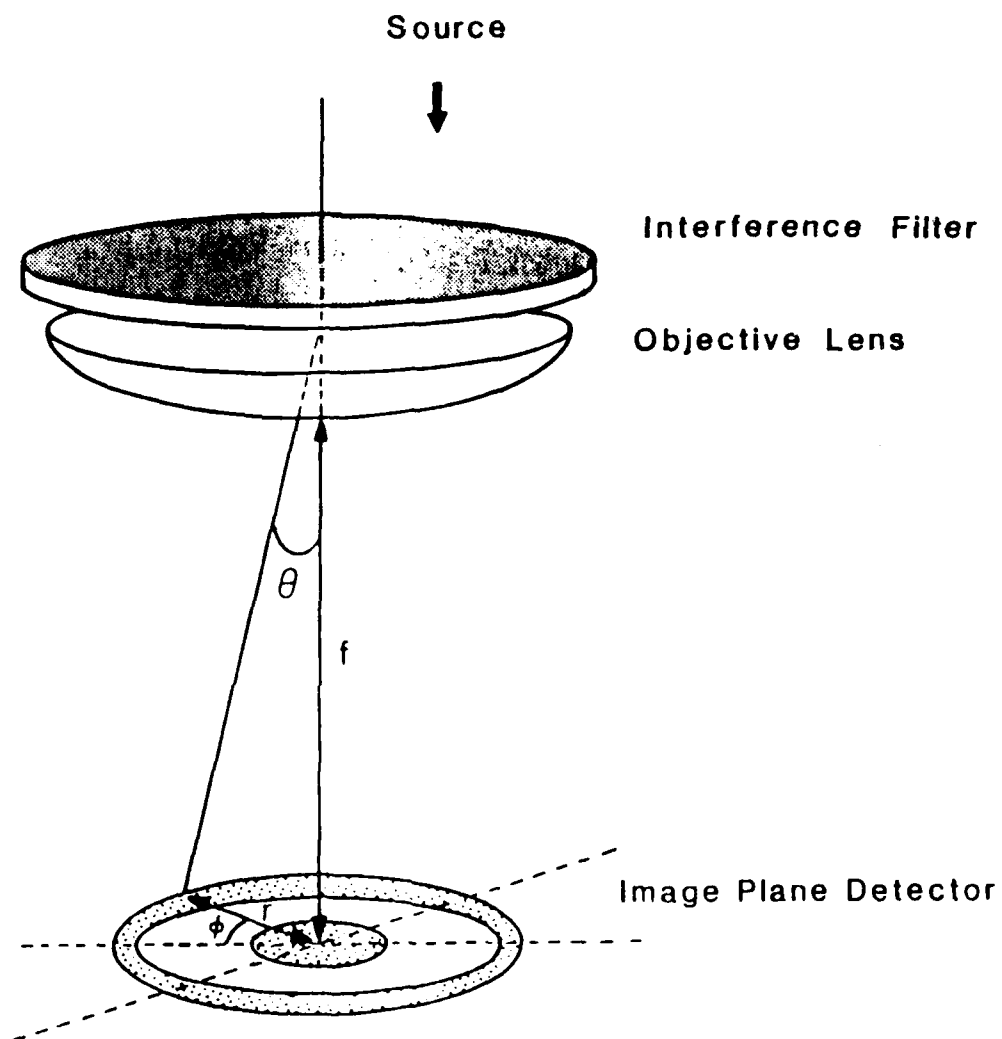


Fig. 1.

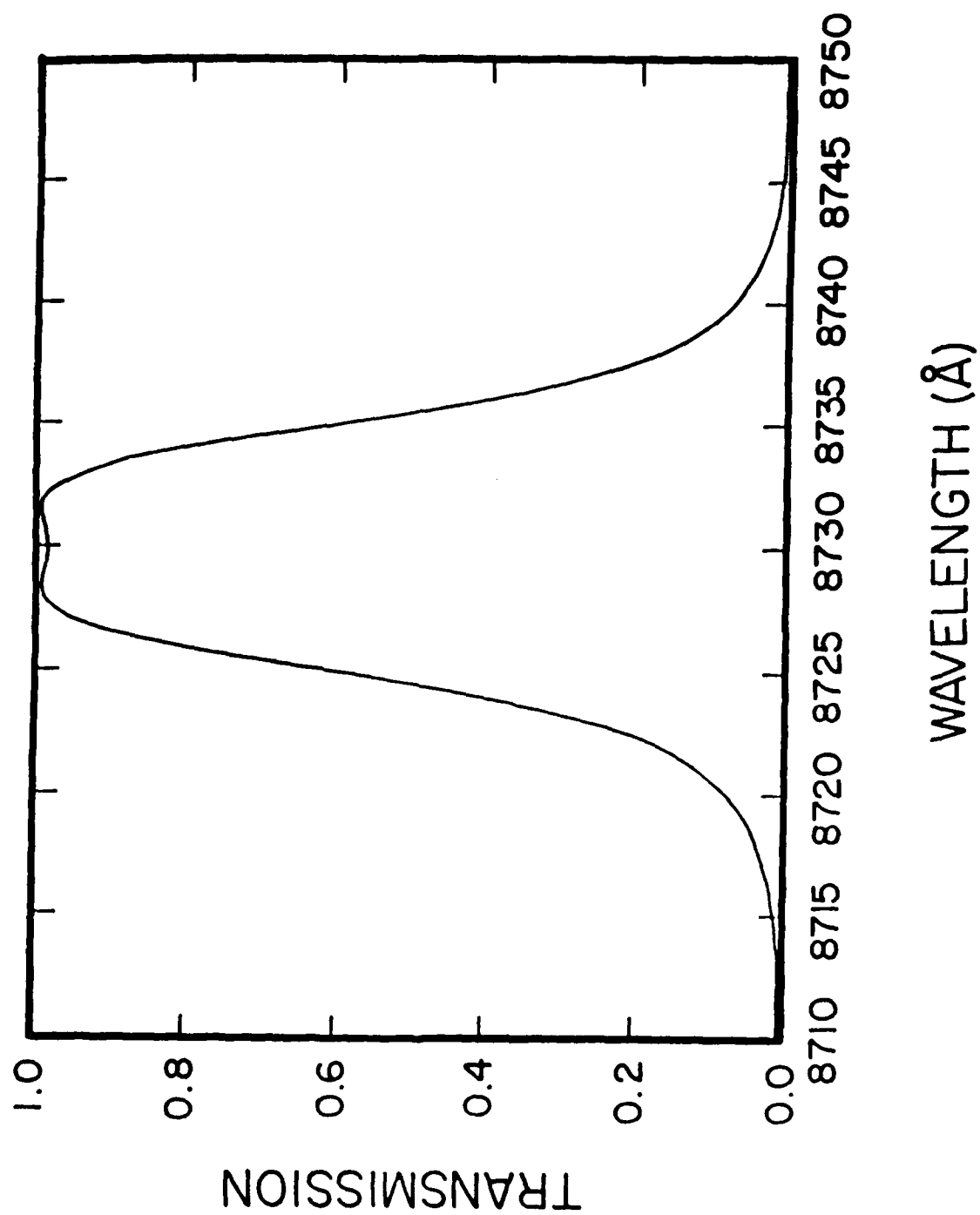


Fig. 2.

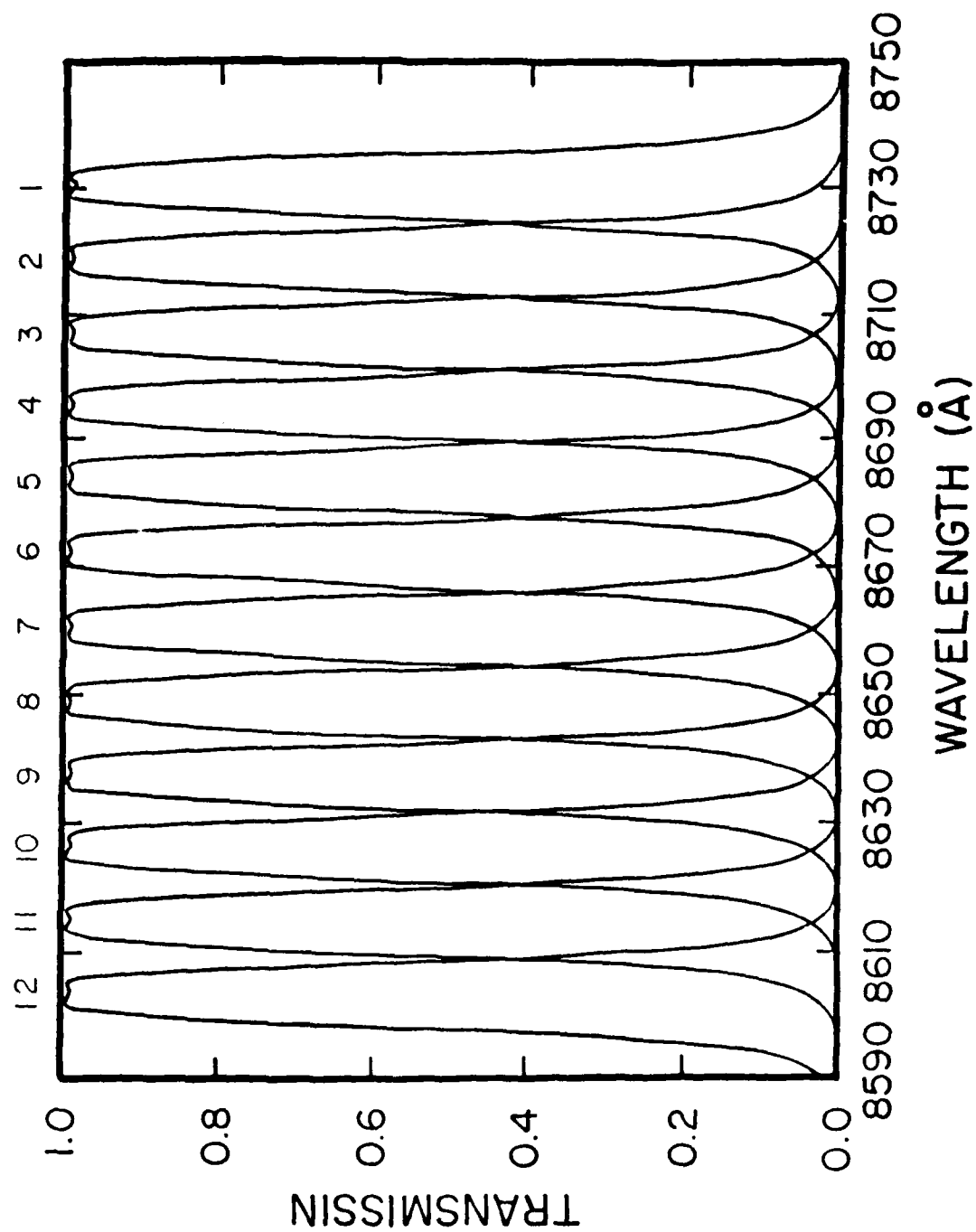


Fig. 3.

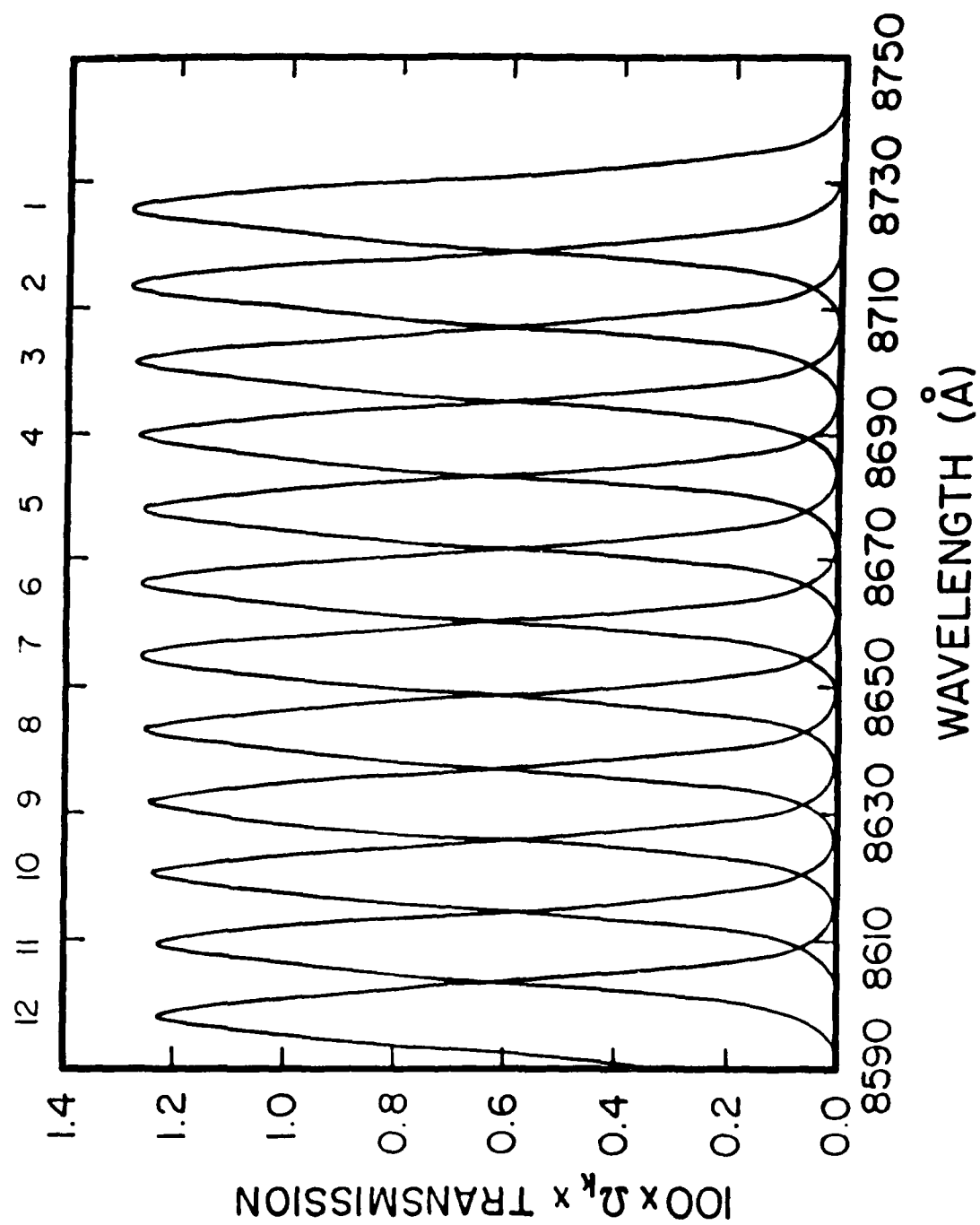


Fig. 4.

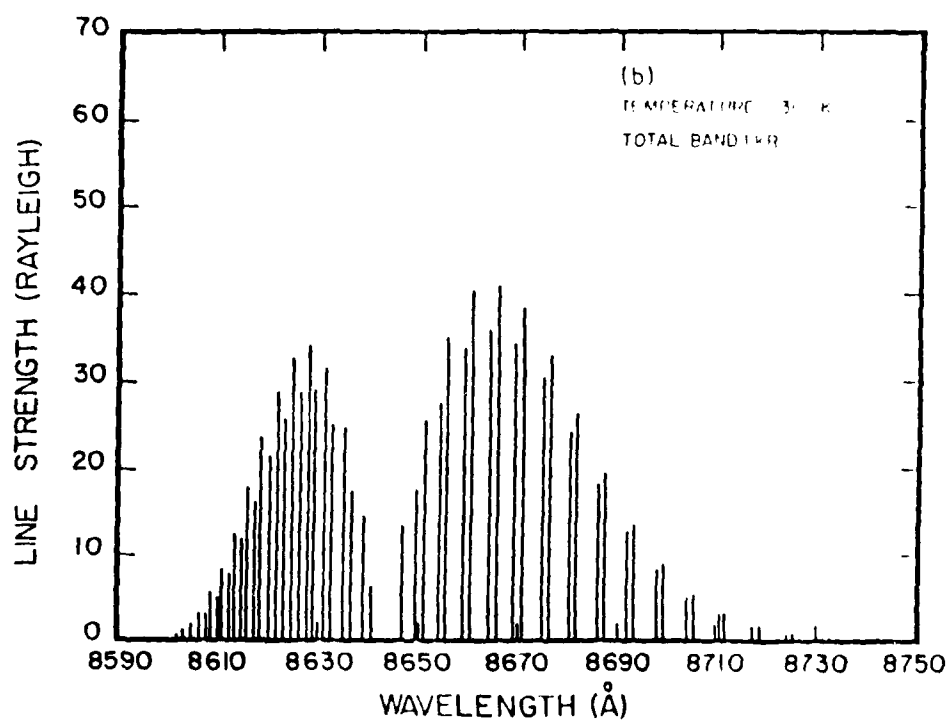
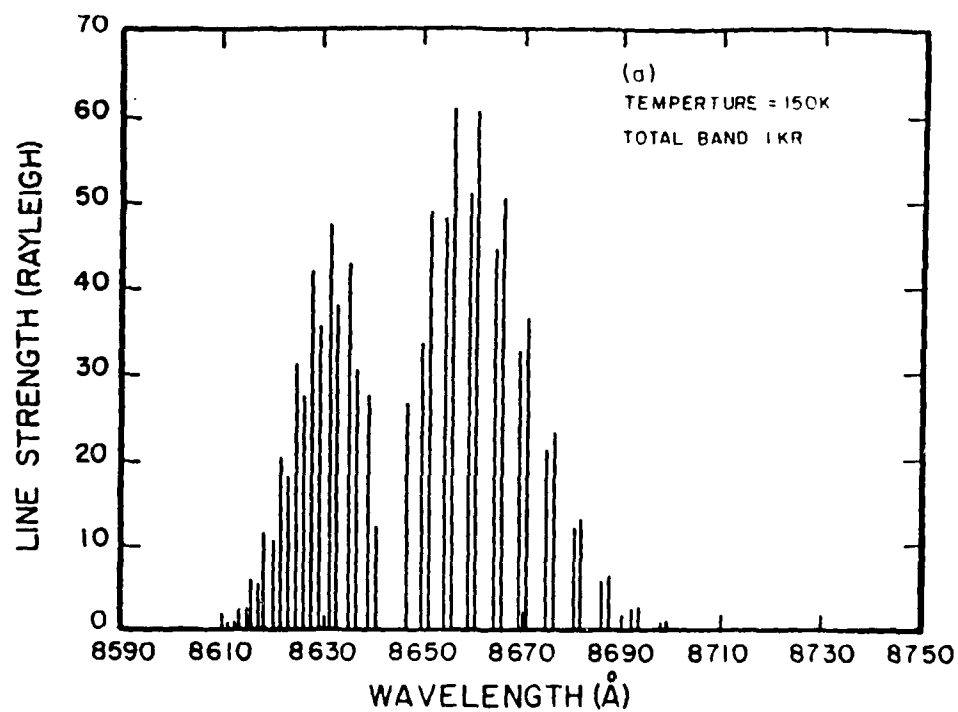


Fig. 5.

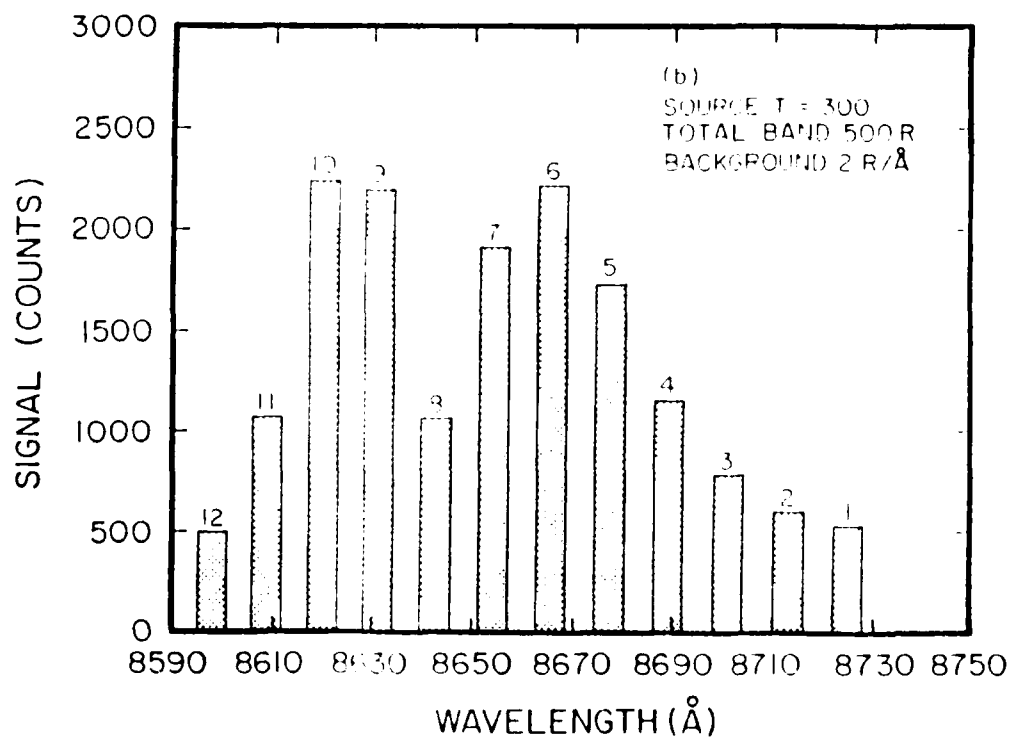
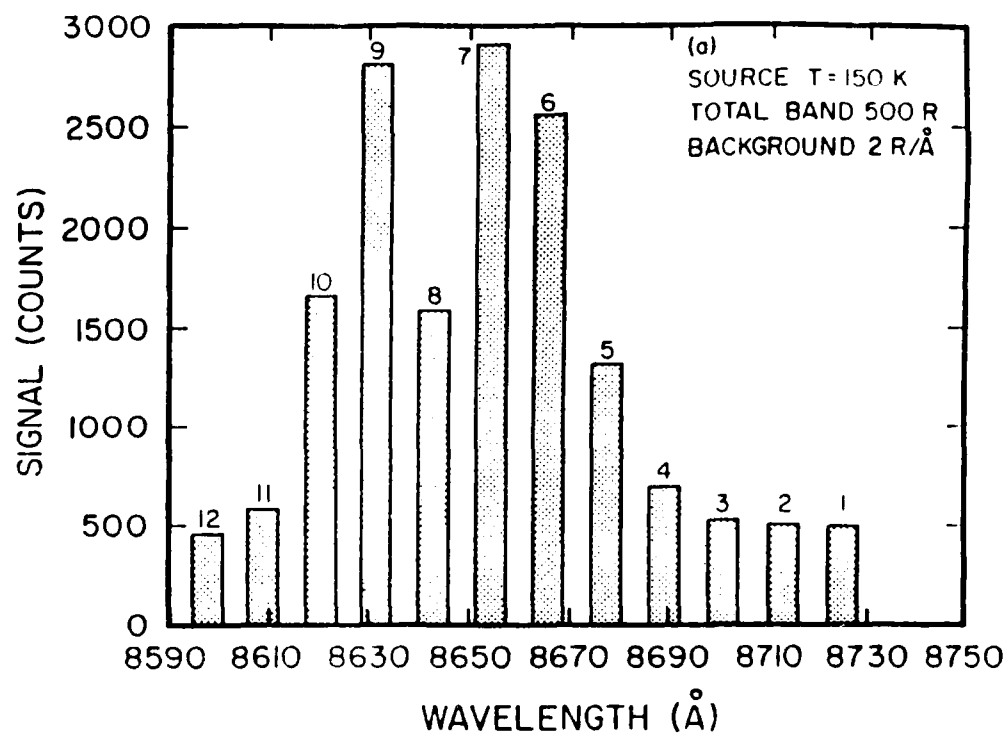


Fig. 6.

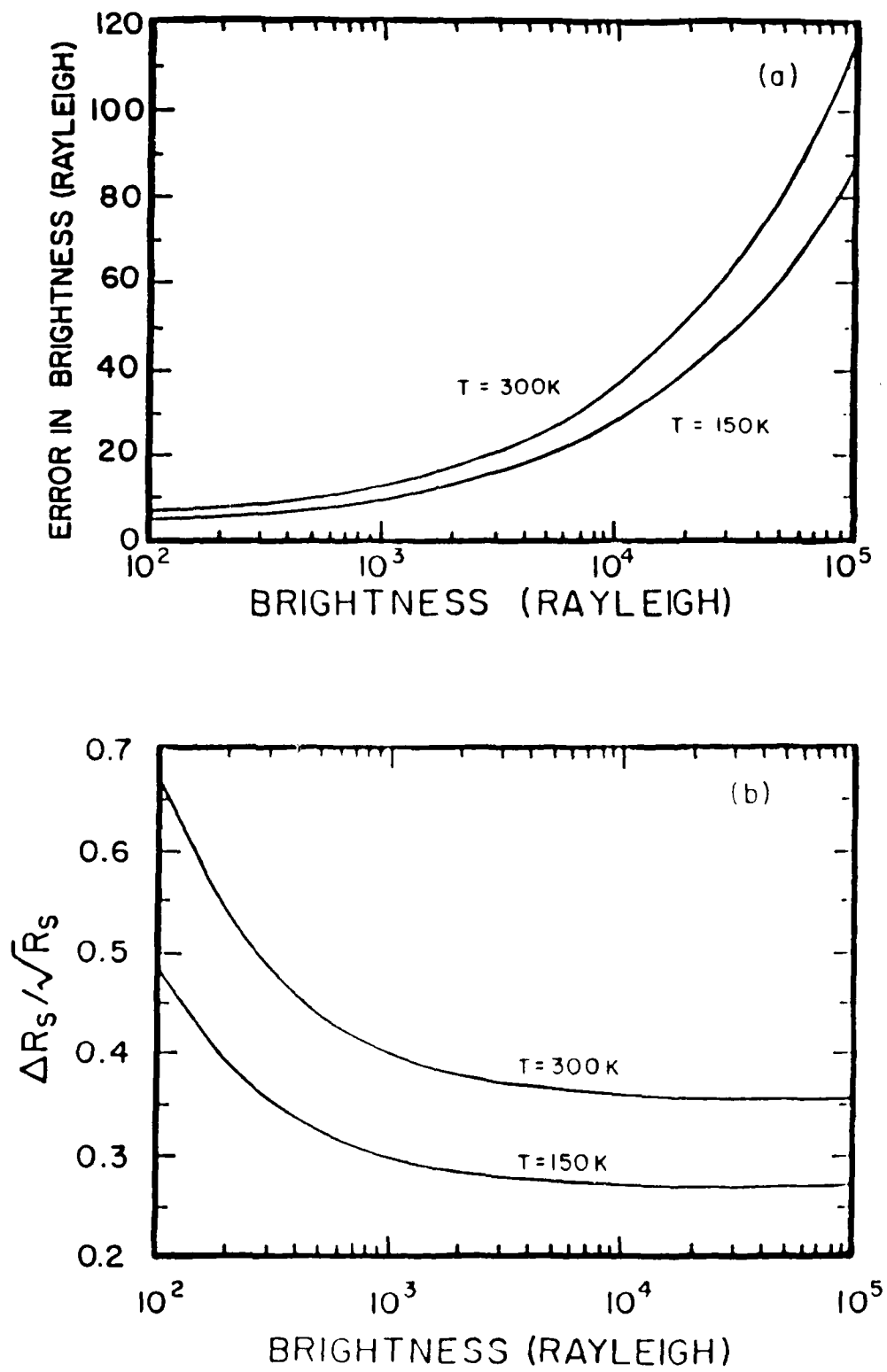


Fig. 7.



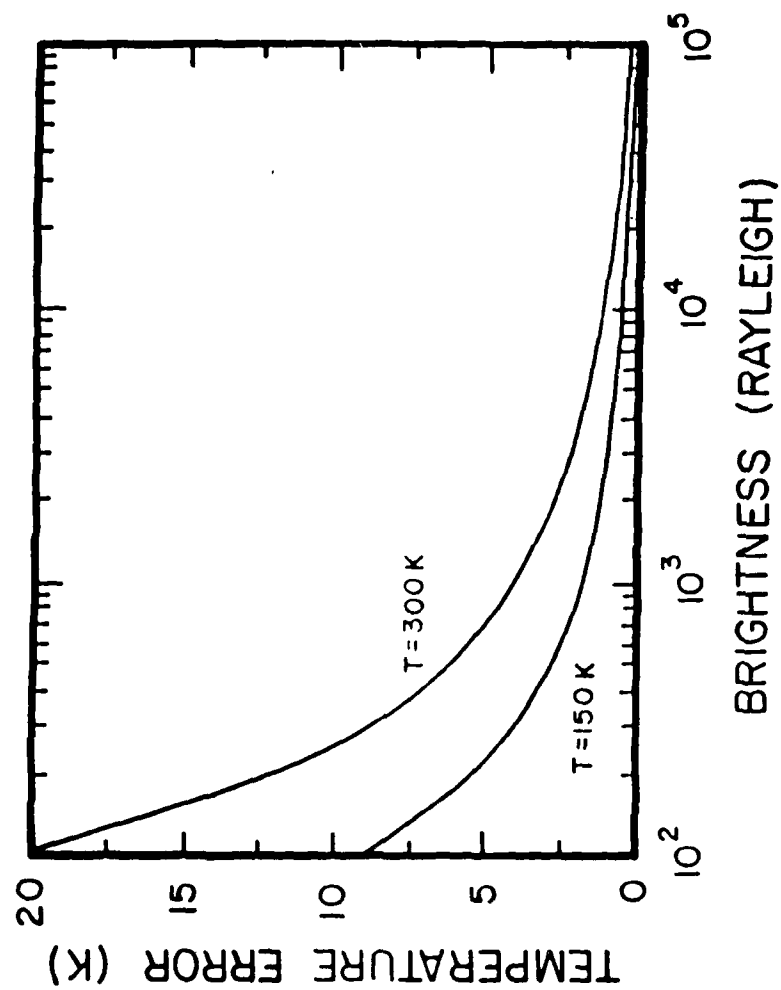


Fig. 8.

DATE  
FILMED  
— 8

